Green Diesel Production via Hydrodeoxygenation of Triglycerides

Thèse

Arsia Afshar Taromi

Doctorat en génie chimique

Philosophiae doctor (Ph. D.)

Québec, Canada

Résumé

En raison des problèmes environnementaux associés à l'utilisation des combustibles fossiles, qui augmentent les émissions de gaz à effet de serre et causent les changements climatiques, et pour satisfaire le besoin mondial de carburants durables et surmonter une éventuelle crise énergétique, une part important de l'attention de la communauté scientifique est aujourd'hui consacrée à la découverte de sources d'énergie renouvelables. L'une des meilleures alternatives est le diesel vert qui pourrait être produit à partir d'huiles végétales (aucune quantité nette de dioxyde de carbone n'est rejetée dans l'atmosphère). Ces types d'huiles sont convertis en diesel vert par réaction d'hydrotraitement à haute température et pression en présence d'un catalyseur hétérogène qui joue un rôle essentiel dans ce processus.

Ces catalyseurs hétérogènes, qui peuvent être bi- ou monométalliques, sont constitués d'un support et d'un composé métallique actif. Les caractéristiques du support telles que la surface spécifique, le volume des pores et le diamètre des pores ont un effet déterminant sur les propriétés finales du catalyseur formé. Ils peuvent déterminer la quantité de la charge de phase active optimale et peuvent être adaptés à la taille moléculaire du réactif. Dans cette thèse, un support d'alumine-γ mésoporeuse a d'abord été synthétisé en utilisant un polymère tensioactif par voie sol-gel et accompagné d'un auto-assemblage induit par évaporation (EISA). L'isopropoxyde d'aluminium ($Al(O\text{-}i\text{-}Pr)_3$) et le copolymère tribloc (Pluronic P123) ont été respectivement utilisés comme source d'aluminium et agent directeur de structure. La température de calcination optimale et le rapport massique P123/$Al(O\text{-}i\text{-}Pr)_3$ respectivement de 700ºC (avec 3 h de temps de trempage) et 0.98 permettent la production de γ-alumine avec des propriétés texturales appropriées. À l'étape suivante, 15% en poids de MoO_3 et 3% en poids de NiO ou CoO ont été imprégnés sur le support préparé pour former NiMo/γ-alumine et CoMo/γ-alumine respectivement après calcination. Suite à une sulfuration ex-situ, l'hydrotraitement de l'huile de canola a été effectué dans un réacteur continu pour la production de diesel vert. Une plage de température de 325 à 400°C et une de LHSV de 1 à 3 h^{-1} ont été étudiées tandis que les autres paramètres opérationnels ont été maintenus constants à P: 450 psi et H_2/huile: 600 $mLmL^{-1}$. Les deux catalyseurs ont permis la production de diesel vert (principalement C15-C18) tandis que NiMo a montré une activité légèrement

supérieure à un LHSV plus élevé. La température optimale et le LHSV se sont révélés être 325ºC et 1 h^{-1}.

Finalement, des catalyseurs Ni/γ-alumine (réduite) respectueux de l'environnement avec structure mésoporeuse ont été synthétisés par des procédés sol-gel (une étape) et d'imprégnation (deux étapes). Une teneur en oxyde de nickel plus faible a été observée dans un catalyseur dérivé du sol-gel par rapport aux produits imprégnés, ce qui est dû à l'incorporation de nickel dans le réseau de l'alumine. Après la réduction, du nickel métallique a été formé dans les deux catalyseurs. L'hydrotraitement de l'huile de canola a été effectué sur les deux catalyseurs (température: 400°C, P: 500 psi, LHSV: 0.5 h^{-1}, H_2/huile: 600 $mLmL^{-1}$) et des hydrocarbures normaux, principalement C15-C18. Il a été observé que la conversion des triglycérides était initialement plus élevée pour le catalyseur imprégné et, après un temps en ligne de 300 min, elle tombe à des valeurs inférieures à celles du catalyseur sol-gel, ce qui montre la plus grande stabilité au fil du temps de ce dernier.

Abstract

Owing to environmental issues concerning fossil fuels usage which increase the greenhouse gas emissions and cause climate change, and to satisfy the global need for sustainable fuels and overcome possible energy crisis much attention is devoted to the finding of sustainable energy sources. One of the best alternatives is green diesel which could be produced from vegetable oils (no net amount of carbon dioxide is released into the atmosphere). These kinds of oils are converted to green diesel via hydrotreating reaction at high temperature and pressure in the presence of a heterogeneous catalyst which plays an essential role in this process. These heterogeneous catalysts which could be bi- or monometallic, consist of a support and an active metal compound. The characteristics of the support such as specific surface area, pore volume and pore diameter have a determining effect on the final properties of the formed catalyst. They can determine the amount of optimum active phase loading and should be adapted to the reactant molecular size.

In this thesis first, the γ-alumina support was one-pot synthesized via polymeric template assisted sol-gel and evaporation-induced self-assembly process. Aluminum isopropoxide ($Al(O\text{-}i\text{-}Pr)_3$) and triblock copolymer template (Pluronic P123) were respectively used as aluminum source and structure directing agent. The optimum calcination temperature and P123/$Al(O\text{-}i\text{-}Pr)_3$ mass ratio were respectively found to be 700ºC (with 3 h of soaking time) and 0.98 enabling the production of γ-alumina with appropriate textural properties. In the next step, 15% wt. MoO_3 and 3% wt. NiO or CoO were impregnated on the prepared support to respectively form NiMo/γ-alumina and CoMo/γ-alumina after subsequent calcination. Following an ex-situ sulfidation, the hydrotreatment of canola oil was performed in a continuous reactor to result in green diesel production. Temperature range of 325 to 400ºC and LHSV of 1 to 3 h^{-1} were studied while the other process parameters were kept constant at P: 450 psi and H_2/oil: 600 $mLmL^{-1}$. Both catalysts are promising for green diesel (mainly C15-C18) production while NiMo showed a slightly higher activity at higher LHSV. The optimum temperature and LHSV were found to be 325ºC and 1 h^{-1}.

Finally, the environmentally friendly Ni/γ-alumina (reduced) catalysts with mesoporous structure were synthesize through sol-gel (one-step) and impregnation (two-step) methods.

Lower bulk nickel oxide content was detected in sol-gel derived catalyst compared to impregnated ones which is due to the incorporation of nickel inside the alumina framework. After the reduction, metallic nickel was formed in both catalysts. Canola oil hydrotreatment was performed over both catalysts (temperature: 400ºC, P: 500 psi, LHSV: 0.5 h^{-1}, H_2/oil: 600 $mLmL^{-1}$) and normal hydrocarbons, mainly C15-C18, were produced. The triglyceride initial conversion was observed to be higher over the impregnated catalyst while after a time on stream of 300 min, it falls to values lower than that of the sol-gel catalyst, showing the higher stability over time of the latter.

Table of Contents

List of Tables

List of Figures

Abbreviations

Al	Aluminium
Al_2O_3	Aluminum oxide
$Al(O\text{-}i\text{-}Pr)_3$	Aluminum isopropoxide
AlOOH	Boehmite
BET	Brunauer-Emmett-Teller
BJH	Barrett-Joyner-Halenda
CO	Carbon monoxide
CO_2	Carbon dioxide
Co	Cobalt
$Co(NO_3)_2.6H_2O$	Cobalt(II) nitrate hexahydrate
CS_2	Carbon disulfide
Cu	Copper
DCO	Decarbonylation
DCO_2	Decarboxylation
DG	Diglyceride
DMDS	Dimethyl disulfide
DSC/DTA	Differential scanning calorimetry/Differential thermal analysis
EISA	Evaporation-induced self-assembly
EPMA	Electron probe microanalyzer

Et-OH	Ethanol
FAME	Fatty acid methyl ester
FID	Flame ionization detector
FTIR	Fourier transform infrared spectroscop
FWHM	Full width half maximum
GC-MS	Gas chromatography mass spectrometry
GHG	Greenhouse gas emission
HDO	Hydrodeoxygenation
HNO_3	Nitric acid
HPLC	High performance liquid chromatography
IMP	Impregnated
IR	Infrared
LHSV	Liquid hourly space velocity
MG	Monoglyceride
MO	Morphological operation
Mo	Molybdenum
N_2	Nitrogen
NaOH	Sodium hydroxide
Ni	Nickel
$(NH_4)_6Mo_7O_{24}.4H_2O$	Ammonium heptamolybdate tetrahydrate
$NiAl_2O_4$	Nickel aluminate

NLDFT	Nonlinear density functional theory
$Ni(NO_3)_2.6H_2O$	Nickel(II) nitrate hexahydrate
PFD	Process flow diagram
PMMA	Poly methyl methacrylate
PSD	Pore size distribution
Pt	Platinum
Pd	Palladium
-R	Reduced form
S	Sulfur
SAXS	Small-angle X-ray scattering
SE	Structural element
SEM	Scanning electron microscope
SD	Standard deviation
SG	Sol-gel
STP	Standard temperature and pressure
-S	Sulfided form
TEM	Transmission electron microscopy
TG	Triglyceride
TGA/DTG	Thermogravimetric analysis/The first derivative of the TGA
TOS	Time on stream
UV	Ultra violet

W	Tungsten
WAXS	Wide angle X-ray scattering
WDS	Wavelength dispersive X-ray spectrometer
-WT	Without template
WCO	Waste cooking oil
XPS	X-ray photoelectron spectroscopy
XRD	X-ray diffraction

Symbols

B and b	Represent FWHM and instrumental broadening established using the FWHM of quartz X-ray reflection, including particles larger than 150 nm at $2\theta \approx 27^{o}$
d	Interplanar spacing
D	Average crystalline size
f(d)	Frequencies of pore numbers of different sizes
h, k, l	Miller integer indices
I(x,y)	Intensity having coordinates of x and y
K	Scherrer constant ≈ 0.9
T	Temperature
V	Volume
V(d)	Pore volume frequency

W	Width
α	Lattice parameter
β	Effective linewidth of the X-ray reflection
θ	Bragg's diffraction angle position
λ	1.54059 Å
∇^2	Second order derivative
$\frac{\partial^2}{\partial y^2}, \frac{\partial^2}{\partial x^2}$	Second partial derivatives in y and x coordinates

Dedication

To my immortal beloved ones: my parents

Acknowledgments

First, I wish to offer my deepest appreciation to my supervisor Professor Serge Kaliaguine, for his availability, advice and insight in different aspects of this project. I thank him for giving me the opportunity to continue this doctorate.

I also would like to thank the thesis committee, Professor Céline Vaneeckhaute, Professor Anthony Dufour and Professor Rajeshwar Dayal Tyagi for evaluating this dissertation.

Besides, I want to thank Gilles Lemay for his help on different equipment and also Dr. Alain Adnot, Dr. Marc Choquette, Jean Frenette, Pierre Audet, Jérome Noël, Marc Lavoie and Jean-Nicolas Ouellet for their assistance.

I am also very grateful to my friends and office mates particularly Dr. Hajar Yousefian, Dr. Delaram Fallahi, Zahra Tabatabaei-Yazdi, Dr. Bardia Yousefi, Dr. Reza Darvishi, Kazem Shahidi, Raoof Bardestani, Frédéric Morneau Guérin and Siavosh Moghaddamzadeh for their invaluable supports and advices.

I recognize that this research would not have been possible without the financial assistance and technical support from the Natural Sciences and Engineering Research Council of Canada (NSERC).

Last, but not least, I want to thank my parents for their love, patience and encouragement.

Forewords

The first chapter of this thesis, which includes five chapters, is an introduction to the production of green diesel from triglycerides using heterogeneous catalysts. A brief literature review on key aspects of the green diesel production such as the feedstock, methods to produce fuel from oils, hydrotreatment mechanism and process and different used catalysts is presented.

Chapters 2-4 present experimental results in the form of published or submitted journal papers. My contributions in these articles are performing the experimental works, collecting and analyzing the data and writing the first draft of the manuscripts.

In chapter two, mesostructured γ-aluminas were synthesized via one-pot sol-gel method with the aims to be used as a catalyst support for the hydrotreatment of triglycerides. The effect of calcination temperature and polymeric template concentration on the final properties of the mesoporous γ-alumina were investigated. The paper is published as:

***Afshar Taromi, A**., and Kaliaguine, S. Synthesis of ordered mesoporous γ-alumina- Effect of calcination conditions and polymeric template concentration, Microporous and Mesoporous Materials, Volume 248, August 2017, Pages 179-191.*

Chapter three consists of the preparation of nanoporous bimetallic NiMo/γ-alumina and CoMo/γ-alumina catalysts using mesoporous γ-alumina as the catalyst support, via incipient wetness co-impregnation. The hydrotreatment of vegetable oil was performed in a continuous fixed-bed reactor varying the LHSV and temperature as process parameters. The final green diesel product consisted mainly of n-alkanes, mostly C15-C18. Slightly better catalytic activity was found over Ni-based catalyst compared to the Co-based catalyst. The optimum temperature and LHSV were found to be 325ºC and 1 h^{-1}, respectively. The paper is published as:

***Afshar Taromi, A.**, and Kaliaguine, S. Green diesel production via continuous hydrotreatment of triglycerides over mesostructured γ-alumina supported NiMo/CoMo catalysts, Fuel Processing Technology Journal, Volume 171, March 2018, Pages 20-30.*

In the fourth chapter, the environmentally friendly reduced Ni/γ-alumina catalysts were used for the hydrotreatment of vegetable oil in a fixed-bed down-flow homemade reactor. Two methods were used for the catalyst preparation: sol-gel (one-step) and impregnation (two-step). The previously developed mesostructured γ-alumina was used as catalyst support for the impregnated catalyst while for the sol-gel derived catalysts the nickel was incorporated in the mesostructured framework. The collected products mainly consist of C15 to C18 normal hydrocarbons. The sol-gel catalysts showed higher time on stream due to the higher stability compared to the impregnated catalyst. The paper is currently under revision as:

***Afshar Taromi, A.**, and Kaliaguine, S. Hydrodeoxygenation over reduced mesostructured Ni/γ-alumina catalysts prepared via one-pot sol-gel route for green diesel production, Applied Catalysis A Journal, Under revision, 2017.*

Finally, the fifth chapter provides overall conclusions regarding the works above along with some recommendations for future work. More results obtained from this work were also presented in the following conference presentations:

***Afshar Taromi, A.**, and Kaliaguine, S. Monometallic reduced Ni/γ-alumina catalysts for green diesel production: Effect of synthesis methods, 4th CRIBIQ Student Symposium, Québec City, Québec, Canada, 25th-26th, September 2017.*

***Afshar Taromi, A.**, and Kaliaguine, S. Preparation of templated mesoporous γ-alumina catalysts supports, synthesis, structural properties and catalytic activity for triglycerides hydrogenation, 66th Canadian Chemical Engineering Conference, Québec City, Québec, Canada, 16th -19th, October 2016.*

***Afshar Taromi, A.**, and Kaliaguine, S. Hydroprocessing of vegetable oils to produce green diesel over sulfide NiMo/γ-alumina and CoMo/γ-alumina catalysts, International Meeting on Advanced Materials and Processes for Environment, Energy, and Health, Québec City, Québec, Canada, 14th -16th, October 2015.*

***Afshar Taromi, A.**, and Kaliaguine, S. Biofuel production from various oils via Hydrotreatment, 64th Canadian Chemical Engineering Conference, Niagara Falls, Ontario, Canada, 19th-22nd, October 2014.*

***Afshar Taromi, A.**, and Kaliaguine, S. Catalyst evaluation for Biofuel Production from Various Oils via Hydrotreatment, 3rd CRIBIQ Student Symposium, Montréal, Québec, Canada, 22nd-23rd, September 2014.*

Chapter 1

Introduction

1.1 General Context

Transportation is one of the main sectors that significantly contributes to the global economy and liquid fuels continue to be the principal source of transportation energy consumption. Currently, the main energy supply for this sector relies on petroleum-derived fuels. From 2012 to 2040, an average increase of 1.4% per year is estimated for the total energy use in the transportation sector. In 2012, 25% of the total worldwide energy consumption was in the transportation sector. Transportation sector is responsible for almost 21% of greenhouse gas (GHG) emission worldwide and will remain around the same amount until 2020. International Energy Agency (IEA) has predicted that around 8.6 metric billion tons of carbon dioxide (CO_2) will be released to the atmosphere from 2020 to 2035 [1], [2]. As a result of the depletion of fossil fuel reserves and the adverse impact on the environment such as global warming, the development of alternative clean sustainable fuels from renewable resources is considered to be crucial. Among different renewable sources of energy such as hydropower, solar power, wind power, ocean and geothermal energy, etc. biomass is the only one capable of producing stored energy in the form of materials. In addition to the use of these biomass derived materials as fuel which could be in the forms of solid, liquid or gas, it is also possible to use them to produce downstream value-added bio-based chemicals. Different value-added bio-based chemicals such as biopolymers, bioproducts and additives could reduce the process cost and thus enhance the economic feasibility.

One of the most promising and sustainable liquids (oils) derived from biomass are triglycerides and fatty acids. Due to their simple chemical structure (the only functional group is the carboxylic group), they have attracted the attention of bioenergy industries [3]. Triglycerides can be obtained from various sources namely; vegetable oils, animal fats, algae

oils and waste cooking oil (WCO). Direct use of oils and fats causes several problems on the engine parts (pistons, rings, cylinder head, etc.), and thus they must inevitably be upgraded. The hydrotreatment product of triglycerides at high hydrogen pressure and temperature in the presence of catalysts is a green fuel (aliphatic alkanes). It is possible to gain different carbon chain lengths by tuning the catalysts' characteristics and varying the hydrotreatment process parameters.

Green diesel (also known as 2nd generation biodiesel) is a kind of bio-based carbon neutral renewable fuel, having properties similar to petroleum-derived diesel. Green diesel is carbon neutral and therefore does not participate in GHG discharge in the atmosphere. It could be used in transportation sector without any or with minimal modification in the current diesel fuel engines. The engine power is not affected upon the use of green diesel and it could be blended in any portion with petroleum-derived diesel if needed, thus allowing its easy integration to the marketplace. The required technology for the production of green diesel is the same as the commonly used one over several decades in conventional refineries. The same available infrastructure such as the reactor, separation unit and the same hydrotreatment catalysts could be used for the hydrotreatment of different oils as triglyceride sources at an industrial level. These catalysts should be accessible, economically attractive for commercial application and non-harmful to environment.

Hence, nowadays, the main aspect of the green diesel process is to optimize the catalyst's characteristics and textural properties as the key points for this purpose. Moreover, finding the suitable process conditions and overcoming the technical difficulties are the main tasks both for the environment and economic sectors. In the following sections, different aspects, from the feed to the green fuel product via hydrotreatment reaction, are presented. The chemistry of hydrotreatment, different reaction pathways, various types of the heterogeneous catalysts, the main reaction process conditions and their effects on the green diesel product are also discussed.

1.2 The feedstock

Among different types of renewable energy sources such as solar power, hydropower, wind power, and fuel cells, biomass is the only type of renewable energy capable of storing the energy in the form of materials. These bio-based materials could be used directly as fuel or as raw materials to produce value-added products such as chemicals or polymers. Fuels produced from biomass have a high potential to replace conventional fossil fuels. Pyrolytic (bio-based), and vegetable oil are the main two types of liquid oils derived from biomass. Thermal decomposition of biomass in the absence of oxygen (fast pyrolysis) produce pyrolytic oil (bio-oil), biochar, and gases. A dark brown liquid is produced after the subsequent cooling and condensation. Pyrolytic oil is a mixture containing alcohols, ketones, acids, aldehydes, ethers, phenolic, and furans [4]–[6]. Pyrolytic oils have some drawbacks including: high acidity due to the presence of organic acids which could damage internal combustion engines (ICE) parts, very high oxygen contents, causing poor stability and non-immiscibility with petroleum-fuels, and low hydrogen to carbon ratio (H/C) arising from the low (H/C) of biomass feed. These drawbacks make different challenges and difficulties in the upgrading process of pyrolytic oils. The high water content of pyrolytic oil which decreases the heating value (about half that of conventional fuel oil), reduces the stability and causes catalysts deactivation during the upgrading process, and additionally, they are extremely malodorous [6]. These shortcomings have led to the increased interest in using vegetable oil as a source for production of green fuels.

Vegetable oils are produced via solvent extraction or cold press process from oil seeds. Vegetable oils consist of triglycerides with three fatty acid chains having carbon numbers in the ranges of diesel fuels. Compared to bio-oils, vegetable oils have higher carbon and hydrogen and lower oxygen contents. The H/C molar ratio of vegetable oils is in the range of about (1.6 and 2.4), which includes and covers the H/C molar ratio of petroleum-derived fuels that is about 2.0. Furthermore, the water content of vegetable oil is very low (0.03 to 0.47% wt.) compared to bio-oils (15 to 30% wt.) [4]. Present-day compression ignition (CI) engine, also called Diesel engine was invented firstly by Dr. Rudolf Diesel. The first operational Diesel's engine ran in the history on 10th August 1893 and the first time that a vegetable oil was used directly as fuel was in 1900 when Diesel used peanut oil as fuel in

Paris exposition. Nowadays, evolved CI engines are widely used in on-road/off-road purposes like transportation, military, agriculture, mining, sailing, and as power sources in under development zones, etc. This is due to their intrinsic durability (heavy-duty), higher torque, better fuel consumption and lower CO_2 emission comparing to spark ignited engines [7]–[9].

It is possible to use vegetable oils directly as fuel for a short period owing to their high-energy content in compression ignition (CI), however, prolonged utilization time leads to the formation of residue in engine parts. On the other hand, the higher viscosity of vegetable oils compared to fossil fuels cause some problems for pumping to the engines [10]. These disadvantages led to extensive research studies focused on upgrading triglyceride molecules to be used as green fuel. One of the first attempts to produce fuel from cracking of vegetable oils was done during the 1920s to 1930s. This technology was further studied to produce an emergency fuel alternative during world war II [11].

Lipid feedstock controls the properties and method used in biofuel production. The main component of lipid feedstock is triglyceride covering; vegetable oils, algae oils, WCO and animal fats [12]–[15]. This study is concentrated on vegetable oil as feedstock for production of green diesel. Various vegetable oils have been used in different countries as raw materials for production of green fuels owing to their good availability. Rapeseed oil and canola are used in Canada and European countries, soybean oil in the United States and palm oil in tropical countries including Indonesia and Malaysia whereas coconut oil is used for biofuel production in coastal areas. Potential non-edible oils used as lipid feedstock include jatropha cultivated mostly in Asia, Africa and South America, and karanja which grows mainly in India [16]–[19]. To mention some examples, several potential triglycerides sources for production of green diesel are presented in Table 1.1 [20].

Table 1.1. Worldwide current potential oil sources separated by countries [20].

Country/Feedstock	Country/Feedstock
Canada- Rapeseed / soybean / flax / mustard / animal fats / yellow grease	India- Jatropha / karanja / soybean / rapeseed / sunflower
Australia- Beauty leaf / jatropha curcas / karanja / waste cooking oil / animal tallow	Brazil- Soybeans / palm oil / castor / cotton oil
New Zealand- Waste cooking oil / tallow	China- Jatropha / waste cooking oil / rapeseed
Peru- Palm / jatropha	Argentina- Soybeans
Iran- Palm / Jatropha / castor / algae	France- Rapeseed / sunflower
Germany- Rapeseed	USA- Soybeans / peanut / waste oil
Ireland- Animal fats / frying oil	UK- Rapeseed / waste cooking oil
Cuba- Jatropha curcas, Moringa, Neem	Mexico- Animal fats / waste oil
Japan- Waste cooking oil	Malaysia- Palm oil
Philippines- Coconut / jatropha	Bangladesh- Rubber seed / karanja
Pakistan- Jatropha curcas	Thailand- Palm / jatropha / coconut
Singapore- Palm oil	Spain- Sunflower / linseed oil
Greece- Cottonseed	Italy- Rapeseed / sunflower
Turkey- Sunflower / rapeseed	Ghana- Palm oil
Zimbabwe- Jatropha	Kenya- Castor
Norway- Animal fats	Sweden- Rapeseed

To produce oil seed as a green fuel feedstock, the high per acre productivity, and the capability to grow on non-arable area are the important issues to be considered when an oil is selected to be industrialized [21], [22].

Vegetable oils found in nature contain a combination of triacylglycerol molecules (i.e., triglycerides). Triglycerides are the main part of all vegetable oils and fat structure, and the significant difference between various vegetable oils is the type of fatty acids attached to the triglyceride molecules. They are formed from a single molecule of glycerol combined with three molecules of fatty acid (chain) as presented in Figure 1.1. The side chains of

triglycerides could be saturated, mono-unsaturated or polyunsaturated. They are usually categorized based on their length and degree of saturation. The chain length of these fatty acids in naturally occurring triglycerides could be of varying lengths (from C12 to C20); but 16, 18 and 20 are dominant ones with a maximum of three unsaturated double bonds commonly in the position 9, 12 and 15 with cis orientation. The 9 and 12 positions are often dominant; for examples in linoleic fatty acid. Natural fatty acids found in plants and animals usually contain an even number of carbon atoms [23].

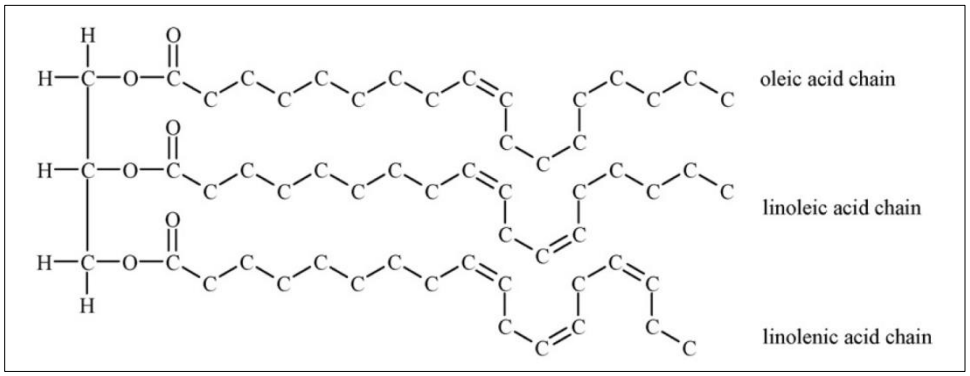

Figure 1.1. The basic structure of triglycerides with double bonds has the cis-configuration [24].

Triglycerides are of different types regarding to their fatty acid composition (saturated/monounsaturated/polyunsaturated, relative location on the glycerol molecule and isomeric forms). The main constituents of both oils and fats are triglycerides. In fact, triglycerides present in both oils and fats determine their final properties. One of their dissimilarity is their melting point, e.g., oils are liquid while fats are solids at ambient temperature. Saturated oils have higher melting points and better oxidation stability; and also greater degree of saturation means lower reactivity [25].

To mention some examples, the fatty acid composition of different vegetable oils are presented in Table 1.2.

Table 1.2. The typical fatty acid composition of oils derived from various vegetable oils [25], [26].

Fatty Acids	Structure	Typical composition (% wt.)						
		Corn	Karanja	Canola	Soybean	Sunflower	Palm	Rapeseed
Capric	C10:0	0.0	0.0	0.6	0.0	0.0	0.0	0.0
Lauric	C12:0	0.0	0.0	0.0	0.0	0.0	0.0	0.0
Myristic	C14:0	0.0	0.0	0.1	0.0	0.0	2.5	0.0
Palmitic	C16:0	6.5	6	5.1	11.5	6.5	40.8	4.9
Palmitoleic	C16:1	0.6	0.0	0.0	0.0	0.2	0.0	0.0
Stearic	C18:0	1.4	7	2.1	4.0	5.8	3.6	1.6
Oleic	C18:1	65.6	62	57.9	24.5	27.0	45.2	33.0
Linoleic	C18:2	25.2	17	24.7	53.0	60.0	7.9	20.4
Linolenic	C18:3	0.1	0.0	7.9	7.0	0.2	0.0	7.9
Arachidic	C20:0	0.1	3	0.2	0.0	0.3	0.0	0.0
Eicosenoic	C20:1	0.1	0.0	1.0	0.0	0.0	0.0	9.3
Behenic	C22:0	0.0	4	0.2	0.0	0.0	0.0	0.0
Erucic	C22:1	0.1	0.0	0.2	0.0	0.0	0.0	23.0

1.3 Conventional methods to produce fuel from oils

Both first generation biofuel and green diesel also trending as the second generation biofuel, can be produced from vegetable oils, but through different processes. Biodiesel is composed of fatty acid methyl esters (FAME) and is produced through transesterification, namely the reaction between triglycerides in the vegetable oils with an alcohol (often methanol) with the contribution of a catalyst as illustrated in Figure 1.2 [27].

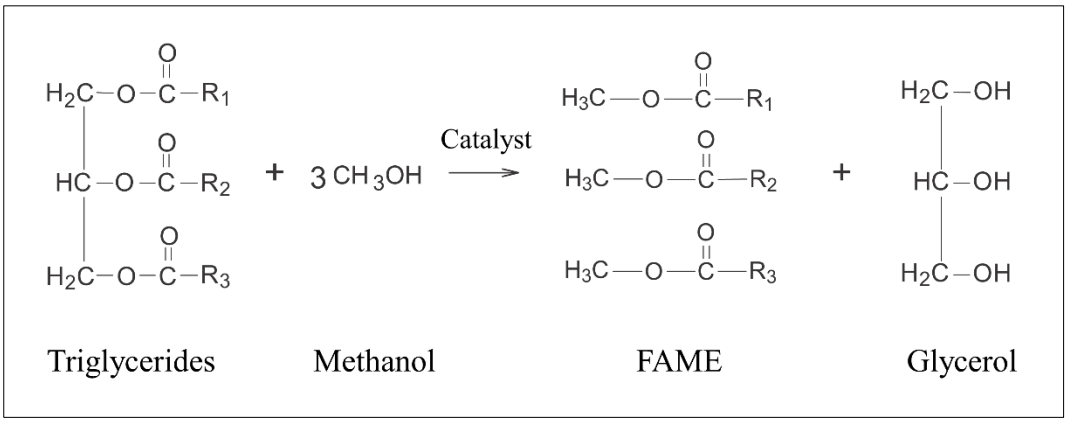

Figure 1.2. Transesterification of triglycerides with methanol to produce fatty acid methyl ester (FAME) or biodiesel [27].

Green diesel can be produced by hydroprocessing of triglycerides present in vegetable oil under high hydrogen pressure and high temperature in the presence of a heterogeneous catalyst to form n-alkanes as presented in Figure 1.3 [28]. Several different processes and catalysts can be used to produce green diesel. They will be described in the following sections.

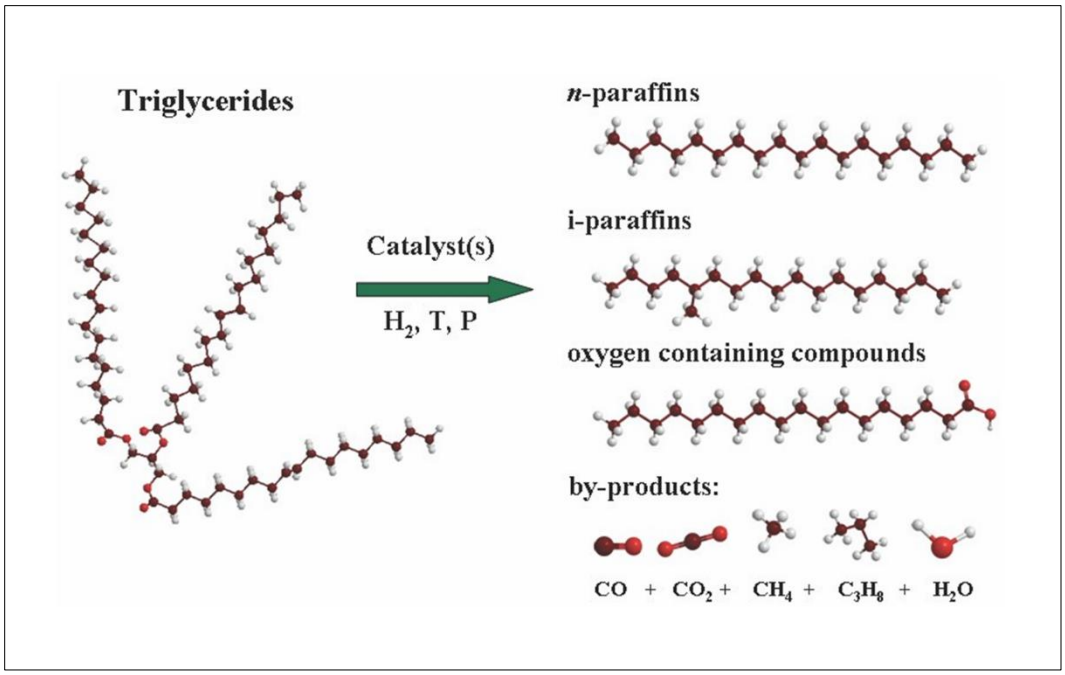

Figure 1.3. Hydrotreatment reaction scheme for green diesel production [28].

1.3.1 Mechanism of hydrotreatment

Briefly, the triglycerides are hydrotreated to alkanes via three main steps involving: (1) saturation of double bonds in the triglycerides molecules, (2) dissociation of the saturated triglycerides via hydrogenolysis to propane and fatty acids, and (3) oxygen removal of the formed fatty acids. Oxygen removal from triglycerides occurs through different reactions such as hydrodeoxygenation (HDO), decarbonylation (DCO), and decarboxylation (DCO_2) influencing the distribution of hydrocarbon products [3].

The triglycerides are transformed into hydrocarbons in the presence of catalysts; mainly to n-paraffin and propane at elevated temperature and hydrogen pressure producing H_2O, CO and CO_2 as by-products [29], [30]. Triglyceride conversions over hydrotreating catalysts in the presence of hydrogen is a complex reaction. It consists of parallel and/or consecutive reaction steps including saturation, cracking, HDO, DCO, and DCO_2 presented in Figure 1.4 [25].

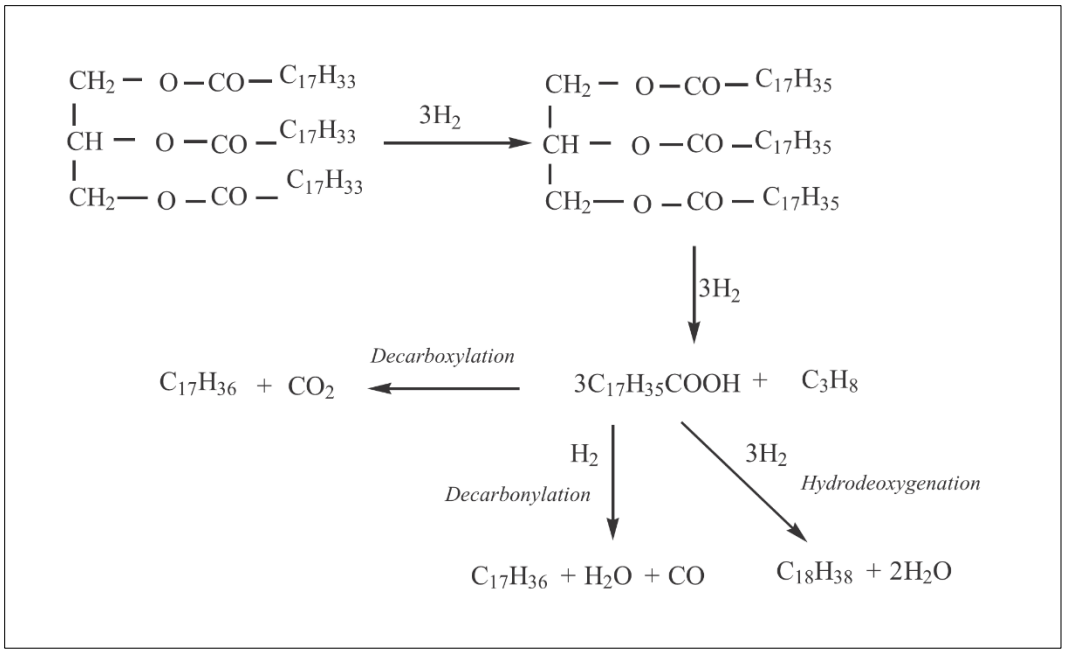

Figure 1.4. Possible deoxygenation pathways [25].

Hydroprocessing of highly unsaturated chain triglycerides requires higher hydrogen consumption compared to less unsaturated triglycerides chains to achieve the similar level of hydro converted fuel. Veriansyah et al. conducted the hydrodeoxygenation of soybean oil in a batch reactor system using commercial 57% wt. Ni/SiO_2-Al_2O_3 catalyst with catalyst/oil weight ratio of ≈ 0.04. During the reaction, two significant drops in hydrogen pressure were observed, presented in Figure 1.5. The first drop in hydrogen pressure took place in the temperature range of 100-130°C corresponding to the saturation of existing double bonds in the triglyceride molecules. The fatty acids chain containing double bonds in the feed were palmitoleic acid (C16:1), oleic acid (C18:1), linoleic acid (C18:2), alpha linolenic acid (C18:3) and eicosenoic acid (C20:1), which were respectively, converted into palmitic acid (C16:0), stearic acid (C18:0), and arachidic acid (C20:0). Further, increasing the temperature to around 270-330°C lead to the appearance of another drop in hydrogen pressure, which was attributed to the degradation of hydrogenated triglycerides into monoglyceride, diglycerides and free fatty acids which were then transformed into deoxygenated products [31].

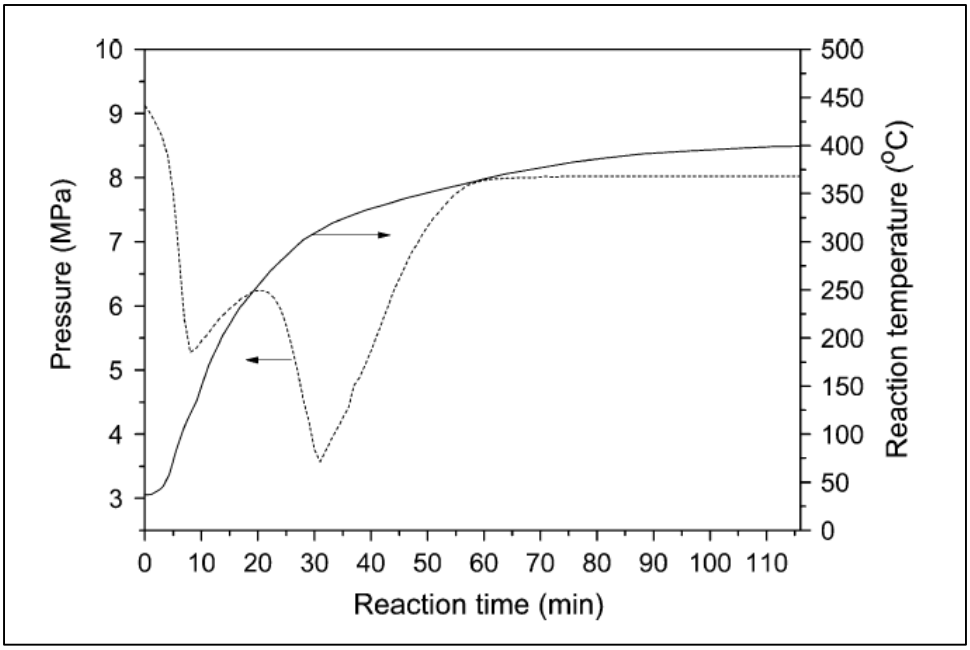

Figure 1.5. Representative pressure and temperature profile during hydrotreating of soybean oil using 57.6% wt. Ni/SiO_2-Al_2O_3. The catalyst to oil weight ratio was around 0.04 [31].

N-alkanes from free fatty acid can be produced through a single or a contribution of three different reaction pathways: hydrodeoxygenation (HDO), decarbonylation (DCO), and decarboxylation (DCO_2) [32]. The decarboxylation pathway converts the carboxylic acid group in the free fatty acids yielding straight chain alkanes by releasing CO_2. During this pathway, hydrogen is not consumed. It makes an n-alkane chain with one lower carbon than the corresponding free fatty acid.

$$R - CH_2 - COOH \rightarrow R - CH_3 + CO_2 \quad (1.1)$$

The DCO pathway produces alkanes by reacting the carboxylic acid group in the free fatty acids with hydrogen and generating CO and water. Similar to the DCO_2 pathway, the alkanes formed via decarbonylation have odd numbers of carbons in their chains.

$$R - CH_2 - COOH + H_2 \rightarrow R - CH_3 + CO + H_2O \quad (1.2)$$

Contrarily, the HDO pathway yields alkanes with even numbers of carbon atoms by reacting the carboxylic acid with hydrogen and producing water leading to the formation of an n-alkane chains having the same length as the corresponding free fatty acid.

$$R - CH_2 - COOH + 3H_2 \rightarrow R - CH_2 - CH_3 + 2H_2O \quad (1.3)$$

If the reaction goes through HDO, the produced n-alkanes will have the same carbon number as the corresponding fatty acid, whereas if it goes through DCO-DCO_2, the resulting n-alkanes will have one carbon less than the carbon numbers of initial fatty acid [33].The ratio of n-alkanes with odd numbers of carbon atoms to n-alkanes with even numbers of carbon atoms (e.g., C15/C16 and C17/C18) could be used as a sign for evaluating the reaction pathways of either DCO-DCO_2 or HDO [34]. Besides these three reaction pathways, a series of reactions such as isomerization, cyclization, and cracking can produce iso-alkanes, aromatics and lighter hydrocarbons. By-products, such as carbon dioxide, carbon monoxide and water generated during hydroprocessing reaction can contribute in a methanation and water-gas-shift side reaction at the same time.

Water gas shift: $CO_2 + H_2 \leftrightarrow CO + H_2O$ (1.4)

CO Methanation: $CO + 3H_2 \leftrightarrow CH_4 + H_2O$ (1.5)

CO_2 Methanation: $CO_2 + 4H_2 \leftrightarrow CH_4 + 2H_2O$ (1.6)

The water molecules (even in small quantity) produced in HDO pathway could be problematic while using sulfide catalysts in hydrotreatment due to the acceleration of sulfur leaching from the catalysts that consequently reduces the lifetime of the catalysts [35].

When DCO-DCO_2 pathways are dominant, the hydrogen is idyllically consumed for the saturation of feed's double bonds and stabilization of the catalyst while most of the oxygen molecules are removed as carbon oxides [36].

Hydrogen consumption follows the trend of HDO > DCO > DCO_2. In the economic point of view, catalysts and process conditions favoring the DCO-DCO_2 reaction pathways are favorable [37].

1.3.2 Advantages of green diesel over FAMEs (biodiesel)

Hydrotreated vegetable oils or green diesel have several advantages over FAMEs as transportation fuels. Due to the differing chemical compositions, biodiesel and green diesel have significantly different fuel properties [38]. Green diesel has similar chemical composition with conventional petrodiesel, and thus can be used in the current diesel engines without any modification. Moreover, the same distribution infrastructures (pumps, pipelines, fuel stations, etc.) can be utilized for green diesel. Current petroleum refineries can also be used for green diesel production via hydrotreatment [25].

Biodiesel contains oxygen atom in its chemical structure whereas chemical compounds in green diesel do not bear oxygen and this is the most significant difference between them. The presence of oxygen in biodiesel causes a reduction in heating value. These low heating values are due to less exothermic ignition of oxygenated compounds, and a reduction in fuel oxidation stability compared to green diesel [39]. Hydrodeoxygenated fuels have superior blending properties with hydrocarbon fuels due to their zero oxygen content and unsaturated bonds compared to FAMEs. FAMEs also have other disadvantages such as low pot-life (due to a high degree of unsaturation), low corrosion resistance (moisture presence) and undesirable low-temperature properties (i.e., pour point and cloud point) which makes them undesired for cold climates [40]. Contrary to FAMEs, hydrodeoxygenated fuels exhibit excellent low-temperature properties, high heating value and high cetane number. In the case of green diesel, the low-temperature properties strongly depend on processing conditions and catalyst type, and the final n-alkane products could have the carbon numbers same as those of gasoline, jet fuel or diesel. For instance, catalysts with stronger acid sites produce lighter hydrocarbons due to the higher cracking acid sites which also can increase isomerization degree of the product. It is well known that process conditions affect the chemical composition of the final fuel. For instance, if green diesel is produced at higher temperatures, a larger amount of isomerized alkanes and short chain n-alkanes will be formed. Thus, it would be possible to improve the fuel's low-temperature properties. Freezing points of normal and isoparaffin as a function of carbon atom number are presented in Figure 1.6. A significant reduction in freezing point is observed for isomerized paraffin compared to normal paraffin [34], [41], [42].

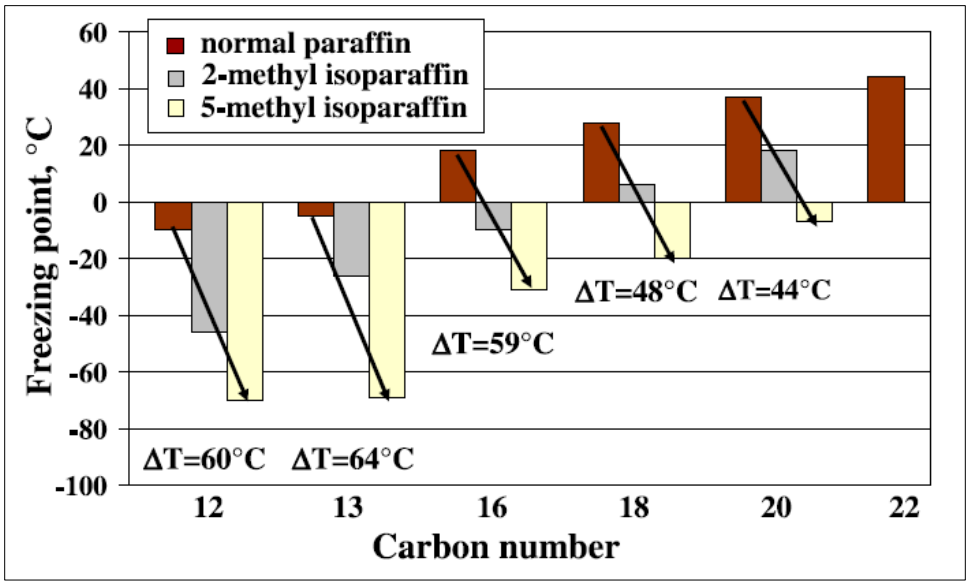

Figure 1.6. Freezing points of normal and isoparaffin as a function of carbon atom number [42].

Hydrogenation and cracking during hydrotreatment cause less dependency on the content of free fatty acids in the vegetable oils, whereas the fatty acid type and content influence the properties of FAMEs. Also, hydrotreatment does not produce byproducts such as glycerol; green diesel co-product is propane which can be used as fuel gas in the green diesel production factories (i.e., not sensitive to co-product prices) [43]. Moreover, current technology for FAMEs production utilizes mostly homogeneous catalysts such as NaOH which are consumed in the process and must be repurchased; they also need to be neutralized and separated from the product. In green diesel production, however, deactivated used heterogeneous catalysts could be easily separated from the products and regenerated to be reused [34], [36], [44].

1.4 Catalysts

1.4.1 Metal supported catalysts

The suggested hydrotreating reactions are carried out in hydrogen-rich atmosphere in the presence of a catalyst to form n-alkanes. Inside the reactor, catalysts operate for two main goals. In high-pressure hydrogen atmosphere, saturation of double bonds in the side chains of triglycerides is caused by the metal function of the catalyst while cracking of the C-O

bonds and isomerization of the formed n-olefins are dependent on the acid function of the catalyst. Selecting an appropriate catalyst is a major step which greatly affects the composition of the products. Two groups of catalysts namely; precious noble metals (i.e., Pd and Pt) and promoted transition metals catalysts (i.e., NiMo, CoMo, NiW, etc.) were used for triglycerides hydrotreatment [14], [37]. The main drawbacks of noble metal catalysts for hydrotreating are poor availability and high cost both limiting their potential application in industry. The prices of palladium, platinum, nickel and molybdenum metals are presented in Table 1.3 [45].

Table 1.3. Examples of noble and transition metals prices [45].

Metals	Palladium	Platinum	Nickel	Molybdenum
Prices (USD)	29.79/g	31.44/g	10.71/kg	16.00/kg

Attempts have been concentrated on the hydrotreatment of triglycerides on transition metal sulfide catalysts and noble metal catalysts. Traditional hydrotreating catalysts like NiMo or CoMo were found to be suitable for hydrodeoxygenation of triglycerides (which represents more than ≈ 95% by weight of vegetable oils).

In 1984, Nunes studied the hydrocracking of vegetable oils in his Doctoral thesis at Université Pierre et Marie Curie. In his thesis, he reported the hydrocracking of soybean oil in a batch reactor, with the utilization of hydrogenating rhodium base catalyst [46]. Šimáček et al. investigated the hydroprocessing of rapeseed oil into green diesel at various temperatures (260-340ºC) under the pressure of 70 atm in a continuous flow reactor using three different types of commercial NiMo/γ-Al_2O_3 catalysts. Prior to the experiments, the catalysts were sulfided using 5% solution of dimethyl disulfide (DMDS) in iso-octane. The final liquid product consisted mainly of C17, iso-C17, C18 and iso-C18 hydrocarbons at reaction temperatures higher than 310°C, whereas at a lower temperature, unconverted triglycerides and free fatty acids were detected [41]. The obtained result was in accordance with the findings of Huber et al., that studied the production of liquid alkanes with a carbon

number from 16 to 20 through hydrotreating of sunflower oil and a blend of sunflower-heavy vacuum oil [32]. In a study done by Şenol et al., using methyl ester as feed, NiMo/γ-Al_2O_3 promote more hydrocracking and hydrodeoxygenation (HDO) compared to CoMo/γ-Al_2O_3 [47].

1.4.1.1 Textural properties of support

The dispersion of the catalysts' active phases is enhanced by using a support; it also permits a higher loading of active metals in the catalyst system. The nature and textural properties of support such as specific surface area, pore volumes, pore diameter and crystallite domain size significantly affect the properties of the catalysts, influencing the hydrotreatment process.

These physical specifications play essential roles in the hydrotreatment reaction. In the hydrotreatment of triglycerides, high surface area and large pore diameter enhance the catalytic activity. The pores of the support should be large enough to allow the triglyceride molecules to access to the active metals and let enough motions inside the pores. Since the reactions take place on the surface of catalyst, a large surface area is required. Indeed, the support is used for uniform distribution of the metal over a large surface area. The relative sizes of reaction components are depicted in Figure 1.7 [48].

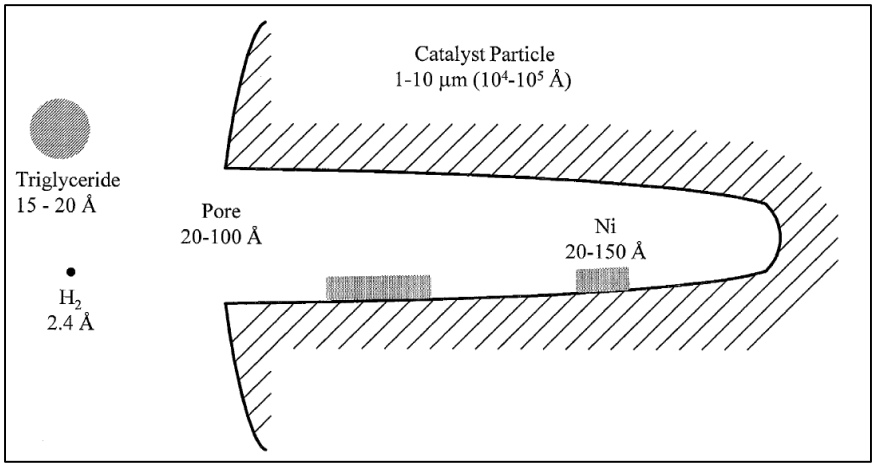

Figure 1.7. Relative sizes of reaction components [48].

The triglyceride size can be estimated from the dimension of, for example, methyl oleate (around 2.5 nm length) and glycerol (around 0.6 nm). Even assuming that relevant dimension of triglyceride molecule is the dimension along the fatty acid chain (considering triglyceride

can also enter into the pores along their smallest diameter which is around 0.6 nm in the glycerol part), supports having mesopores would facilitate the penetration of bulky triglyceride molecules [49].

The γ-alumina, zeolites and activated carbon are conventionally used as catalysts support. Zeolites have small pore diameters which are inaccessible for the bulky triglycerides molecules. Moreover, the high acidity of zeolites results in an excess cracking yielding light fraction products [50]. Hydrotreatment of triglycerides favors the accumulation of coke species on the surface of the catalysts. The use of activated carbon as support, makes it impossible to regenerate the catalyst via simple combustion method in the air and remove these deposits [51]. High mechanical and thermal stability of alumina make it a good candidate to be used as catalyst support. Organized tunable mesoporous γ-alumina have high surface area and appropriate pore diameters to be employed as hydrotreatment catalyst supports. The mild acidity of the γ-alumina results in a moderate cracking and leads to the formation of products in the diesel range. Furthermore, this support could be regenerated by burning off the deposited coke in the air at high temperature [37]. In a study done by Sotelo et al., in the hydrotreatment of rapeseed oil, it was found that the sulfided NiMo/γ-alumina catalyst is a good candidate for hydrotreating process due to its hydrogenation activity, slight acidity and low cost as compared with Pt-Zeolitic based catalysts. Also, it has been shown that sulfided NiMo/γ-Al_2O_3 catalyst effectively promotes the hydrocracking of triglycerides at lower pressures and temperatures. Due to the moderate acidity of sulfided NiMo/γ-Al_2O_3 catalyst, the products consist mainly of n-C17 and n-C18. In the case of Pt-Zeolite catalysts, however, the small pore diameters and enhanced cracking caused by acidity lead to a lower diesel fraction yield [52]. Liu et al. used jatropha oil as a triglyceride source and loaded NiMo catalyst on different supports to investigate the effect of acidity of supports in the final product composition. Among selected supports, the acidic strength was in the order of SiO_2-Al_2O_3 > γ-Al_2O_3 > SiO_2. It was reported that NiMo/SiO_2 showed the highest yield of C15-C18 n-alkanes due to the negligible amount of cracking and isomerization.

In the case of NiMo/γ-Al_2O_3, the light paraffins increased compared to NiMo/SiO_2. Finally, NiMo/SiO_2-Al_2O_3 formed higher amount of cracked products due to higher acidity. The FID-

GC charts of liquid products from the hydrotreatment of jatropha oil for these three catalysts are presented in Figure 1.8 [53].

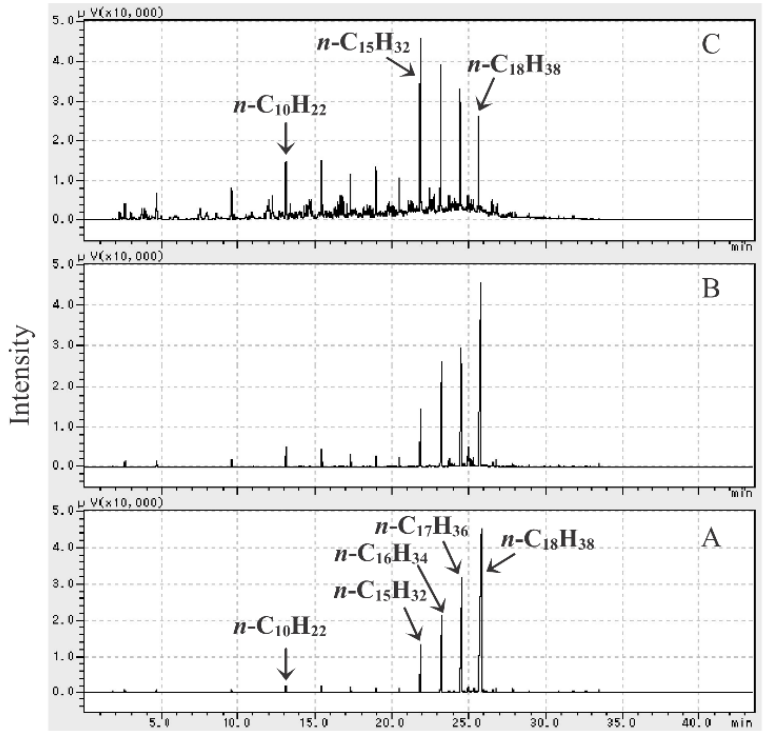

Figure 1.8. GC-FID charts (capillary column) of the liquid hydrocarbons formed from the hydrotreatment of jatropha oil over various catalysts: (A) NiMo/SiO_2, (B) NiMo/γ-Al_2O_3, (C) and NiMo/SiO_2-Al_2O_3 [53].

1.4.1.2 Method for fabrication of mesostructured alumina

As previously mentioned, heterogeneous catalysts were loaded on porous supports. Among various supports, mesoporous alumina showed satisfactory properties and is widely used in catalysis industries. Hence, the control of textural properties of the alumina, such as specific surface area (S_{BET}), pore volume, pore diameter and pore structure, have initiated lots of attention. From different synthesis methods, templating methods, particularly the self-assembly involving one, is of the greatest interest. This method not only allows the formation of a highly ordered mesoporous structure with high surface area alumina, but also makes the modification of the alumina properties possible for use in a wide range of applications [54].

This method was further expanded by introduction and incorporation of structure directing agent of triblock copolymer poly (ethylene oxide)$_{20}$ - poly (propylene oxide)$_{70}$ - poly (ethylene oxide)$_{20}$ (Pluronic P123) which was used as a soft template. Pluronic P123, an amphiphilic molecule, consists of two polymer chains having different properties, which makes possible the formation of micelles in a solution. The structure directing agent forms micelles in the solution and the consequent hydrolysis and condensation of the alumina precursor occur around the micelles to form the porosity. Once the synthesis step is completed, the polymeric template is removed via a calcination process and ordered mesoporosity is reached [55].

Various research groups had worked on the fabrication of mesoporous alumina to optimize its textural characteristic and properties. Wu et al. showed the effect of polymeric template concentration on the formed mesoporous alumina properties. It was reported that the polymeric template intensely affects the characteristics of the mesoporous alumina. It was also shown that at high concentrations of the polymeric surfactant, the final pore size distribution was broadened due to the reduced mobility of the synthesis solution, however their synthesized material did not have any worm-hole like structure [56], [57]. In another work done by Sun et al., the dependency of pore diameters to the calcination temperature in a mesoporous alumina was studied. They revealed that the calcination temperature of 550ºC led to the formation of amorphous alumina, while at higher temperatures a crystalline alumina is formed. Their results also showed that the pore diameter increased by increasing the temperature [58]. Suzuki and Yamauchi also performed the synthesis of mesoporous alumina using a mixture of surfactant and polystyrene nanoparticles as a template. They investigated the effect of calcination temperature on the textural properties of the mesoporous alumina showing that by increasing the calcination temperature from 500 to 900ºC, the specific surface area decreased while the pore diameters increased [59].

In all, making ordered mesoporous alumina is possible through sol-gel assisted via EISA method using copolymer structure directing agents. To further expand their textural properties, widening the application as heterogeneous catalyst support for the hydrotreatment of triglycerides, the effect of polymeric template concentration and calcination temperature on the properties of the mesoporous alumina will be discussed in Chapter 2.

1.4.1.3 One-step catalyst synthesis via sol-gel method

When a material is used as catalyst, an improvement would be the introduction of the active metals into the alumina framework during the synthesis step which could be designated as a modified sol-gel synthesis.

Generally, two main methods applicable for the fabrication of catalysts are the conventional impregnation of the active metals on the support and the one-pot sol-gel assisted synthesis method. In the former, first the mesoporous support is prepared and then the active metals are impregnated on the porous structure, while in the latter, the alumina precursor and the active metal are mixed and the porous structure is formed in the presence of these active metals. In a one-pot sol-gel assisted synthesis method, like the simple sol-gel method, the porosity is acquired through the addition of the polymeric structure directing agent template. In the impregnation method, the active metals are on the surface of the mesoporous alumina, while in one pot sol-gel assisted synthesis method, they are located inside the alumina framework. It is possible to produce a mixed oxide catalyst after a controlled calcination.

Sol-gel derived catalysts, were reported to exhibit higher stability over time compared to their impregnated counterparts. The stability of sol-gel derived catalysts was demonstrated in different chemical reactions. Savva et al. found that Ni/Al_2O_3 is a promising hydrogenation catalyst and also reported the efficiency of the sol-gel technique for better dispersion of the nickel phase [60]. Bykova et al. confirmed that among different Ni-based catalysts, those prepared by the sol-gel method possessed the highest activity for the hydrodeoxygenation of guaiacol [61]. Newnham et al. performed the preparation of Ni/Al_2O_3 via two methods of template-assisted (Ni 10% wt. MAl) and wet impregnation (Ni 10% wt. γ-Al_2O_3) techniques and used them for the dry reforming of methane. The impregnated catalyst showed a loss in activity after 4 h, while Ni/MAl exhibited a very high stability over time up to 200 h. This better stability was reported to be caused by the formation of nickel nanoparticles which are highly stable toward migration and sintering throughout the reaction. This high stability was stated to be due to the strong interaction of the nickel particles with the support and the confinement effect of the nickel particle in the mesoporous framework of the support. Carbon deposition was also significantly lower for the Ni/MAl compared to the impregnated catalyst [62]. Tian et al. performed the CO methanation at elevated temperature, using alumina-

supported nickel (10% wt.) catalysts. The incorporation of nickel into the organized mesoporous alumina (sol-gel), resulted in a higher stability and lower carbon deposition compared the impregnated catalyst. This higher stability was reported to be due to the lower sintering tendency (confinement of nickel) of the sol-gel catalyst [63].

In conclusion, only by using continuous reactor it is possible to produce large amounts of green diesel. Thus the higher stability and the lower tendency of coke formation are essential properties of the catalyst. Up to now, most of the catalysts used for the hydrotreatment of triglycerides are produced via impregnation. The preparation of the sol-gel one-pot assisted catalysts (incorporation of active metals during synthesis step) and their use for the green diesel production is anticipated to the lead to the development of performant catalysts.

As will be discussed in Chapter 3, the prepared mesoporous γ-alumina was used as catalysts support. The two NiMo/γ-alumina and CoMo/γ-alumina catalysts were prepared via impregnation method and their efficiency for green diesel production was evaluated.

The monometallic Ni/γ-alumina catalyst fabricated via one-pot sol-gel assisted technique was also used for the hydrotreatment of canola oil. To compare the two synthesis methods, Ni/γ-alumina catalyst was also synthesized using the mesostructured γ-alumina support via impregnation and sol-gel techniques and the results are presented in Chapter 4.

1.4.2 Catalytic deoxygenation of triglycerides and fatty acids over sulfided catalysts

Metal sulfide supported catalysts have been widely studied because of their appropriate hydrodeoxygenation activity. They are generally made of alumina-supported MoS_2 promoted by Ni or Co. These catalysts usually are stored in their inactive oxide form because of easier handling and loading compared to fully sulfided catalysts. Therefore, to use them for the hydrotreatment of triglycerides, these catalysts should be first activated by a sulfiding agent either in-situ, i.e., directly inside the hydrotreating reactor or ex-situ using an organosulfide agent (CH_3-S-CH_3, CH_3-S-S-CH_3, polysulfides…) or H_2S gas [64]. The drawback associated with utilizing the sulfiding agent in the feed is that the coke could accumulate on the surface of catalysts before sulfidation. For this purpose, besides the addition of sulfiding agent in the feed, ex-situ pre-sulfidation is necessary to activate the catalyst and prevent the primary coke

formation on the surface of the catalyst which affects the overall catalyst behavior with time on stream. The presence of oxygen in the triglycerides molecules tends to remove the sulfur from the catalysts. Hydrogen also removes the sulfur from the catalyst. Furthermore, the bio feedstocks used to produce green fuel contain very low amount of sulfur. Therefore, up to 1-2% wt. of sulfiding agent is added to the feed in order to keep the active metals in their sulfided form. In a study done by Wei-qian et al., CoMoS/γ-Al_2O_3 and CoMo/γ-Al_2O_3 were used for the hydrotreatment of jatropha oil using a continues flow system in a fixed-bed reactor. The obtained results showed that the sulfided catalyst enhanced the conversion compared to non-sulfided catalyst under the same reaction conditions [65]. Kubicka and Horáček demonstrated that adding DMDS continually during the hydrotreatment of rapeseed oils significantly decrease catalyst deactivation, however, the degradation of active sulfur sites was not entirely reversible [66]. Liu et al. showed that removing sulfur from sulfided NiMo catalyst during the reaction caused the catalyst deactivation. It was reported that the deactivated catalyst can be regenerated via sulfidation process [12]. Şenol et al. studied the effect of the presence of H_2S in the deoxygenation of the aliphatic compound. NiMo/γ-Al_2O_3 and CoMo/γ-Al_2O_3 were used as catalysts and the reaction was done in a fixed-bed reactor under the pressure of 1.5 MPa. The obtained results confirmed the positive effect of introducing H_2S on the activity of the catalyst. They suggested that this increase in catalyst activity could be attributed to the augmentation of the acidic sites of the catalysts [67]. The sulfiding agent in the feed maintains the catalysts in sulfided form by producing H_2S. Moreover, it compensates for the activity loss of the catalyst caused by leaching. In the study done by Zhao et al. on the hydrotreatment of rapeseed oil using NiMo/Al_2O_3 a higher deactivation of the catalyst was observed in the absence of a sulfiding agent co-feeding was presented [35], [68].

1.4.3 Catalytic deoxygenation of triglycerides and fatty acids over non-sulfided catalysts

As mentioned in the previous section, transition metal catalysts supported on alumina show appropriate properties for the hydrotreatment of triglycerides oil. Nevertheless, these catalysts are used in their sulfided forms. To maintain them active, it is required to sulfide them with H_2S and also to introduce a sulfiding agent material in the feed. This needs

additional equipment such as corrosion resistant storage tank and pump which adds the extra cost of sulfidation. This sulfur has been reported to leach from the catalysts during the reaction. The sulfur contents of vegetable oils are very low; thus, the SO_x emission of the produced hydrocarbons burning is negligible [69]. Introduction of sulfur and the consequent sulfur leaching might contaminate the final hydrocarbons reducing their quality. Sulfur is environmentally hazardous and very toxic to human health. Moreover, it causes corrosion to the infrastructures [44], [70]. Therefore, due to the mentioned drawbacks associated with sulfide catalysts, sulfur-free metal catalysts are of prime interest to be used to upgrade triglycerides feedstock's via hydrotreatment to aliphatic hydrocarbons. Gousi et al., demonstrated the effectiveness of nickel-alumina co-precipitated catalysts for the deoxygenation of sunflower oil. The deoxygenation was conducted in a semi-batch reactor at 310ºC and a hydrogen pressure of 40 bar. The main liquid products were C15 to C18 hydrocarbons with a maximum of C17, and the prominent pathway was the DCO-DCO_2 route [71]. Hachemi et al. prepared 5% wt. Ni/γ-alumina catalyst using commercial γ-alumina by employing the wet-impregnation technique. They used stearic acid as a model compound in a semi-batch reactor at 300ºC and hydrogen pressure of 30 bar. The DCO-DCO_2 are the dominant routes over reduced Ni/γ-alumina [72].

Kim et al. performed the hydrodeoxygenation of refined soybean oil in an autoclave reactor. They used both sulfided (NiMo/γ-alumina and CoMo/γ-alumina) and reduced (Pd/γ-alumina and Ni/γ-alumina) catalysts. It was reported that the reduced metal catalyst showed higher activity over DCO-DCO_2 pathways while the sulfided ones favored the HDO pathway [73]. Yenumala et al., prepared Ni supported catalysts by using different commercial supports namely; γ-alumina, SiO_2 and HZSM-5 and studied the hydrodeoxygenation of karanja oil in a semi-batch reactor. In order to accomplish hydrogenation of triglycerides unsaturated double bonds, the temperature was adjusted to 200ºC at a hydrogen pressure of 20 bar over the catalysts. They showed that the pure support provides more light fraction compared with their corresponding catalysts revealing the effect of acidity of the supports on cracking. Among these catalysts, γ-alumina displays superior activity for the hydrodeoxygenation with the lowest tendency to cracking which makes possible the formation of diesel range hydrocarbons by the preserving backbone chains of the triglyceride fatty acids intact [74]. Santillan-Jimenez et al. conducted the catalytic hydrodeoxygenation of fatty acids over

carbon-supported nickel and palladium catalysts in a semi-batch reactor. Both 5% wt. Pd/C and 20% wt. Ni/C revealed that both catalysts produce hydrocarbons. Among the employed gases of N_2, H_2/N_2 of 10/90 and H_2, the highest catalytic efficiency was found under pure hydrogen gas [75]. These results are in agreement with a study done by Veriansyah et al., in the hydroprocessing of soybean oil using a batch reactor. Both sulfided (CoMo and NiMo) and reduced (Ni and Pd) catalysts were examined for the hydroprocessing. Hydroconversion trend was found to be as follows: Ni (95.5%) > NiMo (91.9%) > Pd (90.9%) > CoMo (79.9%) at the catalyst weight ratio of 0.09 suggesting that both sulfided and reduced catalysts are effective. Figure 1.9 presents the effect of these catalysts on the conversion and selectivity [31].

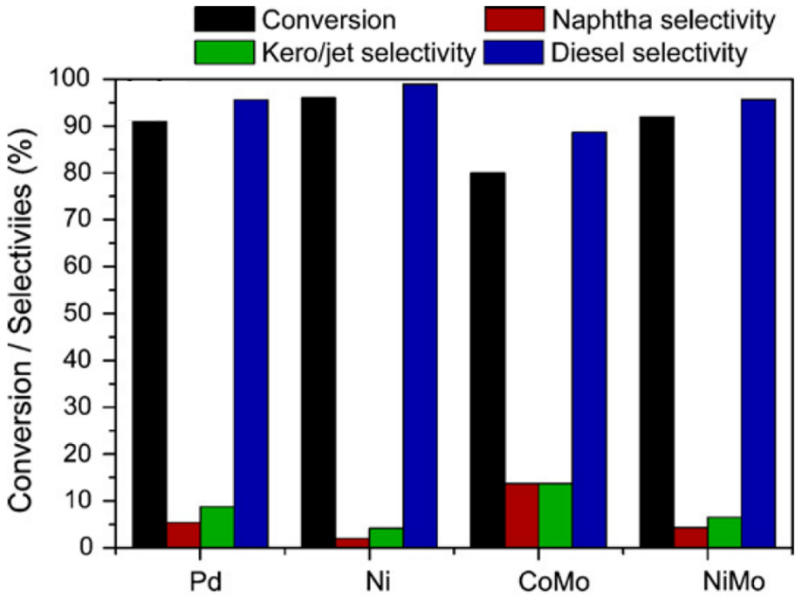

Figure 1.9. Conversion and various fraction selectivities over reduced (Pd and Ni) and sulfided (CoMo and NiMo) catalysts. Temperature: 400ºC, H_2 pressure: 92 bar, reaction time: 2 h and catalysts/oil weight ratio: 0.09 [31].

In another study, Santillan-Jimenez et al. found that the catalytic activity of Ni-Al layered double hydroxide catalyst is better than that of 20% wt. Ni/Al_2O_3 catalyst for hydrotreatment of fatty acids in a semi-batch reactor [51], [76]. They also used the same catalyst in a fixed-bed continuous reactor for the hydrotreatment of algae lipid to fuel-like hydrocarbons. It was suggested that the higher amount of unsaturated fatty acids chain in the feed increased the

coke formation by acting as a poison on the surface of the catalyst or as a precursor for coke deposition. It was also reported that the formation of coke leads to the pores blockage and restricts the access of the reactants to the active sites [77]. Santillan-Jimenez et al. also found that the appropriate reaction temperature is 300ºC. However, in all their experiments, the triglycerides/fatty acids in the feed concentration was very low [78].

Srifa et al. used commercial γ-alumina as support for preparation of Ni, Co, Pd and Pt monometallic catalysts via incipient wetness impregnation. Hydrodeoxygenation of palm oil to produce green diesel was done in a fixed-bed continuous reactor at 330ºC, H_2 pressure of 5 MPa, liquid hourly space velocity of 1 h^{-1} and the H_2/oil ratio of 1000 cm^3/cm^3. The catalysts were denoted 5NiAl, 10NiAl, 5CoAl, 10CoAl, 2PdAl, 5PdAl, 2PtAl and 5PtAl where the prefix number represents the metal concentration in % wt. Hundred percent conversion was achieved for all catalysts except for 2PdAl and 2PtAl reaching around 95% of conversion. DCO-DCO_2 pathways are dominant over Ni, Pd and Pt catalyst whereas over Co catalysts HDO is the dominant pathway. For Ni and Co catalysts, the formation of a slight amount of C8 to C14 hydrocarbons in the liquid product indicated the non-negligible cracking ability for these catalysts. The HDO and DCO-DCO_2 contribution over these different catalysts are presented in Figure 1.10 [37].

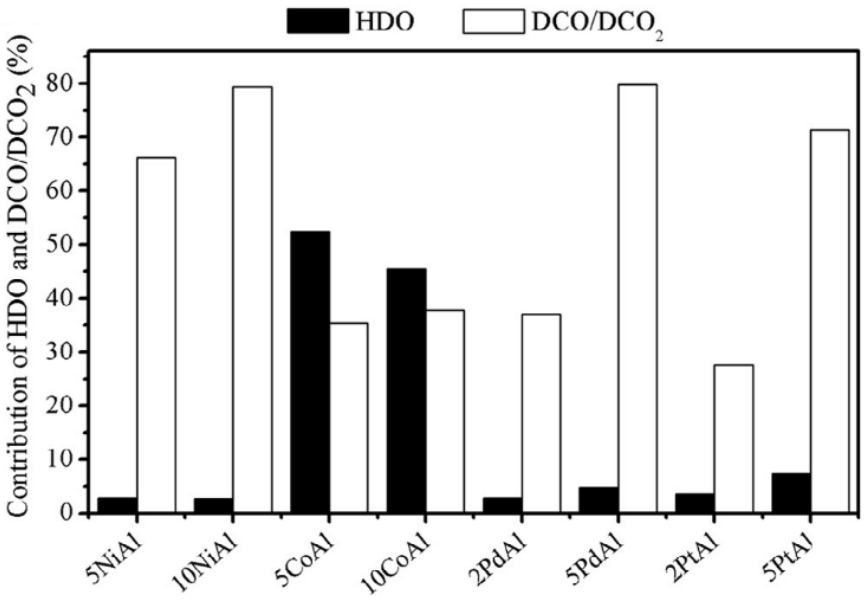

Figure 1.10. HDO and DCO-DCO_2 (%) contribution in the hydrodeoxygenation of palm oil over different monometallic catalysts. Temperature:330ºC, LHSV: 1 h^{-1}, H_2 Pressure: 50 bar and H_2/oil: 1000 cm^3/cm^3 [37].

In another study done in the same group, Ni/γ-alumina and Co/γ-alumina with 10% wt. Ni or Co loading were prepared using commercial γ-alumina via incipient wetness impregnation method [79]. The catalytic behavior of the catalysts was studied at 573 K, the H_2 pressure of 5 MPa, LHSV: 1 h^{-1} and the H_2/oil ratio of 1000 cm^3/cm^3 for the continuous hydrodeoxygenation of palm oil. DCO-DCO_2 reaction pathways are more dominant over Ni/γ-alumina compared to Co/γ-alumina which is in good agreement with the previously reported results from the same group [37]. The dispersion of the nickel particles is found to be better than the cobalt particles showing less aggregation and cluster formation. It was also noted that the nickel and cobalt particle sizes are considerably larger than the pore diameter of the commercial γ-alumina support and consequently most of the loaded active metals are located on the exterior side of the catalyst pores. From TEM observations and XRD results, it was also suggested that sintering is the minor reason for catalysts deactivation, whereas carbon deposition on the surface of the catalysts is the main reason. Moreover, it was reported that Co catalyst deactivates faster than Ni catalyst resulting in the formation of higher carbon

deposited on the catalyst surface. It was also shown that both catalysts could be regenerated and reused. The XRD patterns of the catalysts in calcined, pre-reduced, spent and regenerated states (Figure 1.11) and the TEM micrographs in pre-reduced, spent and regenerated forms and their corresponding particle size distributions are presented in Figure 1.12 [79].

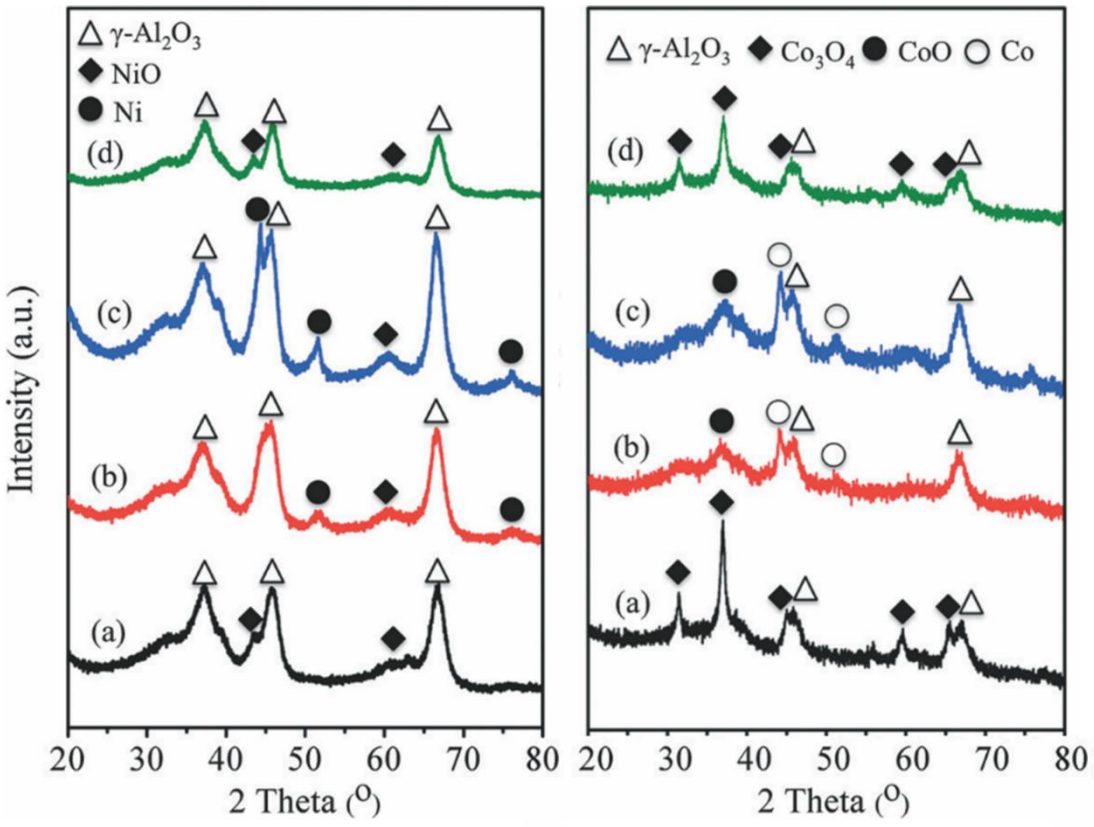

Figure 1.11. XRD patterns of (left) Ni/γ-alumina and (right) Co/γ-alumina in (a) calcined, (b) pre-reduced, (c) spent and (d) regenerated states [79].

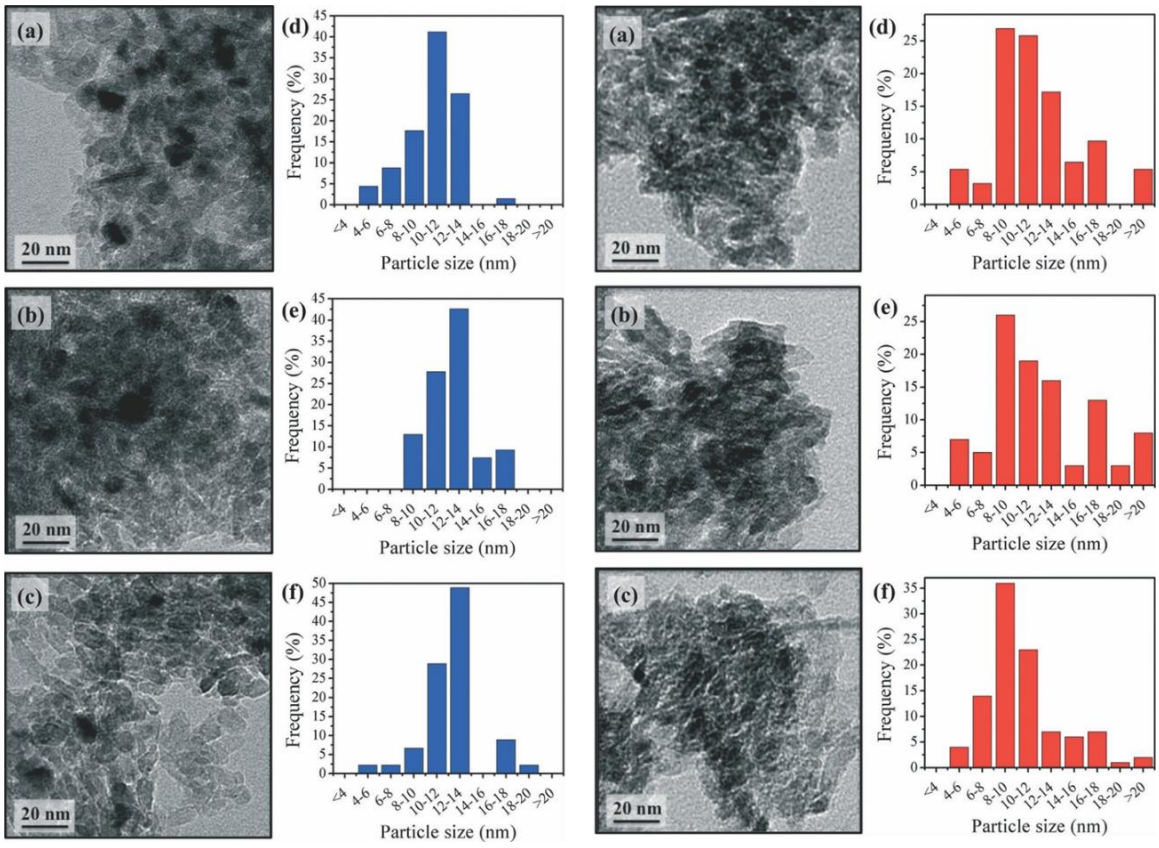

Figure 1.12. TEM images of (left) Ni/γ-alumina and (right) Co/γ-alumina and their corresponding measured particle size distributions of (a) pre-reduced (b) spent and (c) regenerated [79].

Kaewmessri et al. showed that the chicken fat could be successfully used as triglyceride source for green diesel production in a continuous reactor. The 10% wt. Ni/γ-alumina catalyst was prepared using commercial γ-alumina via conventional impregnation method. The process conditions were as follows: T:330ºC, P:50 bar, H_2/fat: 1000 cm^3/cm^3 and LHSV ranging from 0.5 to 2 h^{-1}. The catalyst favored DCO-DCO_2 reaction which is in agreement with the previously mentioned literature on Ni/γ-alumina catalysts reported in [37], [79]. Also, it was found that a shorter contact time of the reactant and the catalysts results in a lower green diesel yield [15].

In conclusion, both commercial sulfided supported transitional bimetallic NiMo and CoMo catalysts, and monometallic supported Pd and Ni catalysts are promising candidates for hydrodeoxygenation of triglycerides. However, the high cost and lesser accessibility of

palladium compared to nickel, cobalt and molybdenum limit the wide use of Pd based catalysts [45]. Hence, investigation and optimization of the efficiency of low-cost non-noble metals catalysts such as bimetallic NiMo/γ-alumina, CoMo/γ-alumina and monometallic Ni/γ-alumina for triglyceride conversion would be of prime importance.

1.5 Hydrotreating of vegetable oils

Biomass-derived feedstocks contain oxygenated compounds which lower the chemical stability and energy content of the fuel. When oils are used as liquid biomass, it is possible to transform them into hydrocarbons using a catalyst. To acquire a liquid green fuel, having combustion properties similar to those of petroleum fuels, the oxygen must be eliminated. This reaction takes place at high temperature and pressure and is designated as catalytic hydrotreatment. This process is fairly similar to the conventional process employed in petroleum refineries. A typical catalytic hydrotreatment unit is a continuous flow hydroprocessing unit consisting of feed system, reactor unit, and product separation section, as presented in Figure 1.13 [12].

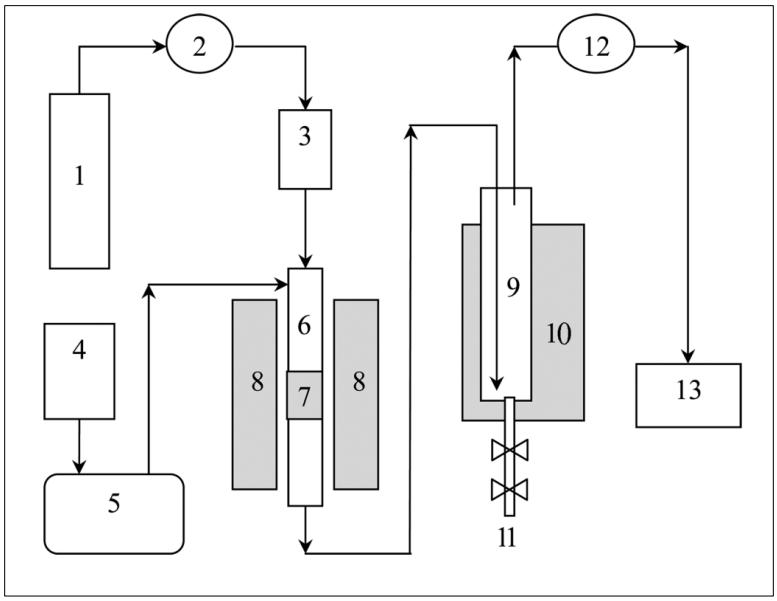

Figure 1.13. Simplified diagram of the green diesel hydroprocessing production unit. High pressure hydrogen cylinder (1), regulator (2), mass flow controller (MFC) (3), oil reservoir (4), high-pressure pump (5), continuous reactor (stainless steel) (6), catalyst bed (7), furnace (8), cold trap (9), ice water reservoir (10), liquid product outlet (11), back-pressure valve (12), and (13) online GC [12].

In the feed section, the oil is mixed with the high-pressure H_2 and is preheated prior to entering the reactor chamber. Check valves are used coupled with mass flow controllers to ensure safety in the entering stage of the reactant into the reactor. The hydrotreating reaction takes place on the catalytic bed at isothermal condition. The back pressure regulator is used to adjust the pressure of the whole setup. The liquid products were collected using a high-pressure low-temperature separator connected to a thermostatic cooling bath or an ice water reservoir.

1.5.1 Effect of process parameters

The selection of operating parameters has a significant influence on the hydrotreating reactions. The key operating parameters of hydrotreating in a continuous reactor include temperature, , liquid hourly space velocity (LHSV), pressure and H_2/oil ratio. Among these parameters, temperature and LHSV are studied in this work.

1.5.1.1 Temperature

Temperature significantly affects the product yields. Generally, oxygen removal is increased by increasing temperature. Srifa et al. performed the continuous hydrotreatment of palm oil over monometallic catalysts, and reported that there is a specified temperature (300ºC) under which, due to the presence of unreacted triglycerides and intermediate components, the liquid products have high viscosity [37]. Bezergianni et al. conducted the hydrotreatment of WCO oil in a small fixed-bed reactor pilot plant hydroprocessing unit. A commercial NiMo hydrotreating catalyst was used and pre-sulfided according to provider instruction. DMDS as a sulfiding agent was added to the feed to keep the catalyst in sulfided form. The effect of various process temperatures (330, 350, 370, 385 and 398ºC) was studied, while keeping other reaction parameters constant (P: 1200 psi, LHSV: 1 h^{-1}, H_2/oil: 4071 scfb). The WCOs which were plentifully used for frying were collected from households and restaurants, and filtered with the help of a simple mesh before being used as feed. It was shown that increasing the temperature led to an increase in hydrocracking reaction (see Figure 1.14, left up) [80].

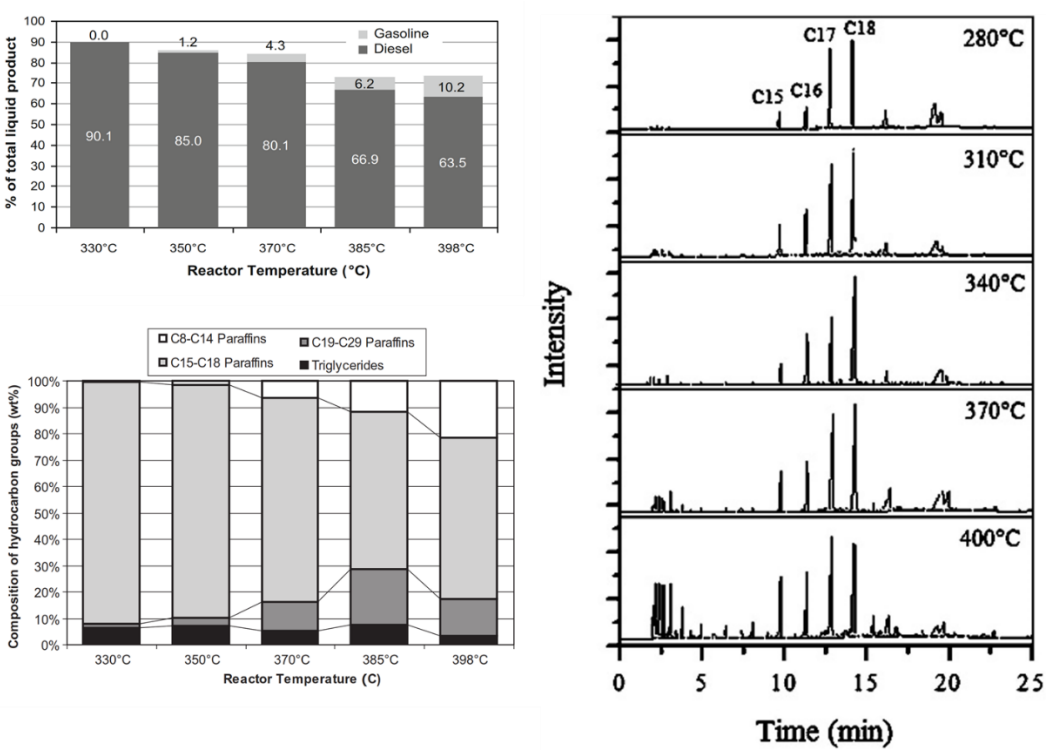

Figure 1.14. (Left up) diesel and gasoline yield (% wt.), (left bottom) hydrocarbons compositions (% wt.) at different temperatures. P:1200 psi, LHSV:1 h^{-1} and H_2/oil:4071 scfb [80], [81] and (right) gas chromatograms of the hydrotreated Jatropha oil products obtained at various reaction temperatures over the NiMoLa(5.0)/Al_2O_3 catalyst, reaction conditions; T: 280-400°C, P: 3.5 MPa, LHSV: 0.9 h^{-1} and H_2/oil:1000 mLmL^{-1} [82].

In another work done by the same group, using WCO as feed and the same reaction conditions, the hydrocarbon composition of the hydrotreated products were reported over the temperature range of 330 to 398ºC (see Figure 1.14 left bottom). As the hydrotreatment reaction temperature increased the triglyceride content in the product remained relatively constant. Diesel fraction (C15-C18 paraffin) is decreased while light (C8-C14 paraffin) and heavy (C19-C29 paraffin) fractions are increased. When the target product is green diesel, an increase in temperature results in a decrease in product yields which is due to the fact that increasing temperature leads to accelerated cracking. However, higher reaction temperature is more suitable when gasoline is the target product [81].

These results are in agreement with those reported by Liu et al. for the hydrotreatment of jatropha oil over NiMoLa/Al_2O_3 over the temperature range of 280 to 400ºC. The GC

chromatograms of final products obtained at different temperatures are presented in Figure 1.14 (right). It is clearly observed that the main components in the product were C15 to C18 straight chain hydrocarbons. Increasing temperature from 280 to 400ºC resulted in the formation of smaller chain molecules due to the enhanced cracking detected at lower retention time [82].

The usual temperature ranges for most of the catalytic hydrotreating and hydrocracking reactions is between 290-450°C. The temperature range depends on the type of catalyst used and the type of feedstock that is processed. In the first period of the catalyst life (industrial application), after loading of catalyst in the reactor, the temperature is normally maintained at low values while the catalyst is still highly active enough. However, as the time passes and deactivation and coking of catalyst take place, the temperature is gradually increased to overcome the loss of catalyst activity and to maintain high product yield and desirable quality. Šimáček et al. characterized the products of the hydrotreatment of rapeseed oil in a laboratory flow reactor over three commercial hydrotreating NiMo/alumina catalysts. The three catalysts had NiO and MoO_3 (% wt.) contents as follows: catalyst A has 3.8 and 17.3 (also contain P_2O_5), catalyst B: 2.6 and 15.7, and catalyst C: 2.6 and 8.8. The reaction was conducted over the temperature range of 260 to 340ºC, the pressure of 7 MPa, LHSV of 1 h^{-1} and H_2/oil ratio of 1000. As can be seen in Figure 1.15 (up), the selectivity of three catalysts changed with temperature, and as the temperature was increased the amounts of C17 and C18 were respectively increased and decreased. This trend shows that the DCO-DCO_2 pathways are favored at higher temperatures, whereas HDO pathway is restricted. As shown in Figure 1.15 (bottom), a parallel trend was observed for C15 and C16 presented as the ratio of n-C16/n-C15 [41]. Same trend was also observed in a work done by Krár et al. in the hydrotreating of sunflower oil using $CoMo/Al_2O_3$ catalyst (Figure 1.16). Increasing temperature from 300 to 380ºC favors the DCO-DCO_2 reaction pathways at various pressure [70].

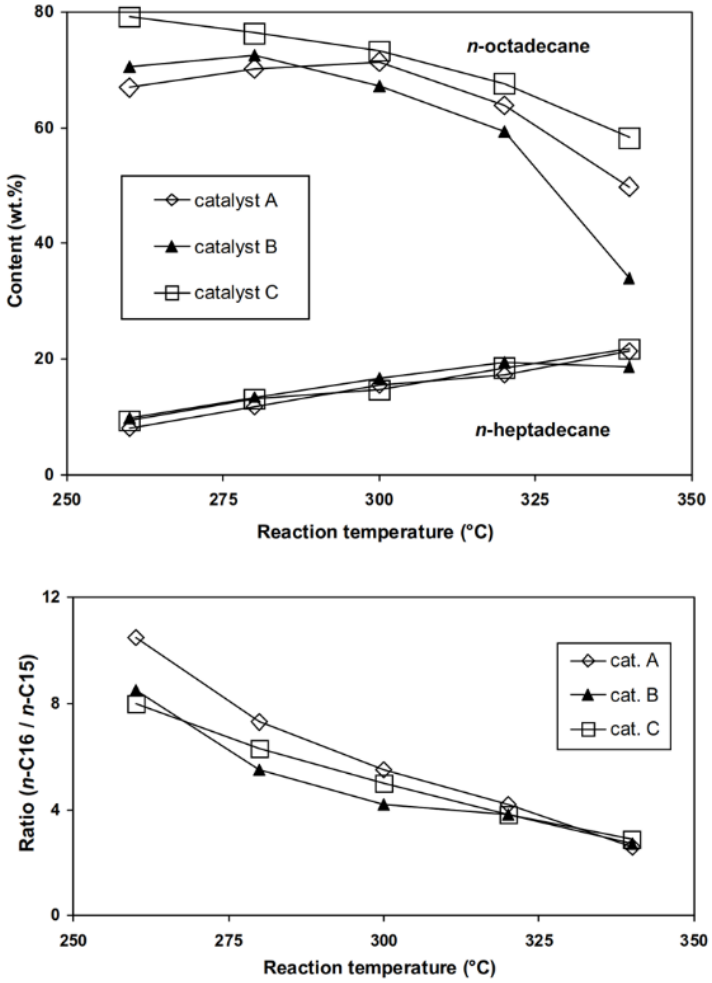

Figure 1.15. The (up) n-octadecane and n-heptadecane (% wt.) and (bottom) the n-C16/n-C17 ratio in the hydrotreated products. T:260-340°C, P:7 MPa, LHSV: 1 h^{-1}, and H_2/oil:1000 [41].

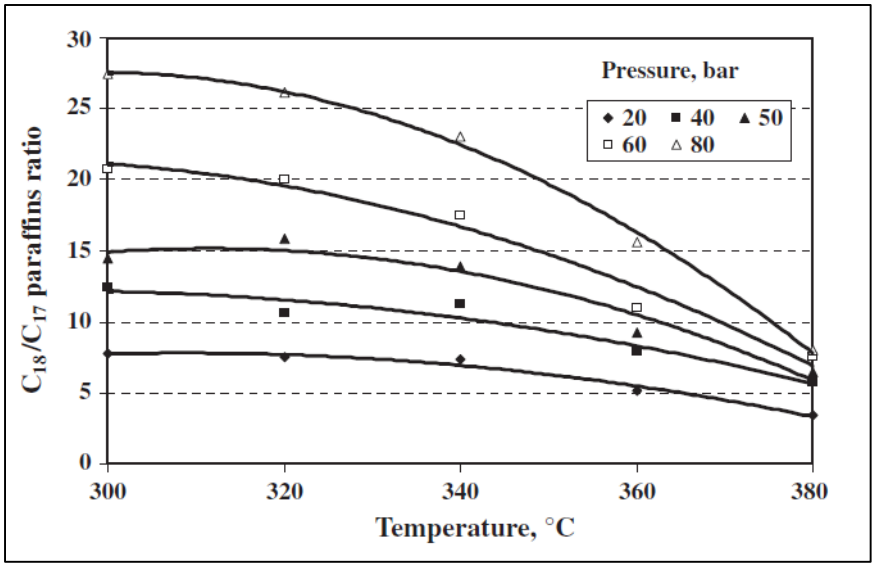

Figure 1.16. The ratio of C_{18}/C_{17}-paraffins at different pressure and temperature. LHSV: 1 h^{-1} and H_2/Oil: 600 m^3/m^3[70].

Orozco et al. proposed the hydrotreatment of castor and palm oil employing two coupled fixed-bed microreactors over commercial sulfided $NiMo/Al_2O_3$ and no catalyst characterization was reported. The pressure was kept constant at 3.5 MPa, while other reaction conditions varied as follows, temperature: 300 to 370ºC, residence time: 66-132 min and H_2/oil molar ratio: 35/1 to 105/1. It was reported that the temperature of 300ºC is not enough for the complete conversion of castor oil which is also reported elsewhere [37].

Furthermore, their best hydrotreated products were analyzed by FTIR (see Figure 1.17). As can be seen, the pressure of 3.5 MPa, H_2/oil molar ratio of 70/1, the temperature of 350ºC and the residence time of 66 min, resulted in the appearance of peaks at (2850-3000 cm^{-1}, 1740 cm^{-1} and 722 cm^{-1}) associated with saturated alkane bands (Figure 1.17 a and b). On the other hand, although sample c was produced at a residence time of 90 min, the lower hydrotreatment temperature (270ºC) led to the appearance of the peaks at 1719 cm^{-1} and 1748 cm^{-1} characteristic of the (acid and ester) carbonyl groups caused by incomplete conversion [83].

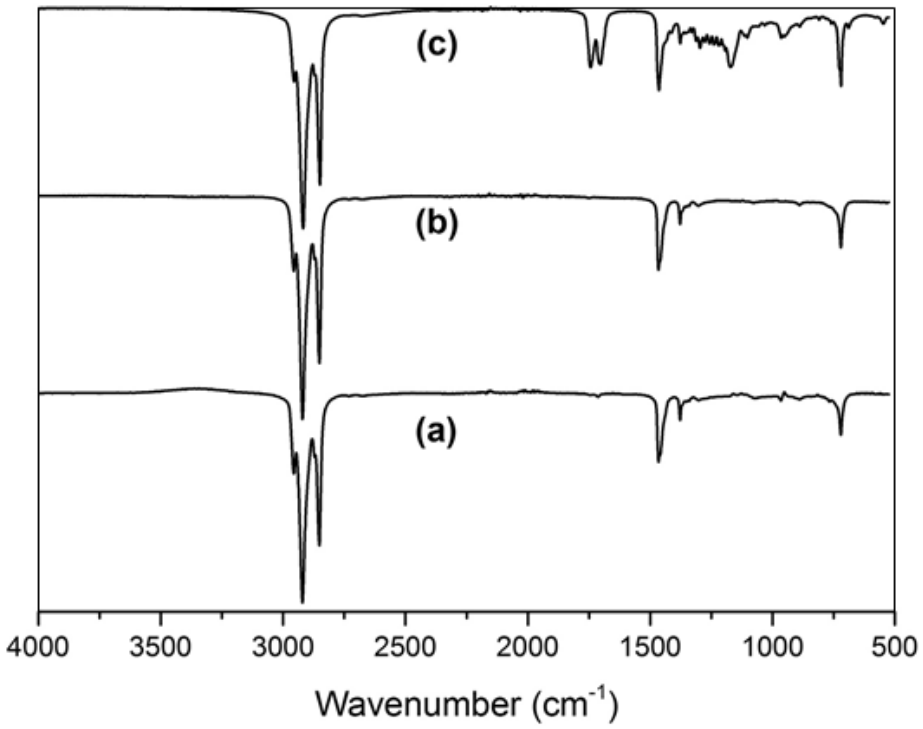

Figure 1.17. FTIR spectra of hydrotreated products at 3.5 MPa and H_2/oil molar ratio:70/1, (a) T: 350ºC, residence time: 66 min (castor oil), (b) T: 350ºC, residence time: 66 min (palm oil), (c) T: 270ºC, residence time: 90 min (castor oil) [83].

1.5.1.2 Liquid hourly space velocity

The liquid hourly space velocity (LHSV) is an essential operating parameter for regulating both catalyst lifetime and effectiveness since it defines the time that the reactants are in contact with the catalyst. LHSV is the ratio of the feed liquid flow rate to the catalyst volume which is expressed in h^{-1}. Kaewmeesri et al., performed the hydrotreatment of chicken fat using reduced Ni/Al_2O_3 catalyst in the LHSV range of 0.5 to 2 h^{-1}, while keeping other reaction conditions constant (T:330ºC, P:50 bar and H_2/oil: 1000 cm^3cm^{-3}). It was reported that an increase in the LHSV results in a reduction of the green diesel yield. On the other hand, very low LHSV can also enhance the cracking reaction leading to the formation of light products [15].

Anand and Sinha reported a gradual increase in unconverted triglycerides by increasing the LHSV from 1 to 8 h^{-1}. The formation of waxy product is also reported at LHSV higher than

10 h^{-1} and temperature lower than 300ºC that is in agreement with previous literature [37], [83]. When LHSV increases, the available time for the feed to be in contact with the catalyst decreases, and thus, the conversion reduces [32], [84]. Thus, finding an acceptable value for LHSV is an important issue. It is noticeable that maintaining large values of LHSV enforces a high rate degradation of the catalyst in industrial units, and thus, it is kept as high as is practically possible.

1.5.1.3 Pressure

Hydrotreating process and catalyst activity are also influenced by hydrogen partial pressure. High hydrogen partial pressures result in high operational costs (compatible infrastructure and feed cost). Thus, hydrogen partial pressure should be optimized according to the catalyst activity. High hydrogen pressure also helps to prevent the catalyst deactivation by removing water from the catalyst. A higher hydrogen pressure facilitates the HDO pathway which consumes more H_2 than DCO-DCO_2 (see equations 1.1-1.3). Moreover, highly unsaturated feedstocks show higher hydrogen consumption compared to saturated ones.

Liu et al. investigated the effect of H_2 pressure on the hydrotreatment of jatropha oil over NiMo/SiO_2-Al_2O_3 catalyst. As presented in Figure 1.18, the yield of gas product (C_3-C_4), increased with increasing H_2 pressure from 0.5 to 3 MPa and was kept almost constant when the H_2 pressure was above 3 MPa. In the liquid hydrocarbon products, a significant increase in yield was observed by increasing H_2 pressure from 0.5 to 3 MPa, followed by a slight increase from 3 to 8 MPa. It is well known that acid number indicates the content of carboxylic acid in triglycerides. As can be observed in Figure 1.18, acid value (based on mg KOH/g) of bio hydrogenated diesel sharply diminished with increasing H_2 pressure and could not be identified when H_2 pressure was above 4 MPa indicating a high conversion of carboxylic acids (triglycerides) to paraffin [12].

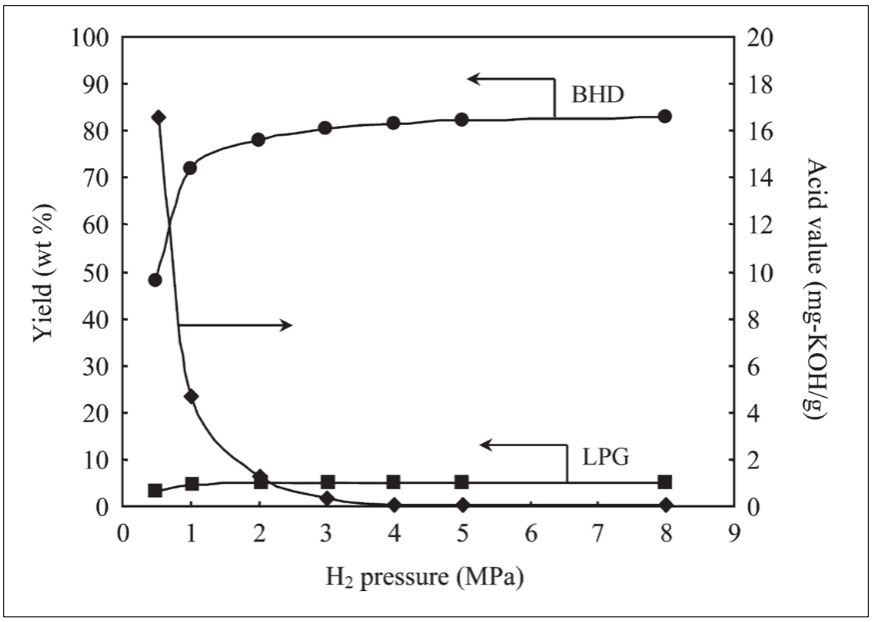

Figure 1.18. Effect of H_2 pressure in the hydrotreatment of jatropha oil over $NiMo/SiO_2$-Al_2O_3; Yield of hydrogenated biodiesel (liquid hydrocarbons) (●) and its acid value (♦); yield of liquefied petroleum gas ($C_3 + C_4$) (■) [12].

1.5.1.4 H_2/oil ratio

Another effective parameter for hydrotreating processes is the ratio of hydrogen gas to liquid oil feed flow rates which also has an impact on the efficiencies of hydrogenation and cracking reactions. Increasing the ratio of H_2/oil leads to an enhancement in heteroatom removal and saturation reaction. Although, increasing H_2/oil ratio to some extent results in a higher liquid product yield, a change in the final composition of obtained hydrocarbons was also reported. Krár et al. also reported the decline of the DCO-DCO_2 reactions with increasing the H_2/sunflower oil volume ratio, at various temperatures of 340-380ºC and constant pressure of 80 bar shown in Figure 1.19 [70].

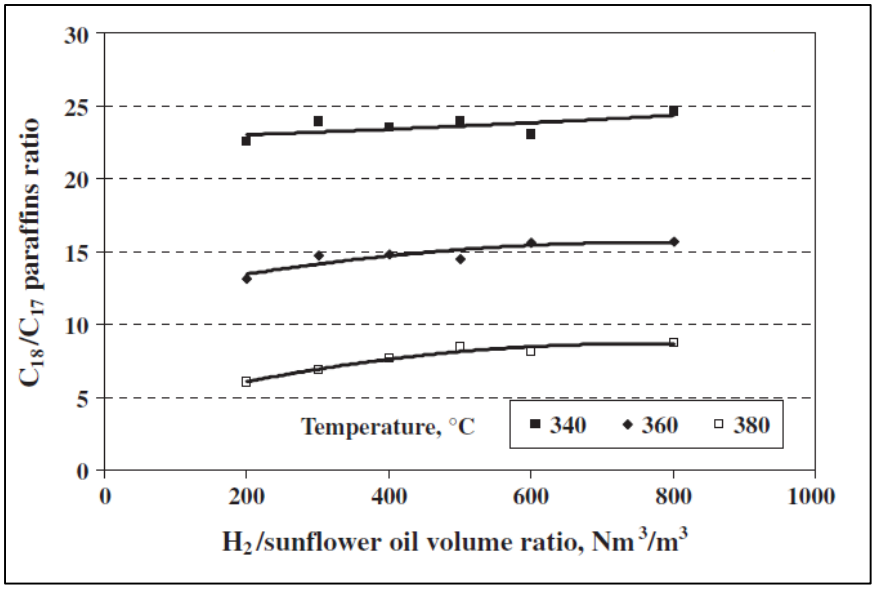

Figure 1.19. C18/C17 ratios at different H_2/sunflower oil volume ratios and temperatures, P: 80 bar, LHSV: 1 h^{-1} [70].

1.6 Thesis objectives and organization

The main objective of this research is the development of catalysts for the production of green diesel from vegetable oils. For this purpose, canola oil as triglyceride source should undergo hydrotreating in a continuous down-flow fixed-bed homemade reactor in the presence of heterogeneous catalysts to produce green diesel. The product should be a mixture of hydrocarbons with chain lengths same as conventional diesel and which could be directly used as a fuel. To do so, the work will be divided into three sub-objectives that can be described as:

- One-pot synthesis of improved γ-alumina with controllable textural properties (specific surface area, pore volume, pore diameter and crystalline phase) to be used as catalyst support regarding large size reactant such as triglycerides.

- Utilization of the synthesized γ-alumina in the preparation of bimetallic NiMo/γ-alumina and CoMo/γ-alumina via co-incipient wetness impregnation technique. Application of these catalysts in the sulfided form, in a continuous down-flow reactor, to produce green diesel from canola oil; and study the process parameter

(temperature, LHSV) effect on the triglyceride conversion and chain length distribution of the final product.

- Synthesis of Ni/γ-alumina catalysts via two different methods of sol-gel (one-step) and wet impregnation (two-step) using synthesized mesostructured γ-alumina support. Evaluation of their structural differences due to various preparation procedures. Comparison of the catalytic activity of the two kinds of catalysts for the hydrotreatment of canola oil producing green diesel according to conversion and chain length distribution over time on stream.

This dissertation consists of five main chapters:

In the first chapter, a brief introduction to the production of green diesel from triglycerides using heterogeneous catalysts was presented. According to the scope of this work, a literature review on key aspects of the green diesel production such as the feedstock, methods to produce fuel from oils, hydrotreatment mechanism and process and different used catalysts was explained.

The second chapter is devoted to the synthesis of mesostructured γ-aluminas via one-pot sol-gel method with the aim to be used as a catalyst support for the hydrotreatment of triglycerides. The effect of calcination temperature and polymeric template concentration on the final properties of the mesoporous γ-alumina were investigated.

Chapter three studies the preparation of nanoporous bimetallic NiMo/γ-alumina and CoMo/γ-alumina catalysts using mesoporous γ-alumina as a catalyst support, via incipient wetness co-impregnation. The hydrotreatment of vegetable oil was performed in a continuous down-flow fixed-bed reactor varying the LHSV and temperature as process parameters. The final green diesel product consisted mainly of n-alkanes, mostly C15-C18. Slightly better catalytic activity was found over Ni-based catalyst compared to Co-based catalyst. The optimum temperature and LHSV were found to be 325ºC and 1 h^{-1}, respectively.

Chapter four introduces the environmentally friendly reduced Ni/γ-alumina catalysts for the hydrotreatment of vegetable oil in a fixed-bed down-flow homemade reactor. Two methods were used for the catalyst preparation: sol-gel (one-step) and impregnation (two-step). The

previously developed mesostructured γ-alumina was used as catalyst support for the impregnated catalyst while for the sol-gel derived catalysts the nickel was incorporated in the mesostructured framework. The collected products mainly consist of C15 to C18 normal hydrocarbons. The sol-gel catalysts showed higher time on stream due to the higher stability compared to the impregnated catalyst.

Finally, the fifth chapter presents a general conclusion recalling briefly the main results of this study and presents some recommendations for future work.

Chapter 2

Synthesis of ordered mesoporous γ-alumina – Effects of calcination conditions and polymeric template concentration

Arsia Afshar Taromi and Serge Kaliaguine, Microporous and Mesoporous Materials, Volume 248, August 2017, Pages 179-191.

Résumé

Dans ce travail, une alumine mésoporeuse a été synthétisée en utilisant un polymère tensioactif par voie sol-gel et accompagné d'un auto-assemblage induit par évaporation (EISA) en présence d'un isopropoxyde d'aluminium ($Al(O\text{-}i\text{-}Pr)_3$) utilisé comme source d'aluminium. Parmi les paramètres expérimentaux affectant les propriétés de l'alumine synthétisée, l'effet de la température de calcination et la teneur en copolymère triblock (Pluronic P123) dans le gel ont été étudiés. Les effets de la température de calcination (allant de 700°C à 1050°C) sur les paramètres tels que la surface spécifique, le volume des pores, la distribution de la taille des pores, la transformation de phase et la taille des cristaux ont été investigués. De plus, l'influence du rapport massique de $P123/Al(O\text{-}i\text{-}Pr)_3$ entre 0.49-1.96 sur la texture de l'alumine synthétisée a aussi été étudiée. Pour cela, l'alumine mésoporeuse synthétisée a été caractérisée en utilisant l'analyse des isothermes d'adsorption-désorption de N_2, TGA/DTG et DSC/DTA. L'identification des phases et mesure de la taille des domaines cristallins ont été effectuées à l'aide de la DRX. La morphologie des échantillons calcinés a été analysée par SEM et TEM. Les observations TEM et les mesures SAXS ont révélé un réseau de pores mésostructurés dans les échantillons. Les distributions du diamètre des pores ont aussi été estimées par une analyse d'image numérique des images TEM. Les distributions des longueurs des pores ont également été estimées à l'aide de la barre d'échelle des images TEM et se sont avérées avoir des moyennes d'environ 800 nm. Les distributions de taille des pores de volume calculées (PSD) se sont révélées concorder raisonnablement avec les PSD obtenues à partir de l'analyse NLDFT des isothermes d'adsorption-désorption d'azote. Les alumines-γ synthétisées présentaient une stabilité thermique jusqu'à 950°C. À des températures plus élevées la mésostructure s'est effondrée avec formation de la phase α. Les échantillons obtenus avec $P123/Al(O\text{-}i\text{-}Pr)_3$ = 0.98 et 1.47, calcinés à 700°C avec un temps de plateau de 3 h ont présenté une surface spécifique de 259 m^2/g et 238 m^2/g respectivement.

Abstract

Mesoporous alumina was one-pot synthesized via polymeric surfactant template assisted sol-gel and Evaporation-Induced Self-Assembly (EISA) using aluminum isopropoxide (Al(O-i-Pr)$_3$) as aluminum source. Among several experimental parameters affecting the properties of the synthesized aluminas, the effect of calcination temperature and the triblock copolymer template (Pluronic P123) content in the gel were studied. The effects of calcination temperature in the range of 700°C-1050°C, on such parameters as surface area, pore volume, pore size distribution, phase transformation, and crystal size were experimentally investigated. The influence of P123/Al(O-i-Pr)$_3$ mass ratio in the range of 0.49-1.96 on the textural properties of the synthesized alumina was studied. The synthesized mesoporous alumina was characterized using N_2 adsorption-desorption analysis, TGA/DTG and DSC/DTA. The phase identification and crystal domain size were determined using XRD. The morphology of the calcined samples was analyzed using SEM and TEM. The TEM observations and SAXS measurements revealed the mesostructured pore lattice of the samples. The pore diameter distributions were estimated by numerical image analysis of TEM images. The pore lengths distributions were also estimated using the scale bar of TEM images and found to be averaged around 800 nm. The calculated volume pore size distributions (PSD) were found in reasonable agreement with the PSDs obtained from NLDFT analysis of nitrogen adsorption-desorption isotherms. The synthesized γ-aluminas exhibited thermal stability up to 950°C. At higher temperatures, the α-phase was formed, and the mesostructure collapsed. Samples obtained with P123/Al(O-i-Pr)$_3$ = 0.98 and 1.47, calcined at 700°C with 3 h soaking time exhibited a surface area of 259 m^2/g and 238 m^2/g respectively.

2.1 Introduction

Mesoporous solid materials are used in a wide range of industrial applications owing to their chemical, mechanical and thermal properties. Among various mesoporous substances, high surface area oxides, such as aluminum (III) oxides are used as catalyst supports or even directly as catalysts in various large-scale processes [85], [86]. They are used as a support for noble metal catalysts (such as Pt and Pd) and common sulfided hydrotreating bimetallic catalysts such as Ni-Mo, Co-Mo, and Ni-W [14], [31], [52], [70]. While used as catalyst support, their catalytic performance strongly depends on such properties as specific surface area, pore size, pore volume and crystalline phase that could be adjusted by changing the preparation conditions [87]. Mesoporous aluminas are most commonly produced using soft/hard template assisted through sol-gel self-assembly together with Evaporation-Induced Self-Assembly (EISA) process. In EISA, the initial solvent contains the alumina precursor and surfactant dissolved in water or ethanol. Further solvent evaporation leads to the formation of an organized templated mesoporous inorganic substance. The properties of the final mesoporous inorganic substance are significantly affected by initial surfactant/precursor ratio [88]–[90].

To obtain organized mesoporous γ-alumina, different templates including hard templates such as activated carbon [91], polymeric microspheres [90], [92]; and soft templates (surfactants) [93], could be employed. Using activated carbon as a template results in the formation of micropores, which limits the usefulness of the resulting catalyst support. The presence of impurities in the template can also affect the composition of the templated solid. In the case of using polymeric microspheres such as polystyrene or poly(methyl methacrylate) to control the textural pattern of alumina, the template should be first synthesized via polymerization with a narrow particle size distribution, to let the formation of a unimodal narrow pore size distribution after template removal. This multistep process is time-consuming, while by using a structure-directing agent (ionic or non-ionic) as a template, the ordered porosity can be reached in one-step. Polymeric surfactant template assisted sol-gel method along with the EISA process is a promising one-pot method among those methods due to its reproducibility and simplicity, controlling aspects, and lack of impurities. Various parameters such as calcination temperature and surfactant content can be controlled to obtain

different textural properties. On the morphological point of view, alumina exists as amorphous or different oxide and oxyhydroxide crystalline phases. Crystalline alumina has proper acid-base properties compared to amorphous alumina, which are key features in many catalytic applications. The crystalline structures which mainly consist of γ, δ, θ and α (corundum) phases, differ in properties. All these structures can be reached by irreversible transformation under heat treatment of well-crystallized hydroxides and aluminum salts or via colloidal gel precipitation. They are all metastable except for α-Al_2O_3, which is the most thermodynamically stable compound of oxygen and aluminum and the final high-temperature product of the thermal treatment [94], [95].

To optimize the specific surface area, pore width, and pore volume while reaching γ-alumina phase, the effects of polymeric surfactant concentration in the gel and the calcination temperature have been studied. Sun et al. [58] reported the effect of calcination temperature on pore size and crystalline structure of mesoporous alumina. Suzuki and Yamauchi [59] used a mixture of surfactant and polystyrene nanospheres as a template for synthesis of hierarchical porous γ-alumina. Increasing calcination temperature from 500°C to 900°C reduced the surface area while increasing the pore diameter. Wu et al. [56], [57] demonstrated the effect of P123 concentration on mesostructured alumina characteristics. Their material did not result in a wormhole-like structure. In the work of Grant et al. [96], the Pluronic F127 triblock copolymer was used as template to synthesize ordered mesoporous alumina. In another study, Bleta et al. [97], reported the effect of calcination temperature on mesostructured boehmite synthesized by the sol-gel method. It was observed that at a high temperature of around 1000°C, the prepared materials remained thermally stable. Li et al. [98], used Pluronic P123 and fatty alcohol polyoxyethylene ether non-ionic surfactant to synthesize mesoporous alumina. Their results showed that increasing the surfactant content results in larger pores. The higher calcination temperature of about 900°C, resulted in a surface area reduction of around 70% compared to 400°C.

The structural dependency of mesoporous alumina to polymeric template content and calcination temperature and in particular the effects of these parameters on the properties of the final porous structure were investigated. In the present study mesostructured γ-Al_2O_3 was synthesized with the objective of optimizing the pore structure features for the application of

these materials as supports for hydrodeoxygenation (HDO) of vegetable oil triglycerides. Therefore, the structure directing agent template assisted sol-gel method was investigated in order to control the pore lattice properties, to avoid mass transfer limitations which should be expected with such large molecule reactant.

2.2 Experimental

2.2.1 Material and alumina preparation

According to a typical mesoporous alumina synthesis via the template-assisted sol-gel method, first a specified amount of poly (ethylene oxide)$_{20}$-poly(propylene oxide)$_{70}$-poly(ethylene oxide)$_{20}$ triblock copolymer (Pluronic P123) (Mav = 5800, BASF Co.), used as a soft template was dissolved in 60 mL of anhydrous ethanol (Commercial Alcohols, CAS no.67-17-5) using a magnetic stirrer at room temperature. A very small amount of dissolved water such as the one in the added HNO_3 solution is sufficient to control the hydrolysis of Al(O-i-Pr)$_3$. To adjust the pH of the solution, about 4.2 mL of HNO_3 69% wt. (Sigma-Aldrich, CAS no. 7697-37-2) was added to the solution. Subsequently, 30 mmol of Al(O-i-Pr)$_3$ (Sigma-Aldrich, CAS no. 555-31-7) as the aluminum source was added to the above mentioned solution. The molar composition of the reaction mixture Al(O-i-Pr)$_3$/P123/Et-OH/HNO_3 was 0.03/ (0.0005, 0.0010, 0.0015 and 0.0020)/1/0.1. All chemicals were used as received. The solutions were continuously stirred (600 rpm) at room temperature for 24 h. Then, they were poured in Petri dishes and maintained at 60°C for eight days inside a drying oven. In this step, ethanol evaporated during the EISA process along with the formation of a light yellow to yellow solid depending on the template concentration. Different samples were calcined by increasing the temperature from room temperature to the desired temperature (700°C to 1050°C) in air atmosphere. A heating rate of 1°C min^{-1} was used to ensure uniform heat transfer and prevent any collapse of the alumina structure caused by quick dehydration or fast grain growth. The samples were left at the desired temperature for 3 h, to completely burn off the template along with the formation of the possible alumina phase (γ, α). The reported results are the average of at least three measurements. The synthesized aluminas were identified as X-Y, where X and Y represent the mass ratio of P123/Al(O-i-Pr)$_3$ and the final calcination temperature (°C), respectively. The molar ratios P123/Al(O-i-Pr)$_3$ indicated above (0.0166, 0.0333, 0.05, and 0.0666) correspond to X, the mass ratios of P123/Al(O-i-

$Pr)_3$ of (0.49, 0.98, 1.47, and 1.96). For instance, SA-0-Y indicates a sample without P123. The notation SA-X-P will designate dried but non-calcined precursors.

2.2.2 Characterization

2.2.2.1 Nitrogen adsorption-desorption analysis

This test was carried out at -196°C using a Quantachrome Nova 2000 instrument. All calculations were done using the Autosorb-1 software, (Quantachrome Instruments). Before the analysis, a known mass of sample around 400-500 mg was degassed at 200°C under vacuum for 5 h until a residual pressure of 10^{-6} mbar was reached. The specific surface area (S_{BET}) of the samples was established via standard Brunauer-Emmett-Teller (BET) equation over the relative pressure (P/P_0) range of 0.05-0.2 (linear part). The adsorption branch of the isotherm was used to determine the pore size distribution curve (PSD) using Barrett-Joyner-Halenda (BJH) calculation. The total pore volume (V_t) was obtained from the volume of adsorbed nitrogen at the relative pressure of $P/P_0 = 0.99$. The specific surface area, total pore volume and pore width (S_{DFT}, V_{DFT}, and W_{DFT}, respectively) were also calculated using non-local density functional theory (NLDFT) method. The pore size distributions were determined by applying the kernel of NLDFT using the equilibrium isotherm of N_2 at -196°C on silica, assuming all pores have a cylindrical shape.

2.2.2.2 Thermogravimetric analysis (TGA/DTG)

The data were recorded on a TA Instruments Q5000 equipped with an autosampler by using platinum (50 μL) TGA pans using the high-resolution mode. Synthetic air (25 $mLmin^{-1}$ STP) was used as the carrier gas with a heating rate of 5°C/min from 50°C to 900°C for 15-30 mg of uncalcined (non-dried) samples.TGA curves were acquired by plotting the relative weight (%) of the samples versus temperature.

2.2.2.3 Differential scanning calorimetry (DSC/DTA)

Differential scanning calorimetry (DSC) measurements were performed by using a Netzsch STA 449C thermogravimetric analyzer. The curves were recorded by loading about 20 mg of uncalcined sample in an alumina crucible pan. The experiments were executed at a temperature scanning rate of 10°C/min using air gas purge flow of 20 $mLmin^{-1}$, from 50 to 1200°C. All reported data were blank-corrected.

2.2.2.4 X-ray diffraction (XRD)

Wide-angle X-ray scattering (WAXS) diagrams were recorded by using a Siemens D5000 diffractometer with Cu Kα monochromatized radiation source (wavelength of 0.154059 nm), at room temperature, operating at a fixed power source of 40kV and 30 mA. Counts were collected every 0.02° (2θ), ranging from 10 to 90°, at a scan speed of 1°/min. Prior to analysis, the samples were gently ground to form a fine powder (< 100 µm). Phase recognition was acquired by comparing the experimental diffraction patterns to Joint Committee on Powder Diffraction Standards (JCPDS) database. The average crystallite sizes of samples were roughly estimated after Warren's correction for instrumental broadening using Scherrer's formula: $D = K\lambda/\beta Cos\theta$ where $K \approx 0.9$ (Scherrer constant), $\lambda = 1.54059$ Å, and θ is the Bragg's diffraction angle position. β is the effective linewidth of the X-ray reflection, obtained using $\beta^2 = B^2 - b^2$ formula, where B is the (FWHM) and b is the instrumental broadening defined by the FWHM of the X-ray reflection of quartz (both in radians), containing particles larger than 150 nm, at $2\theta \approx 27°$ [99]. Small-angle X-ray scattering (SAXS) was measured using a Nanostar U Small-angle X-ray scattering system (Bruker, Germany) with Cu Kα radiation (40 kV, 35 mA) in the range of 1-10°. The d-spacing values were calculated using the formula $d = 2\pi/q$.

2.2.2.5 Scanning electron microscopy (SEM)

The morphology, texture and elemental composition of the synthesized aluminas were determined and recorded using scanning electron microscope (SEM) JEOL JSM-840A equipped with an EDX spectrometer (functioning at an accelerating voltage of 15 kV at high vacuum 10^{-6} Torr employing secondary electron mode). Prior to the observation, powdered samples were dispersed on a 300 mesh copper grid followed by an amorphous carbon film coating. Then, the samples were sputter coated in a vacuum chamber (100 mTorr) with Pd/Au to form an electrically conductive surface. The EDX signals were acquired by focusing a high energy electron beam on the desired surfaces and collecting the spectra within 60 s of acquisition time using Spirit™ Bruker AXS Microanalysis software. Eventually, the EDX spectra were accumulated from random area of samples using a single point quantitative analysis. Besides, SEM images were acquired using Orion™ software at different

magnifications under operational conditions of 15 kV accelerating voltage and a current beam of 60 μA at a working distance of 20 mm.

2.2.2.6 Transmittance electron microscopy (TEM)

The morphology of the samples was also analyzed using a JEM-1230 (JEOL) transmission electron microscope equipped with a lanthanum hexaboride (LaB6) filament thermionic emission source. The electron beam acceleration voltage was adjusted to 80 kV, using a Gatan Ultrascan 1000XP camera. Specimens were gently ground and dispersed in methanol and underwent moderate sonication in a water bath for 10 min. A drop of the obtained solution (≈ 5 μL) was pipetted uniformly on a Formvar film coated nickel grid (200 mesh). Prior to analysis, the grid was dried in air at room temperature.

2.2.2.7 Image analysis and Morphological Operations (MO)

The pore diameter distributions were estimated using the Morphological Operations (MO) image analysis using MATLAB software based on five representative TEM images (≥ 200 pores) of the same sample. The pore lengths distributions were determined by measuring all pore lengths in one single slab by using TEM images scale bar. At least five micrographs were taken each picture comprising a single slab.

2.3 Results and Discussion

2.3.1 Nitrogen adsorption-desorption analysis

2.3.1.1 Effect of calcination temperature

To find the appropriate calcination temperature for a high surface area mesophase γ-alumina, calcinations were performed from 700°C to 1050°C under air atmosphere. Some samples (the ones prepared without P123 and those calcined at 1050°C) showed a non-porous structure and very low surface area. For this reason, their nitrogen adsorption-desorption isotherms and related pore size distribution are not reported here. The nitrogen adsorption-desorption isotherm and related pore size distribution curves of samples SA-0.98-Y calcined from 700°C to 950°C with a calcination time of 3 h are presented in Figures 2.1 and 2.2, respectively. All samples exhibit the classical shape of type IV adsorption-desorption isotherms with hysteresis loops of H2 type slightly shifting to H3 type (characteristic of

materials with channel-like or ink-bottle pore connectivity with relatively narrow pore size distribution indicating pores with cylindrical morphology with numerous interconnections between the pores) [100]. By increasing the calcination temperature (Figure 2.1), the isotherms and hysteresis loops keep the same shape, but change in size. Increasing the calcination temperature from 700°C to 950°C results in a lower capillary condensation value resulting in smaller hysteresis loops. Comparison of the different calcination temperatures for samples SA-0.98-Y shows that the large N_2 uptake at a low relative pressure of sample SA-0.98-700 is shifted to higher relative pressure by increasing the calcination temperature (Figure 2.1). This reflects the destruction of small pores and the formation of pores with larger diameters [57], [59]. For all samples, the increase in calcination temperature results in larger pore diameters, but smaller surface area and pore volume (Table 2.1).

As shown in Figure 2.2 none of the samples has significant micropores. By increasing the temperature, the PSD curves start at higher pore diameters. Lower temperatures lead to sharper pore size distribution. Broadening of pore size distribution curves with increasing the temperature from 700°C to 950°C can be related to the loss of water from the alumina structure, possibly with structure rearrangement to form the γ-phase, which is also confirmed by DSC/DTA (Figure 2.8) [97]. This phase formation leads to pore wall shrinkage and some porous structure collapse, which makes the PSD curve shift to a higher pore size at higher calcination temperatures.

Sample SA-0.98-950 shows a noticeable reduction in surface area and pore volume compared to SA-0.98-700. The remaining relatively high surface area (Table 2.1) revealed that the as-made mesoporous alumina samples are still thermally stable at this high calcination temperature. This thermal stability is of great importance when alumina is used as catalyst support in high-temperature processes. By increasing the calcination temperature from 700°C to 950°C, the surface area, and the pore volume decreased from 259 m^2/g to 113 m^2/g, and 0.506 cm^3/g to 0.254 cm^3/g respectively; and the average pore diameter increased from 7.8 nm to 9 nm. For this temperature range, the N_2 adsorption capacity varied from approximately 350 cm^3/g to 150 cm^3/g (STP). At higher temperatures densification, shrinkage, and finally, sintering could lead to the formation of larger pores [97], [101]. It is therefore suggested that to obtain a mesoporous alumina in γ-phase while keeping the high

surface area, a calcination temperature of 700°C is appropriate. The textural properties of samples with different P123/Al(O-i-Pr)$_3$ mass ratios, i.e., X = 0.49, 0.98, 1.47 and 1.96, calcined at various temperatures are summarized in Table 2.1.

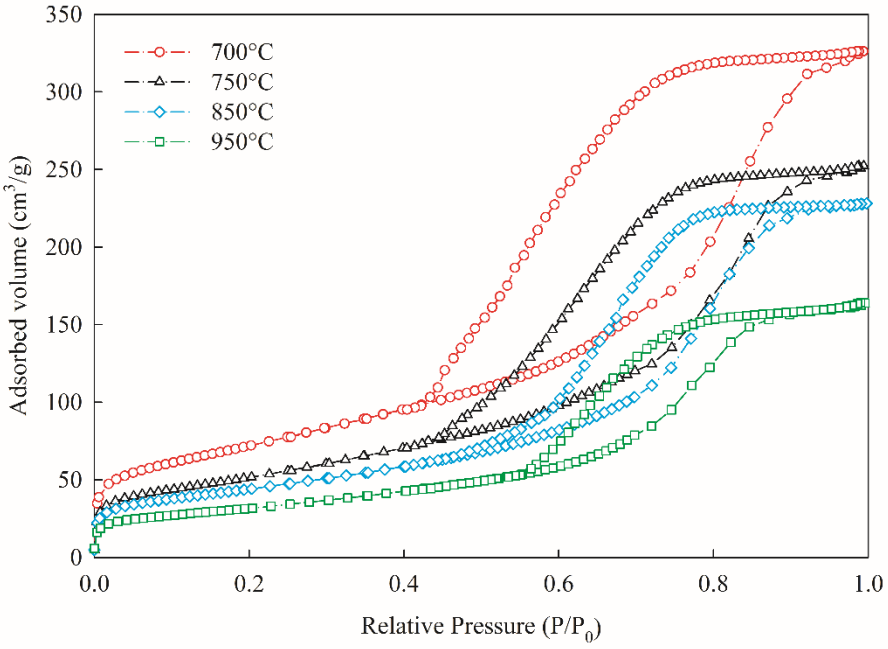

Figure 2.1. Nitrogen adsorption-desorption isotherms of SA-0.98-Y calcined at different. Temperatures.

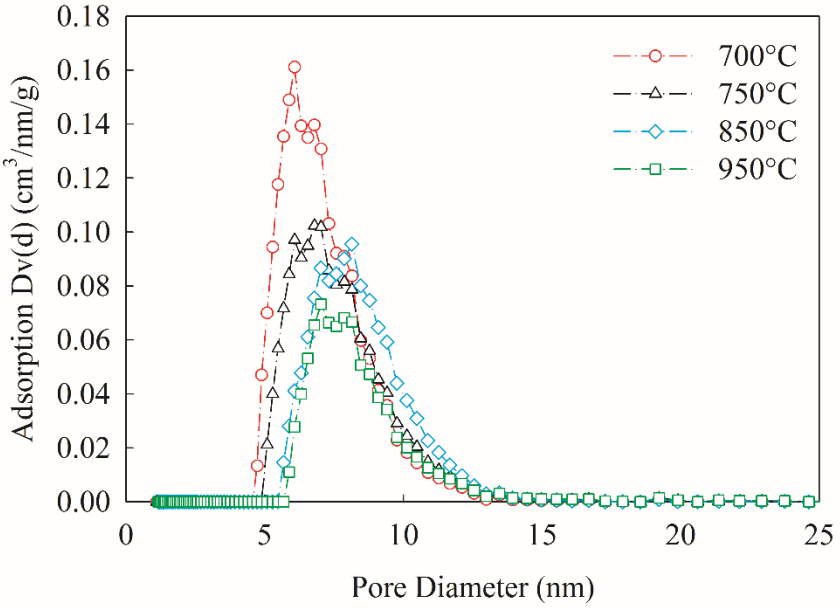

Figure 2.2. NLDFT pore size distribution of SA-0.98-Y calcined at different temperatures.

Table 2.1. Adsorption properties of calcined mesoporous alumina at different temperatures for 6 h.

Samples, SA-0.98-Y at Y:	S_{BET} (m^2/g)	S_{DFT} (m^2/g)	V_t (cm^3/g)	V_{DFT} (cm^3/g)	W_{BJH} (nm)	W_{DFT} (nm)
700	259	283	0.506	0.488	7.8	6.1
750	186	203	0.391	0.376	8.4	6.8
850	158	168	0.354	0.343	9.0	8.2
SA-X-700 at X:						
0.49	174	172	0.247	0.236	5.7	4.9
1.47	238	246	0.634	0.612	10.6	8.2
1.96	93	81	0.195	0.182	8.4	5.7
SA-X-950 at X:						
0.49	121	130	0.229	0.220	7.6	6.1
0.98	113	118	0.254	0.243	9.0	7.0
1.47	99	114	0.497	0.485	20.1	13.9
1.96	40	36	0.155	0.147	15.4	7.0

Specific surface area (S_{BET}) is calculated from adsorption data in the relative pressure range of 0.05 to 0.2. Single point pore volume (V_t) calculated from the adsorption isotherm at the relative pressure of 0.99. Barrett-Joyner-Halenda (BJH) method is used to calculate pore width at the maximum of the PSD using adsorption branch. The kernel of NLDFT equilibrium capillary condensation isotherms of N_2 at 77K on silica is used to calculate S_{DFT} (specific surface area), V_{DFT} (total pore volume) and W_{DFT} (pore diameter)

2.3.1.2 Effect of template concentration

The Nitrogen adsorption-desorption isotherms and corresponding PSD curves of samples prepared with different polymer template contents, calcined at the two temperatures of 700°C and 950°C with a 3 h soaking time are presented in Figures 2.3 to 2.5. As shown in Figure 2.3, samples SA-0.49-700 and SA-0.49-950 show type IV isotherms with H2 and H2 mixed slightly with H3 hysteresis respectively, indicating the presence of mesoporous structure with numerous channel-like or ink-bottle interconnections between the pores [102]. The capillary condensation step is steeper and starts at lower P/P_0 for sample SA-0.49-700, showing the presence of a more uniform structure and a smaller pore diameter. As the pores are not too large, they can be completely filled before reaching the relative pressure of P/P_0 =1 making a plateau section in the isotherms of both samples at high relative pressure. This plateau section begins at lower relative pressure for sample SA-0.49-700, suggesting the smaller pores with a slightly higher total pore volume of this sample compared to sample SA-0.49-950, are filled completely at lower relative pressure (Table 2.1). As can be seen in Figure 2.3, the pore size distribution of sample SA-0.49-700 is quite narrower compared to sample SA-0.49-950, which is in accordance with TEM images (Figure 2.14).

As seen in Figure 2.4, sample SA-1.47-Y shows the type IV isotherm with a combination of H3 and slight H2 types; this type of hysteresis loop indicates the presence of slit-shape pores in the macro range [103]. This sample shows a high pore volume at high calcination temperatures. The shift of capillary condensation step to higher relative pressure is observed while increasing the calcination temperature. Sample SA-1.47-700 shows a rather narrow pore size distribution, while sample SA-1.47-950 shows a broad pore size distribution with a very large pore size (up to 21 nm). Such materials with large pores and high pore volume are good candidates for catalyst support; they will facilitate the movement of large reactant molecules inside the pores and enhance active metal loading [48].

Increasing the P123/$Al(O\text{-}i\text{-}Pr)_3$ ratio to 1.96 results in a remarkable reduction in the adsorbed volume (Figure 2.5). Both samples present type IV isotherms; sample SA-1.96-700 shows the H4 type hysteresis loop which is typical for materials with narrow slit-like pores, and sample SA-1.96-950 shows the H3 type without any limiting adsorption at high relative

pressure which is characteristic of materials formed from aggregates where the porosity is not defined [104].

The pore size distribution of SA-1.96-Y is highly affected by increasing temperature (Figure 2.5). It seems that the porous structure of SA-1.96-950 is not well-formed. Increasing the template content to a high concentration in the case of P123/Al(O-i-Pr)$_3$ = 1.96 during synthesis enhances the viscosity of the solution which can prohibit the EISA process during aging [57].

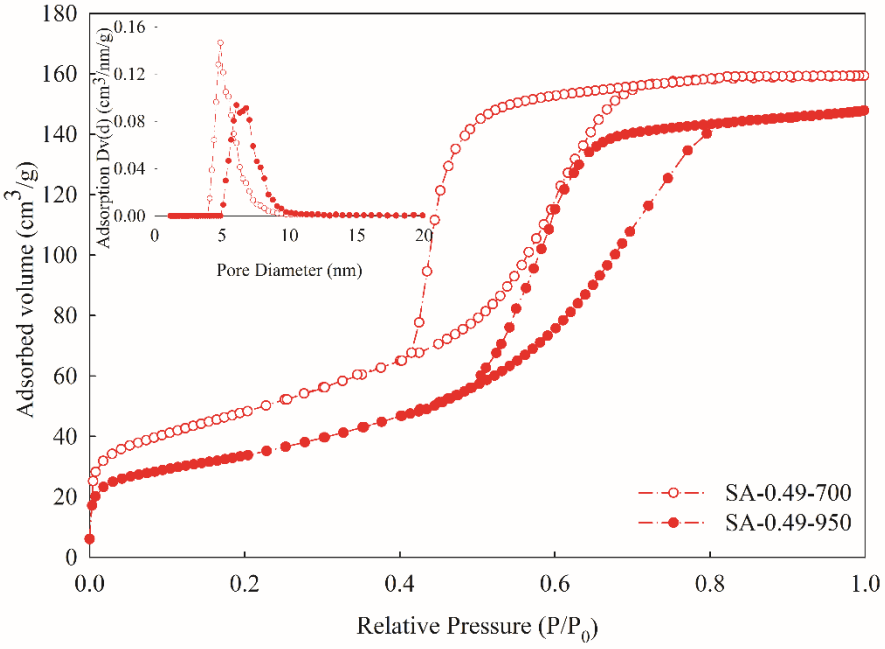

Figure 2.3. Nitrogen adsorption-desorption isotherms and the corresponding PSDs for samples SA-0.49-Y calcined at 700°C and 950°C.

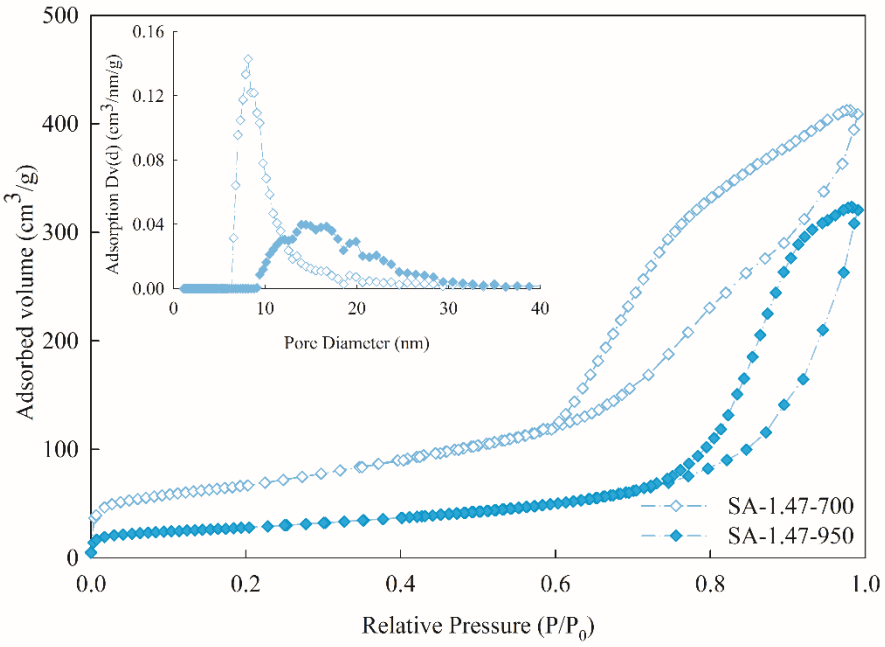

Figure 2.4. Nitrogen adsorption-desorption isotherms and the corresponding PSDs for samples SA-1.47-Y calcined at 700°C and 950°C.

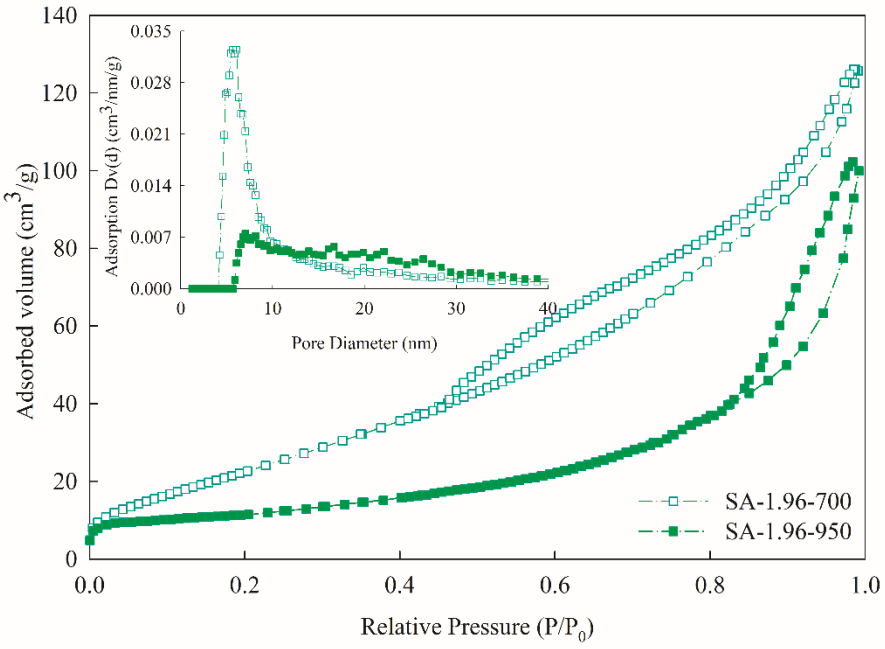

Figure 2.5. Nitrogen adsorption-desorption isotherms and the corresponding PSDs for samples SA-1.96-Y calcined at 700°C and 950°C.

For all samples, an increase in calcination temperature results in a lower volume adsorption and broader pore size distribution curves. The maximum of this broadening effect is seen in sample SA-1.96-950. Both samples SA-0.49-950 and SA-0.98-950 also show the broadening effect but still keep their narrow pore size distribution curve. Sample SA-0.49-700 with a narrow pore size distribution has relatively small surface area and pore volume which are limiting factors for its usage as catalyst supports. Among all samples, samples SA-0.98-700 and SA-1.47-700 show relatively high surface area and pore volume. Both of them show relatively narrow pore size distribution. The pore diameter of sample SA-0.98-700 is smaller than that of sample SA-1.47-700. They both also have a relatively high pore volume (Table 2.1).

2.3.2 Thermogravimetric analysis (TGA/DTG)

Thermogravimetric analysis of the dried as-made alumina precursors (SA-0.98-P, SA-0-P) was performed to study the characteristic soft template decomposition during calcination. The TGA/DTG curves of P123, SA-0.98-P, and SA-0-P samples determined under air atmosphere are depicted in Figures 2.6 and 2.7, respectively.

TGA/DTG curve of pure P123 (25 mg sample in a platinum pan) shows a sharp weight loss peak at ≈ 210°C associated with the polymeric template thermal decomposition (Figure 2.6). Comparing this peak with its corresponding peak in the TGA/DTG curve of sample SA-0.98-P at 192°C (Figure 2.7) points out the effects of $Al(O\text{-}i\text{-}Pr)_3$ presence which causes a slight reduction in the P123 degradation temperature.

As seen in Figure 2.7, the addition of P123 template has a noticeable effect on the thermal process that can be viewed in the TGA/DTG curve of the SA-0.98-P sample. At a temperature below 160°C (Section 1), both samples show a weight loss associated with the removal of physisorbed/chemisorbed water. The differences between these two weight losses (27.8%: SA-0-P, 18.2%: SA-0.98-P) can likely be due to the adsorbed polymer on the sample surface which restricts water removal and reduces water absorbance capability in the presence of P123. The weight loss peak at ≈ 208°C starting at ≈ 170°C for sample SA-0-P is attributed to the removal of chemically adsorbed water and alcohol molecules (gel network water) and nitrate decomposition also described elsewhere [105], [106].

A very sharp weight loss in the range of 160°C to 260°C (section 2) in TGA/DTG curve of sample SA-0.98-P, which consists of two peaks with maximums at ≈ 192°C and ≈ 217°C, can be related to the decomposition of P123. This sample contains residual HNO_3, which produces NO_x in-situ through oxidation reaction. This can catalyze the P123 decomposition (the first sharp peak).

As Bleta et al. [97] reported and is observed in Figure 2.7 (sample SA-0.98-P), when all NO_x are consumed, oxygen diffusion becomes the limiting factor, reducing decay rate. This phenomenon is apparent in the second part of the peak. The DTG curve of both samples shows a weight loss starting at 260°C with a maximum value at 300°C ending at around 400°C (section 3). This weight loss is related to the loss of water associated with the

condensation and removal of residual hydroxyl groups still present in the structure. Above this temperature, a stable alumina phase is formed, as indicated by the stable weight plateau section [57].

It was reported that the conversion of Boehmite (AlOOH) to γ-Al_2O_3 via dehydroxylation reaction happens at a temperature above 300°C with a theoretical weight loss of 15% [29]. This is in good agreement with the value obtained for as made SA-0.98-P sample, i.e. 13% at 260-450°C. The weight losses of pure P123, SA-0-P and SA-0.98-P samples at different temperature zones are shown in Table 2.2.

Table 2.2. TG weight loss (%) during calcination process.

Sample	$\Delta W_{50\text{-}160°C}$	$\Delta W_{160\text{-}260°C}$	$\Delta W_{260\text{-}400°C}$	$\Delta W_{50\text{-}900°C}$	Residual W
Pure P123	0.9	20.7	0.9	22.4	0
SA-0-P	27.8	24.7	11.7	66.3	33.7
SA-0.98-P	18.2	38.7	12.9	71.0	29

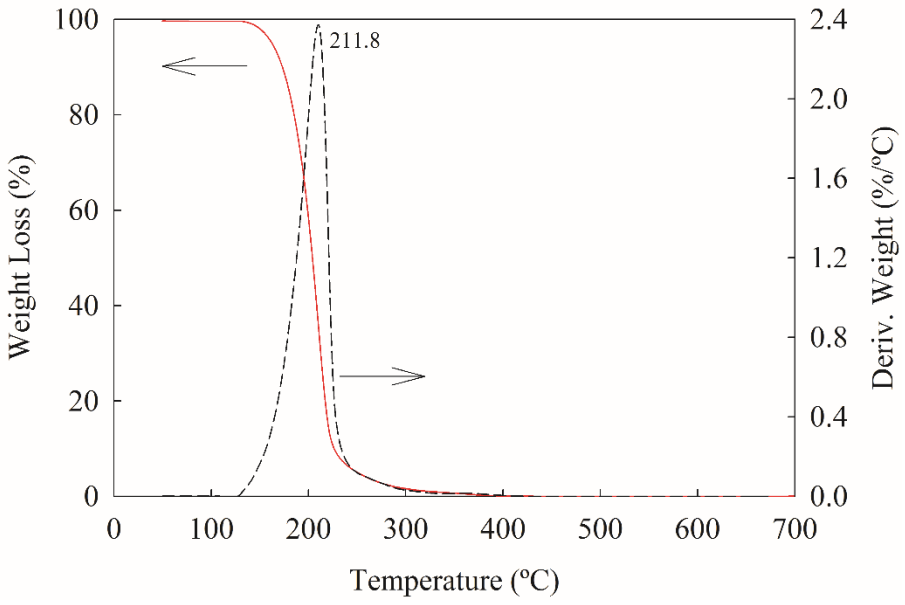

Figure 2.6. TGA/DTG curve of Pluronic P123 under air.

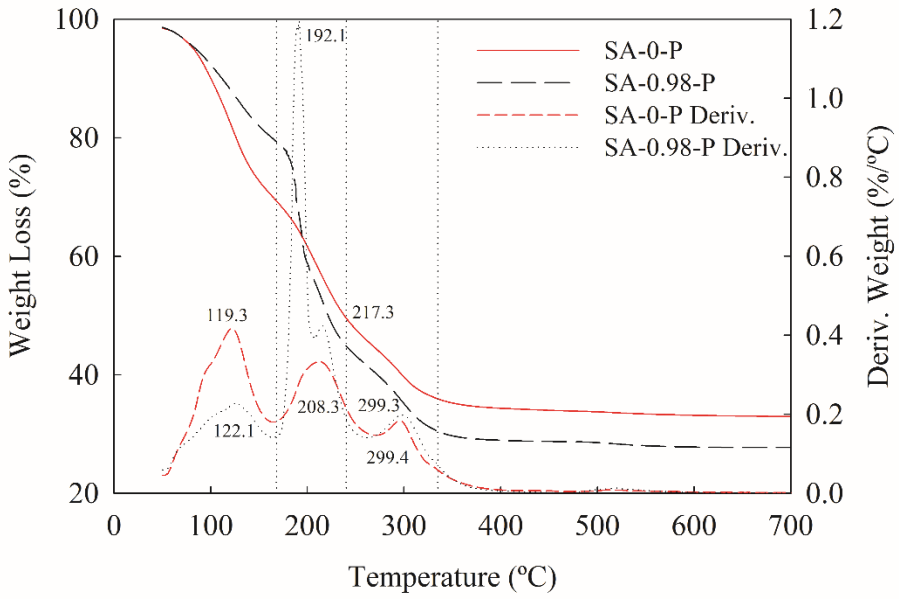

Figure 2.7. TGA/DTG curves of samples SA-0-P and SA-0.98-P.

Template removal and the ceramization process are critical steps in the formation of mesostructured alumina by hindering the formation of the defects and structural collapse that have probably the same importance as the synthesis process itself. It is worth stating that to completely eliminate the polymeric template, hence resulting in the expected porosity, and obtaining a white-snow colored alumina, a minimum temperature of 600°C and a residence time of 3 h are needed with the used experimental calcination set up. The EDX spectra of samples SA-0-650, SA-0-700 and SA-0.98-700 revealed that alumina is the only remaining component after calcination above 650°C (inset Figure 2.12 a, b and c). If the applied temperature is less than 450°C, a dark gray product is formed as a result of incomplete combustion of the template. Moreover, a slow heating rate and sufficient airflow are required for complete removal of the template.

2.3.3 Differential scanning calorimetry (DSC/DTA)

DSC was used to investigate the alumina structure phase formation temperature. Figure 2.8 shows the DSC/DTA results of samples SA-0-P and SA-0.98-P. Sample SA-0-P shows an endothermic peak which started below 160°C with a maximum at around 192°C, due to the

removal of the remaining physisorbed and chemisorbed water. In the same temperature range beginning at about 160°C, sample SA-0.98-P shows a sharp exothermic peak with a maximum at 212°C as a result of the polymeric template combustion along with the removal of the remaining physisorbed and chemisorbed water. At higher temperatures, both samples show an analogous trend. The exothermic peak starting above 300°C, with a maximum at 312°C, indicates the formation of structured alumina [94]. Moreover, the exothermic peaks centered at 872°C and 852°C observed for SA-0-P and SA-0.98-P, can be attributed to the transformation of γ-phase to θ-phase and α-phase. This temperature difference can be related to the defects in alumina caused by the polymeric template. These defects could lower the activation energy of the phase formation [107], [108]. This transition from γ to α phase should be initiated at 1000°C according to XRD analysis (Figure 2.9).

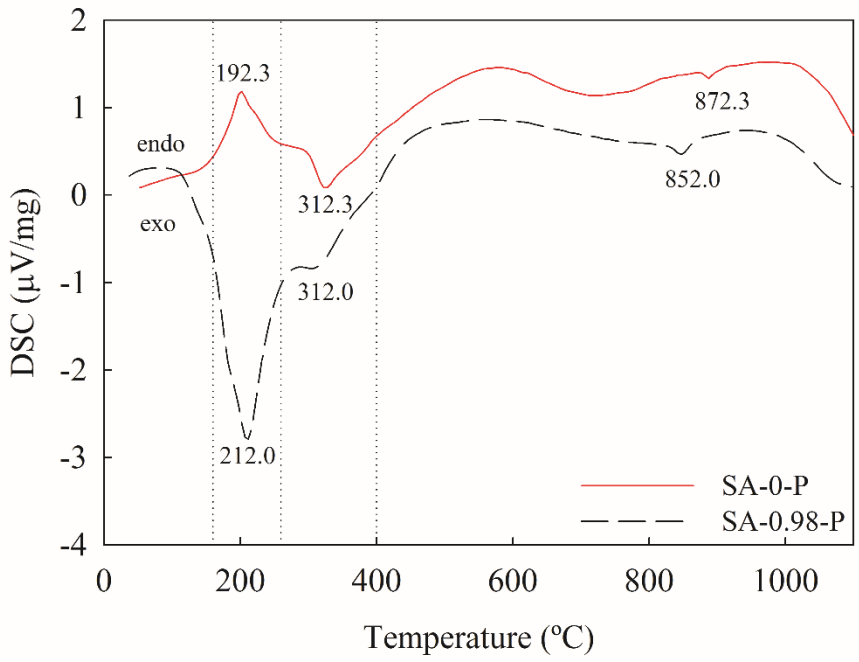

Figure 2.8. DSC/DTA curves of the non-calcined SA-0-P and SA-0.98-P samples.

2.3.4 X-ray diffraction (XRD)

The XRD patterns of calcined SA-0.98-Y powder heated from 650°C to 1050°C are shown in Figure 2.9. In this calcination temperature range, no differences were observed in the XRD patterns of samples synthesized with or without P123, suggesting that the crystalline structure depends essentially on calcination temperature. This observation is in line with those in reference [109].

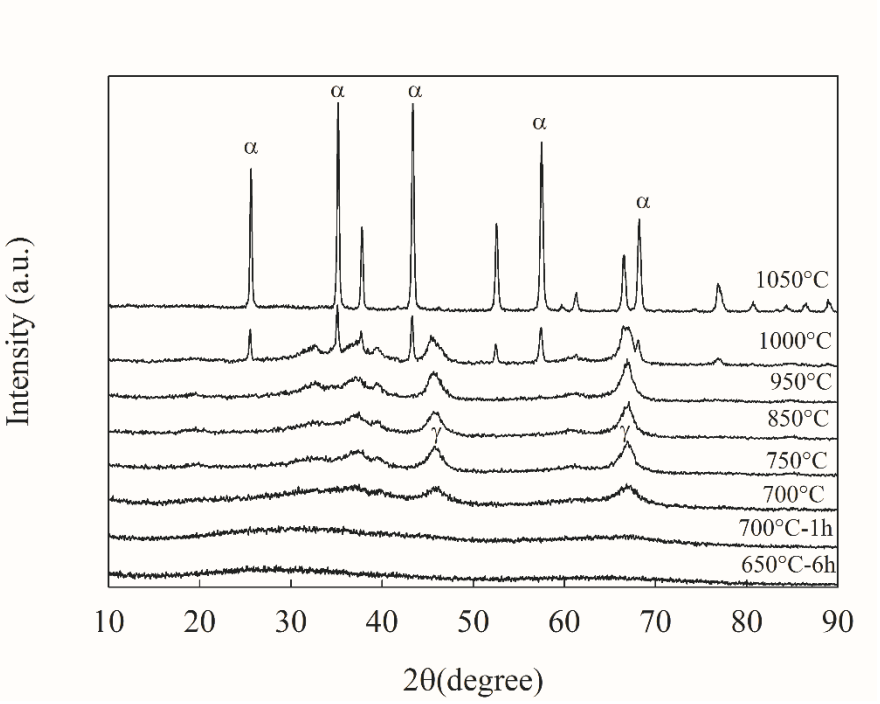

Figure 2.9. X-ray diffraction patterns of SA-0.98-P calcined at different temperatures (the calcination time is 3 h unless noted otherwise).

To determine the appropriate required soaking time for crystal formation, soaking times of 1, 3 and 6 h, and 1 and 3 h were chosen for samples SA-0.98-650 and SA-0.98-700, respectively. For sample SA-0.98-650 a residence time of up to 6 h results in the formation of an amorphous structure and no crystalline diffraction peak is detected in the XRD patterns; this temperature is not high enough for the formation of γ-Al_2O_3. Sample SA-0.98-700 with 1 h residence time also results in the formation of amorphous structure. Increasing the residence time to 3 h for this sample results in the formation of the diffraction peaks which

are indexed to γ-Al_2O_3 phase with cubic structure (JCPDS card 10-0425). The crystallization of alumina takes place between 1 and 3 h at 700°C. The broad peaks reflect the nano-size crystalline grain of the γ-Al_2O_3 samples. The two peaks with a diffraction intensity at 2θ = 46 and 67° are the principal peaks of gamma-phased alumina [110], [111]. Then, a single calcination temperature step with soaking time of 3 h was selected for all other samples. The dependency of calcination time on crystal formation is also reported in a study done by Boissiere et al. [104]. Heating from 700°C to 950°C revealed that the gamma phase remains intact. By increasing the temperature in this range, the crystallinity of samples increased resulting in the formation of sharper diffraction peaks. As can be seen in Figure 2.10, the crystal size grows from 7.6 nm to 9.9 nm (as determined using Scherrer equation) by increasing the temperature from 700°C to 950°C.

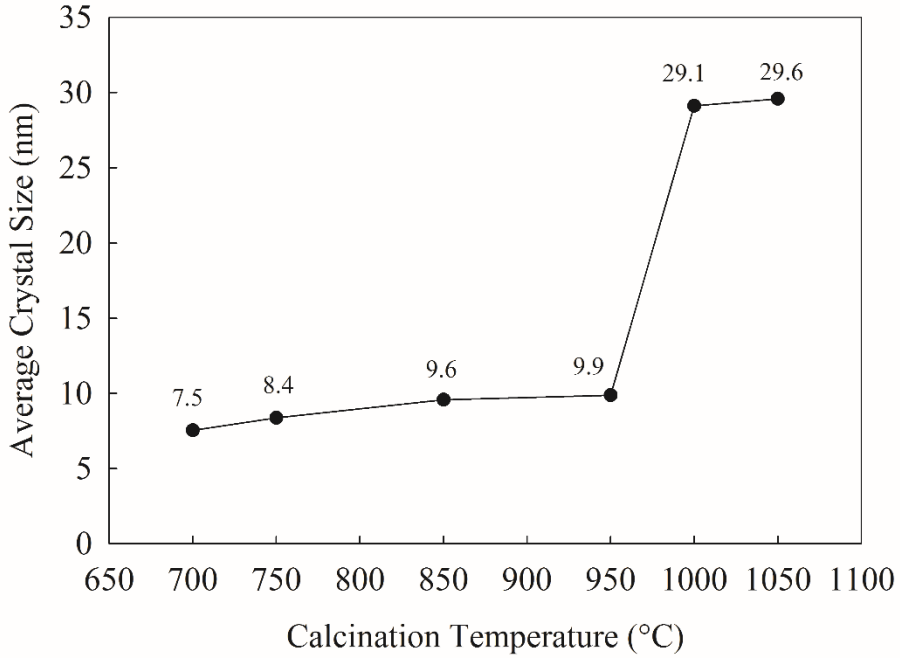

Figure 2.10. The average crystal size of samples SA-0.98-Y calcined at different temperatures under air atmosphere and calcination time of 3 h.

At 1000°C in addition to the diffraction peaks of γ-Al_2O_3, the diffraction peaks indexed to α-Al_2O_3 phase (JCPDS card, 11-0661) also appear which indicates the formation of a

polymorph phase showing the transition from gamma phase to alpha phase. The main peaks with diffraction intensities at 2θ = 26, 32, 43, 57 and 68° are the principal peaks for alpha-phased alumina [110]. No other metastable phase is seen between these two phases, although in DSC/DTA analysis this phase transition appeared at a lower temperature, (see Figure 2.8). Above 1000°C, at 1050°C as a result of the full transformation of γ-Al_2O_3 to α-Al_2O_3 only the sharp diffraction peaks of the highest stable α-Al_2O_3 phase is present. These sharp, well-defined peaks show the formation of relatively large crystal grains along with the massive reduction in surface area (ex: 5 to 6 m^2/g for SA-0.98-1050) as a result of the porous structure collapse. A steep increase in crystal size from 9.9 nm to 29.1 nm (Figure 2.10) is observed for the sample calcined at 950°C to 1000°C, followed by a slight crystal growth to 29.6 nm for the sample calcined at 1050°C. This steep increase could be the result of the rearrangement of the structure of γ-Al_2O_3 by destroying the spinel lattice vacancies to form the highly stable and crystalline α-Al_2O_3. This trend is also reported by other researchers [94], [112], [113].These results show that the γ-Al_2O_3 samples prepared via EISA method are thermally stable up to 950°C, which is in a favorable agreement with the above mentioned BET results and TEM image observations reported below.

The small angle powder X-ray scattering diffraction patterns for selected calcined samples are presented in Figure 2.11. The absence of any peak in the SAXS diffraction of sample SA-0-700 indicates the absence of any mesostructure; also confirmed with TEM images (Figure 2.12e). When the P123 content is low (SA-0.49-700) a sharp diffraction peak at around 2θ = 0.64° (d_{100} = 13.6 nm) and a weak peak at around 2θ = 1.2° are observed which can be attributed to diffraction peaks of (100) and (110), respectively. As seen in Figure 2.11, the peak in the pattern of SA-0.98-700 was shifted to higher 2θ = 0.68° (d_{100} = 12.8 nm) along with a lower d-spacing, showing that the pore diameters of SA-0.98-700 are increased compared to SA-0.49-700 [93]. However, SA-1.47-700 shows a peak around 2θ = 1°, which in agreement with TEM images (see Figure 2.16) is ascribed to a 2D hexagonal *P6mm* symmetry [114]. Increasing the calcination temperature results in major collapse and sintering of the porous structure, and no ordering in SAXS diffraction of sample SA-1.47-1050 is seen. This is in good agreement with the result obtained from XRD and TEM images (see Figures 2.9 and 2.17e, f). By further increasing of gel P123 content, the framework shrinkage is enhanced, and the overall mesostructure is slightly deteriorated. The presence

of second order peak at 2θ = 1.36° shows the high degree of ordering of the structure, which is also detectable in SAXS diffraction of sample SA-1.96-700 [115][104].

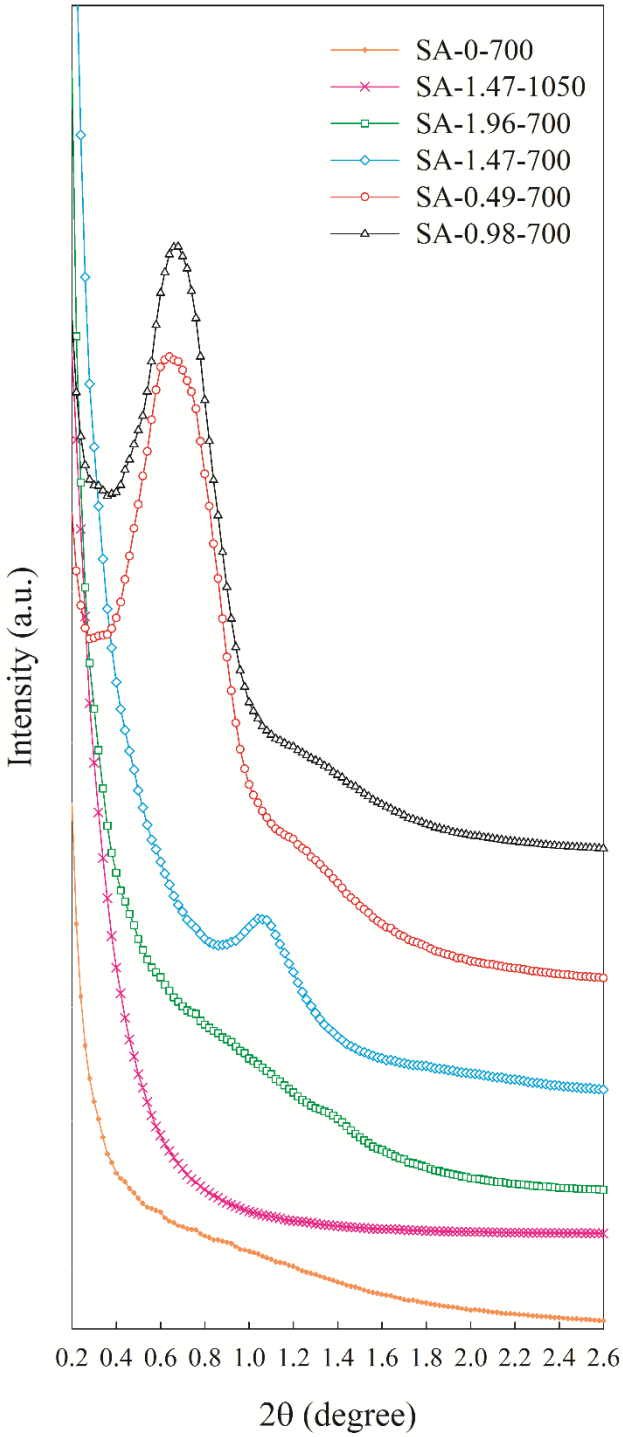

Figure 2.11. SAXS diffraction patterns of selected alumina samples.

2.3.5 Electron microscopy (SEM, TEM and image analysis)

SEM and TEM images of SA-0-650, SA-0-700, and SA-0.98-700 samples are illustrated in Figure 2.12. As can be seen in Figure 2.12a, the formed porous structure of SA-0-650 shows two types of macropores: some large pores formed inside the matrix walls and smaller pores included in them. At higher temperatures, the smaller pores inside the matrix walls disappear while the large pores become well-formed smaller as can be seen in Figure 2.12b for sample SA-0-700. This could probably be because of further alumina structure condensation which happens at this elevated temperature. Moreover, the addition of polymeric template, even at low contents, leads to the formation of smooth surface with some well-formed cracks and the disappearance of macropores (see Figure 2.12c). This phenomenon is also observed at higher template concentrations (not presented). TEM micrographs of the prepared alumina, SA-0-650, and SA-0-700 samples (Figure 2.12d and 2.12e), prepared in the absence of P123 show a very smooth surface. They mainly consist of dense adjacent large particles with no regular shape. These observations are consistent with SAXS analysis results (Figure 2.11). The TEM image of sample SA-0.98-700 (Figure 2.12f) reveals the formation of a mesoporous wormhole-like textural structure which occurred while polymeric template was employed. This wormhole-like structure is formed due to the long-chain molecules and the high degree of hydrogen bonding of the P123 template [108]. Energy-dispersive X-ray (EDX) spectroscopy measurements ((inset Figure 2.12 a, b and c) confirmed the presence of carbon-free alumina.

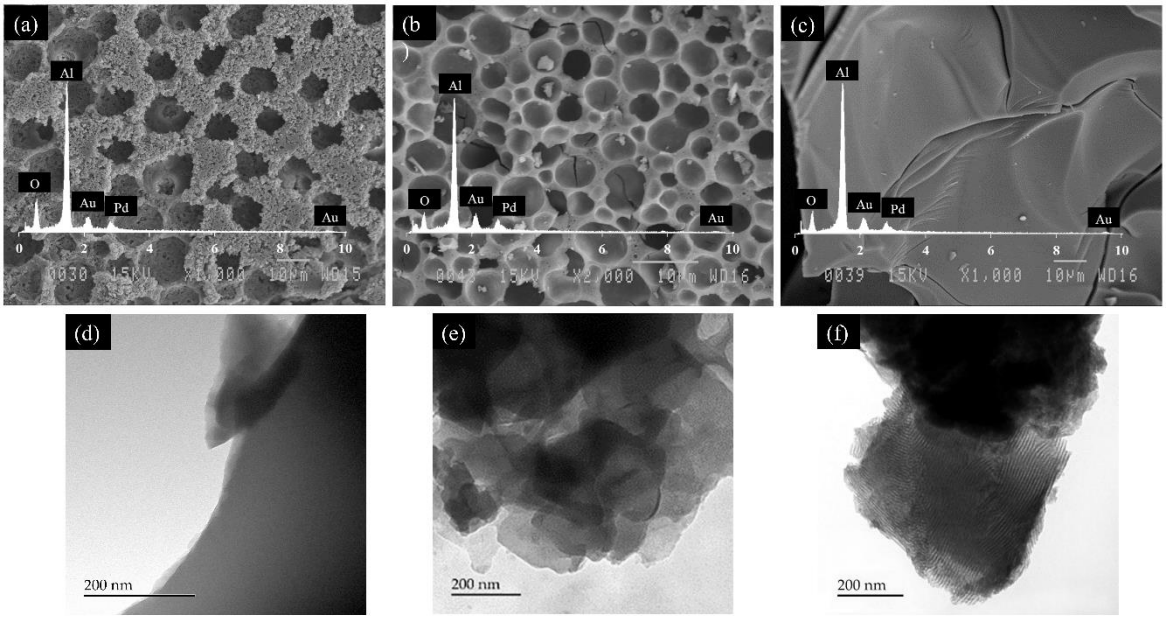

Figure 2.12. SEM, EDX (inset) and the corresponding TEM images of (a, d) SA-0-650, (b, e) SA-0-700, (c, f) SA-0.98-700.

2.3.5.1 Computational (TEM) image analysis

The pore diameter estimation from TEM images was performed applying image analysis approaches. Image analysis widely uses the morphological operation (MO) by applying different kernel operators in the function which leads to erosion and dilation within the components of the image. It also helps the extraction of objects and spatial enhancements. An image can be defined as a function of given amplitude (intensity or color) in the continuous or discrete coordination corresponding to the pixel points of the images. In general, MO is making use of dilation and erosion functions which are utilized in a different hierarchy. Dilation is to enlarge each pixel of the intensity of the image source, and erosion provides an opposite effect on the image. Brightness and kernel pixels are the parameters of MO functions which can influence the outcome of the operation. As above mentioned, dilation and erosion combinations are introduced to make other MO functions, for instance, the opening operation can be made by erosion followed by dilation, or on the contrary, closing includes a dilation followed by erosion. The function of morphology strives to extract or enhance the structural or contextual information in the analysis of the image. Here this information includes information on porosity in TEM images as targeted object in the image.

The intensity or targeted pixel size of the pores in the image object varies by applying such techniques. It provides adjustment or improves the beneficial information (targeted pores) by applying a Laplacian filter (Canny edge detection approach is also applied). The second partial derivation of the image for both coordinates of x and y gives a significant filter to find edges. Using the zero crossing for finding the edge location, Laplacian extracts thinned edges. The Laplacian operator is defined as:

$$\nabla^2 I_x(x,y) = \frac{\partial^2 I_x(x,y)}{\partial x^2} + \frac{\partial^2 I_x(x,y)}{\partial y^2} \tag{2.1}$$

Where $I(x,y)$ is the intensity of TEM image having (x,y) coordinates and $\nabla^2 I(x,y)$ is the second order derivative of the image. $\frac{\partial^2}{\partial x^2}$ and $\frac{\partial^2}{\partial y^2}$ are the second partial derivative in the ***x*** and ***y*** coordinates, respectively.

Canny edge detector contains five steps in which Gaussian filter is applied and the intensity gradient of the image for detecting vertical, horizontal and diagonal edges is found. Then using non-maximum suppression, double thresholding is used to find edges, and the possible edges are tracked by hysteresis (see Figure 2.13). The mentioned method allows obtaining empirical knowledge from components of TEM images and in particular an understanding of location and quantitative characteristics of pores. Applying the MO is necessary for gathering the contextual information of the pores in TEM images. On the other hand, using MOs requires determining the Structure Element (SE) as an important factor. SE is directly related to the structural information of the targeted object [116]. In this work a rectangular structure element was selected for searching the pores, and this was then slided along the image, rescaled and rotated to find the pores. The SEs were long rectangles selected due to the similarity to our object.

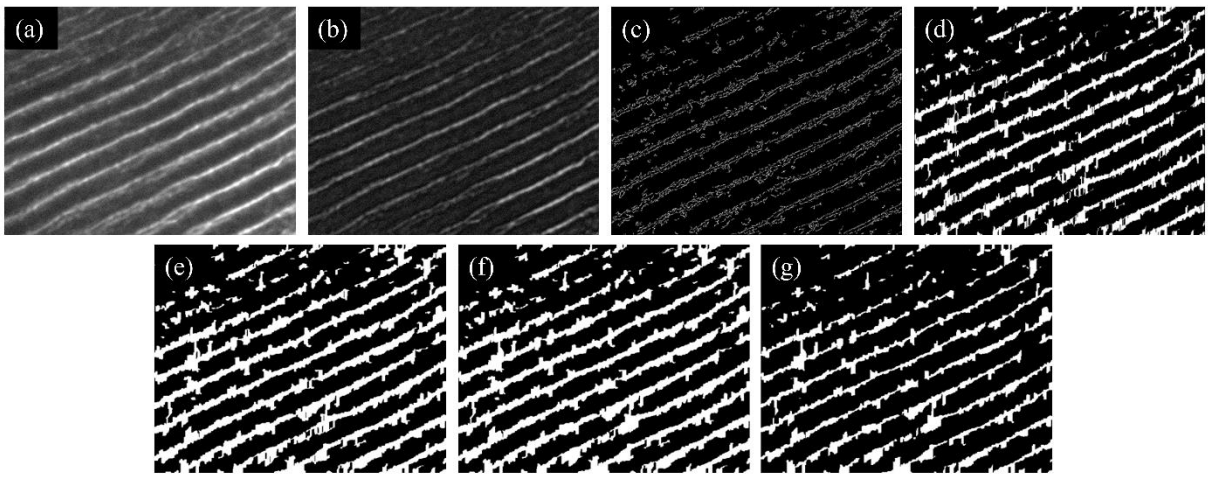

Figure 2.13. Example of results of MO applied to a TEM image: (a) the original TEM image of SA-0.98-700; (b) the background subtraction of the original image; (c) after Canny edge detection; (d) after closing operation; (e) after dilation; (f) after filling operation, (g) after erosion.

TEM images of samples SA-0.49-700 and SA-0.49-950 along with 001 orientations, and SA-0.98-700 and SA-0.98-950 1D channels along with 110 orientations are presented in Figures 2.14 and 2.15 respectively. The mesoporous structure was formed for these samples. The pore size distributions obtained via TEM image analysis are given in Figures 2.14 and 2.15 as well. Generally speaking, the pore diameter calculated from the image analyzer software would be expected to be smaller than the pore diameter obtained from nitrogen adsorption-desorption analysis, because of the uneven brightness and contrast of the TEM images. These uneven parts reduce the possibility for clearly finding the edge of the pores and make the thresholding less accurate. The mean pore diameter obtained from TEM images for samples: SA-0.49-700, SA-0.49-950, SA-0.98-700, and SA-0.98-950 are in the range of 5.1 to 7.6 nm. Image analysis calculation on SA-0.49-Y sample shows a slightly smaller average pore size compared to SA-0.98-Y. These data follow the same trend as reported above (see Table 2.1) from nitrogen adsorption-desorption analysis. TEM images of sample SA-0.98-X revealed the formation of ordered aligned pores which is in good agreement with the presence of an intense peak in SAXS analysis (Figure 2.11) [117].

It can be seen that the pore structure characteristic depends on calcination temperature. By increasing the calcination temperature, the size, and density of pores are changed. For SA-0.49-Y and SA-0.98-Y, an increase in calcination temperature from 700°C to 950°C results in a growth of 37% and 13% in the pore diameter respectively, calculated by image analysis. TEM images of both SA-0.49-Y and SA-0.98-Y samples show that the mesoporous structures are resistant up to 950°C (see Figures 2.14 and 2.15). Comparing the percentage of pore size growth in samples SA-0.49-Y and SA-0.98-Y points out that the latter has a higher temperature resistance than the former.

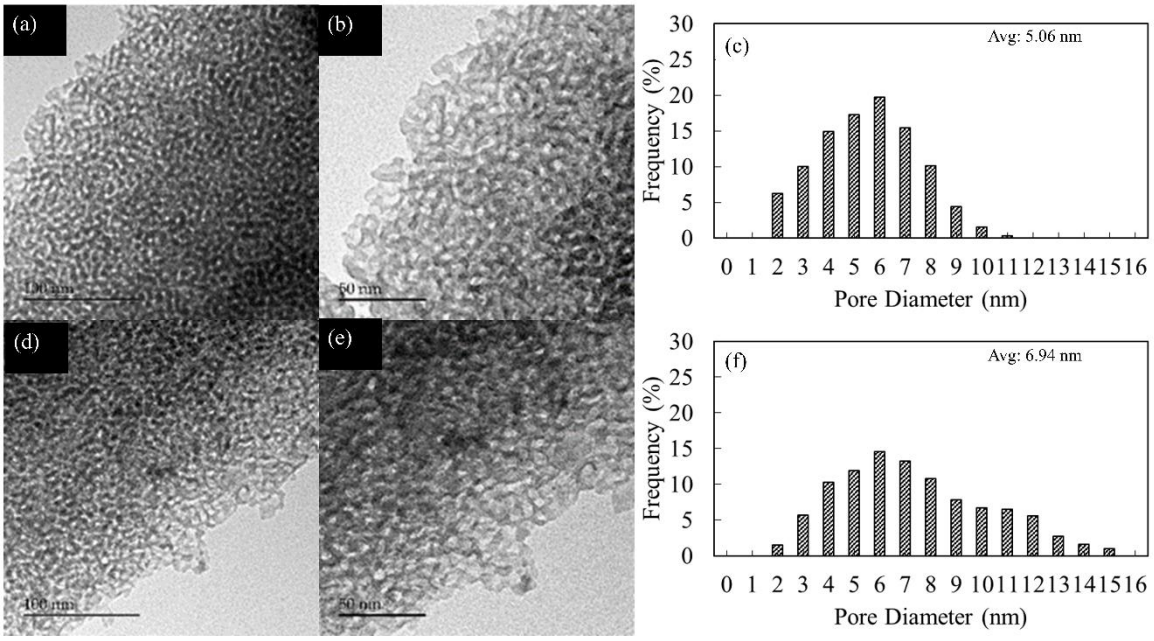

Figure 2.14. TEM images of (a, b) SA-0.49-700, (d, e) SA-0.49-950 view along 001 direction view and their corresponding image analysis histogram (c, f) at different magnifications.

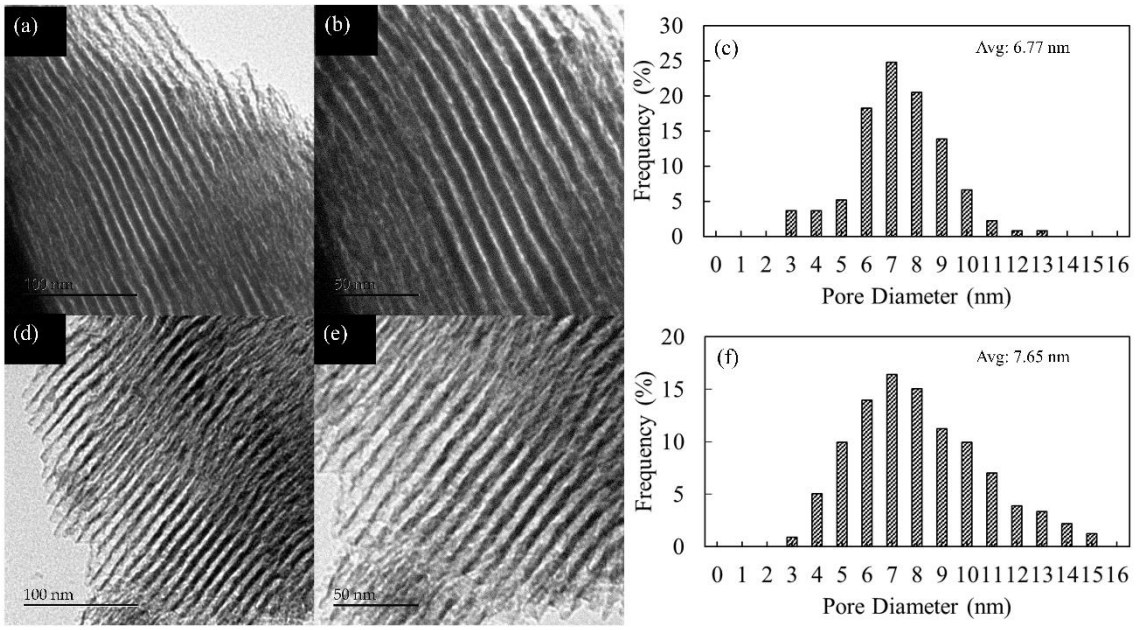

Figure 2.15. TEM images of (a, b) SA-0.98-700, (d, e) SA-0.98-950 view along the 110 direction and their corresponding image analysis histogram (c, f) at different magnifications.

As can be observed in Figure 2.16, TEM images of samples SA-1.47-700 reveals good periodicity with hexagonal 2D *P6mm* symmetry of uniform pores of *ca*.9.4 nm calculated from image analysis which is in accordance with the result of SAXS [118]. The TEM images confirmed that the P123 concentration has an important effect on the formation of porous structure, so that mean pore diameter of sample SA-1.96-700 reaches 4.8 nm, showing a 48% reduction from SA-1.47-700. Also, sample SA-1.96-700 showing smaller pores as compared to SA-1.47-700 is in good agreement with data presented in Table 2.1. During the aging step, the EISA process occurred. In this stage, a high concentration of P123 increases the viscosity. This high viscosity inhibits the mobility of surfactants and consequently the micelle formation [57]. Specifically, in the case of the sample with P123/Al(O-i-Pr)$_3$ = 1.96, the mesoporous structure is not completely formed, and some Al_2O_3 wraps the mesoporous domains which results in a significant reduction in ordering and homogeneity [119]. For this reason, despite the relatively large average pore diameter, the surface area and pore volume of sample SA-1.96-700 is quite small (see Table 2.1). It seems that at a higher P123/Al(O-i-

$Pr)_3$ ratio (1.47 and 1.96), mesoporous structures show a lower thermal resistance when the temperature increases. To be able to perform the image analysis, porous and well-formed sections of samples SA-1.47-700 and SA-1.96-700 were selected.

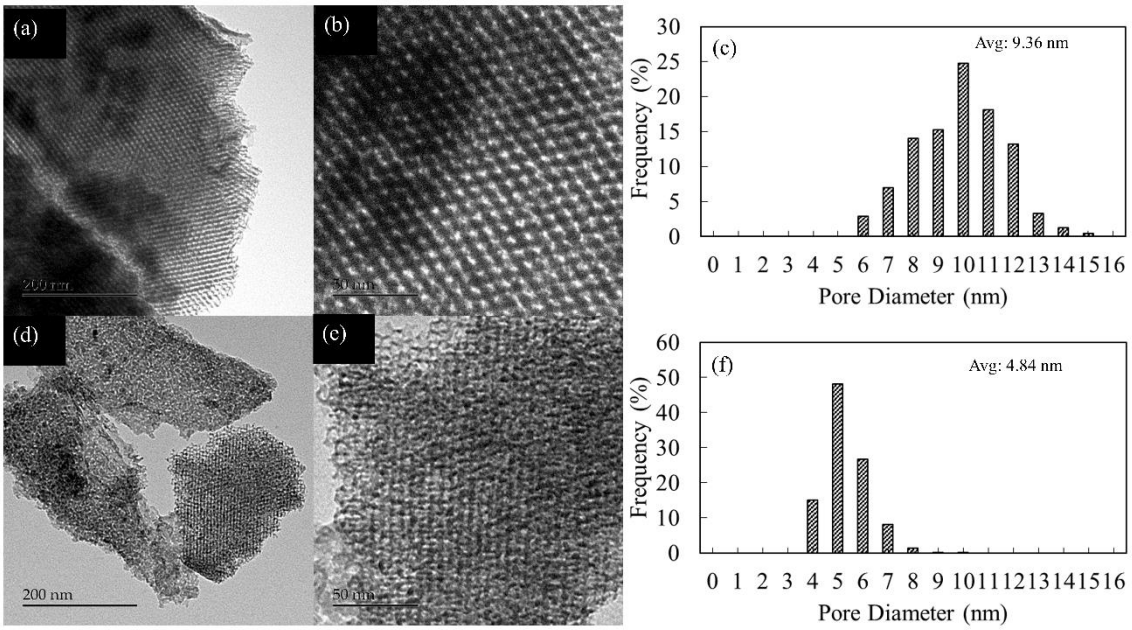

Figure 2.16. TEM images of (a, b) SA-1.47-700 and (d, e) SA-1.96-700 along with 001 direction and their corresponding image analysis histograms (c, f).

At higher calcination temperatures sample SA-1.47-950 and SA-1.96-950 revealed partial collapse forming some nanofiber morphology (Figure 2.17 a-d). The porosity of these samples is made by means of close packing of crystalline particles with some loss of mesoporous zones.

As shown in Figure 2.17 (e, f) and Figure 2.9, in sample SA-1.47-1050, increasing the calcination temperature to 1050°C leads to the alumina phase transformation from metastable γ-alumina to stable α-alumina. As a result, a significant collapse and sintering of the porous structure are observed [120], for all samples whatever the loading of P123 sintered at 1050°C. The TEM images of sample SA-1.47-1050 are presented here as an example.

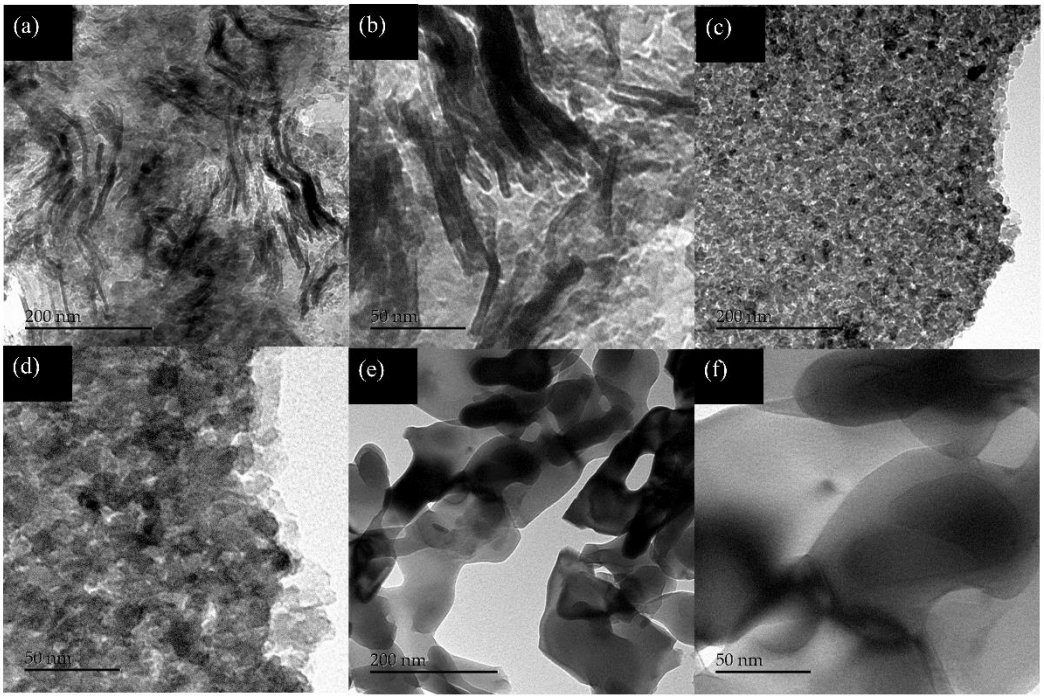

Figure 2.17. TEM images of (a, b) SA-1.47-950, (c, d) SA-1.96-950 and (e, f) SA-1.47-1050 at different magnification factors.

Micrographs of sample SA-0.98-700 along the 110 direction were used to measure the visible pore length distribution (Figure 2.18). All slabs include long range ordered pores which are proportional to the slab length. After measuring the length of at least 500 pores, the maximum and minimum length values of ≈ 2398 nm and ≈ 26 nm with the average of ≈ 801 nm were established for sample SA-0.98-700.

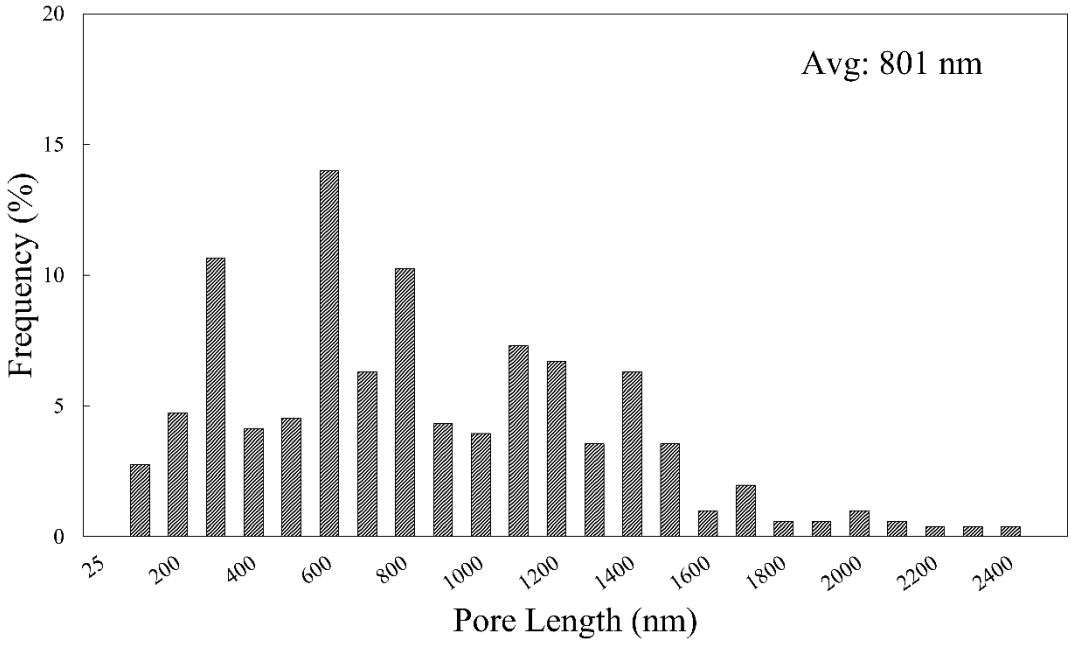

Figure 2.18. Pore length histogram of sample SA-0.98-700.

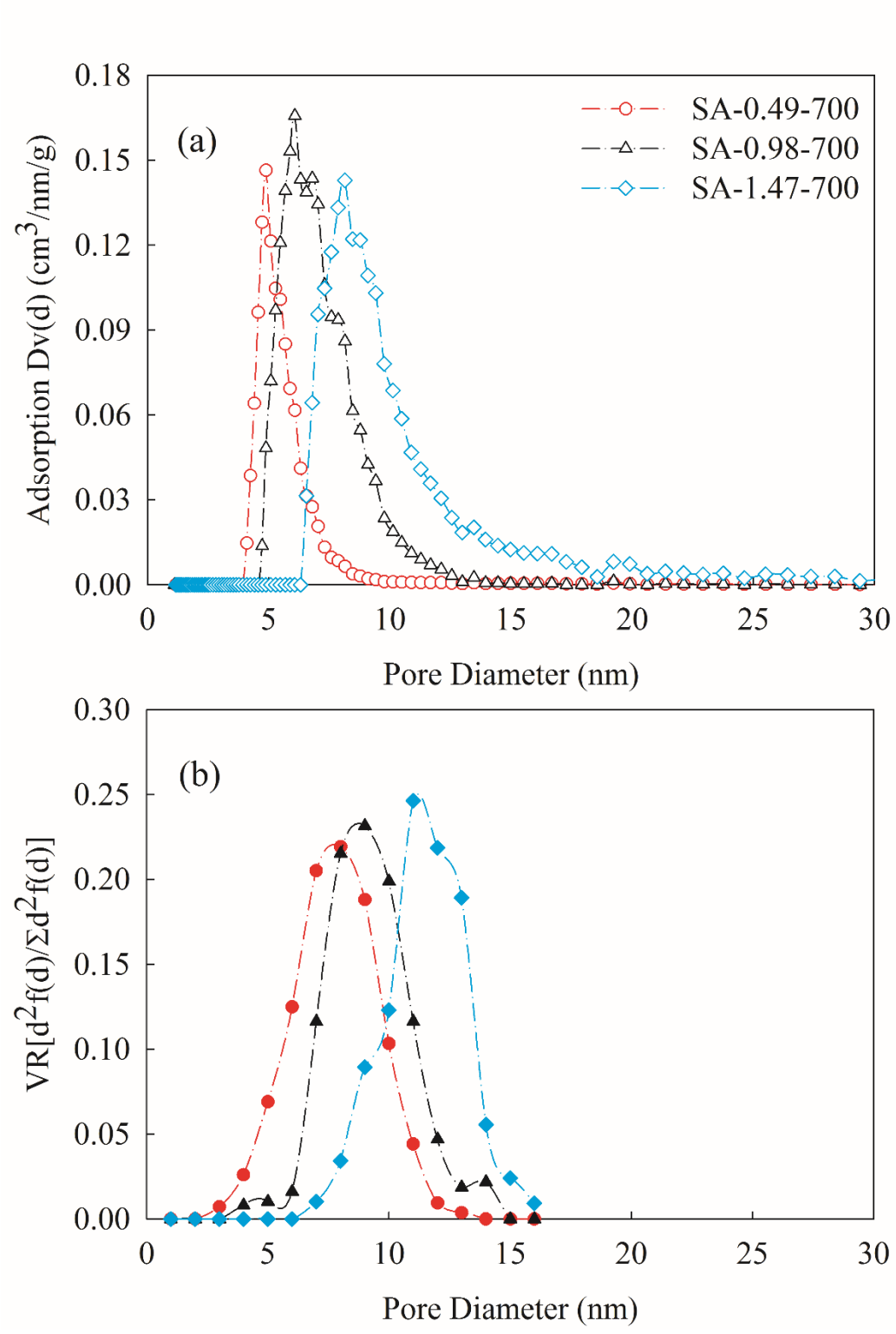

Figure 2.19. Pore size distributions of calcined samples (a) N_2-adsorption-desorption analysis, (b) image analysis.

2.3.5.2 Comparison of pore size distributions measurement methods

Since the literature on mesostructured materials reports essentially only PSDs established from nitrogen adsorption-desorption isotherms a comparison of PSDs obtained by this method and by image analysis for the same samples is of general interest. The PSDs derived from nitrogen isotherms such as those presented in Figures 2.2-2.5 are picturing frequencies of pore volumes of different sizes $D_v(d)$. The PSDs obtained by image analysis rather correspond to frequencies of pore numbers of different sizes f(d). Since the pore length distribution may be assumed to be independent of pore diameter, the pore volume frequency may be considered proportional to $d^2f(d)$. Thus for the comparisons presented in Figures 2.19 and 2.20, the PSDs established from image analysis are reported as the normalized distributions:

$$V(d) = \frac{d^2 f(d)}{\sum d^2 f(d)} \qquad (2.2)$$

The comparison of results in Figure 2.19(a) and (b) shows that even though some deviations on the d values are observed, the general shape and evolution of PSD with P123/$Al(O\text{-}i\text{-}Pr)_3$ mass ratio are represented.

In Figure 2.20, the two distribution determinations for sample SA-1.96-700 essentially fit, except for a tailing at higher pore diameter, observed on NLDFT determined PSD.

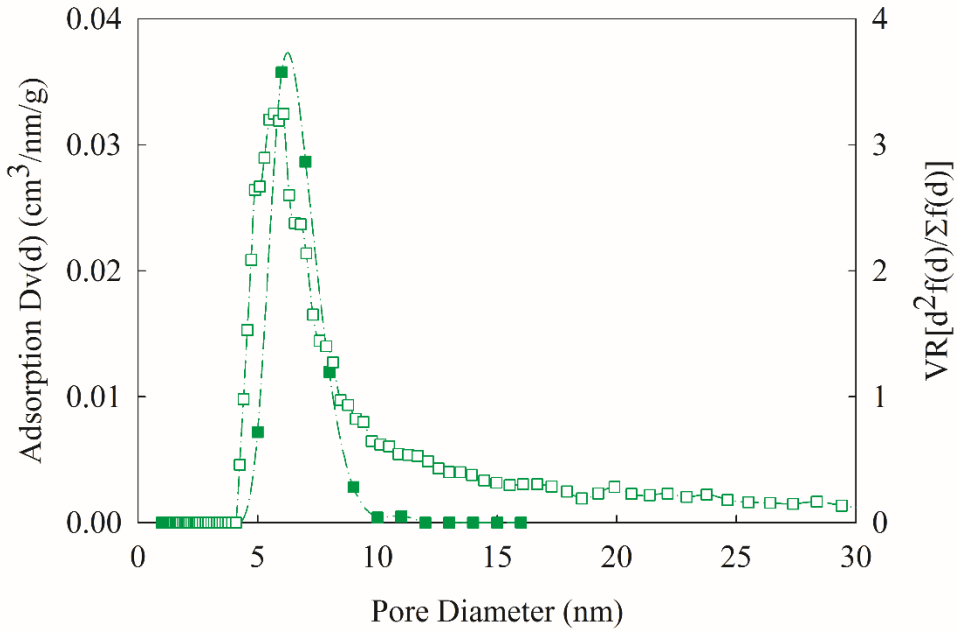

Figure 2.20. Pore size distribution of sample SA-0.196-700. Open symbols obtained from N_2-adsorption-desorption analysis, close symbols calculated from image analysis.

2.4 Conclusion

Mesoporous alumina was one-pot synthesized via the polymeric surfactant template assisted sol-gel method, along with the EISA process using $Al(O\text{-}i\text{-}Pr)_3$ as an aluminum source and the non-ionic surfactant P123. Different contents of P123 were utilized in the synthesis gel, and a series of calcination temperatures from 650°C to 1050°C was used. Increasing the P123/$Al(O\text{-}i\text{-}Pr)_3$ mass ratio from 0.49 to 1.96 resulted in the formation of different pore morphologies. Among all samples synthesized with different polymer contents, samples SA-0.98-700 and SA-1.47-700 showed the highest surface areas with only a small difference between them. The latter showed a higher pore volume and pore diameter. The P123/$Al(O\text{-}i\text{-}Pr)_3$ ratio in the range of 0.98 to 1.47 and the calcination temperature of 700°C are therefore suggested to produce samples with high surface area and volume. The increase in calcination temperature resulted in the formation of larger pores but reduced surface area and pore volume for all samples. This is likely due to the crystal growth within the framework causing partial collapse which reduces the ordering of the structure. Samples were also thermally and

structurally analyzed: the minimum temperature of 700°C and a soaking time of 3 h (at this temperature) is required to fully remove the template and let the formation of mesoporous γ-alumina. Therefore, it is suggested that to reduce the energy cost in the fabrication step, and also to reach maximum surface area, this optimum condition be implemented. According to the XRD and N_2 adsorption-desorption analysis, all samples retained their porosity and were thermally stable up to 950°C, but increasing the temperature to 1050°C, drastically reduced their surface area and total pore volume. Tracing the phase transformation with XRD, revealed that the γ-phase remained intact up to 950°C. Above this temperature (at 1000°C) a polymorph of γ and α phases coexisted and finally at 1050°C the γ-phase disappeared completely. At this temperature, structure collapse happened, and a sharp increase in crystal domain size to 29.6 nm was observed. The morphological evaluation using TEM image analysis revealed that an ordered hexagonal structure with dimensions in the range close to 5 to 10 nm was produced, resulting in the high surface area of the samples. TEM observation shows that the total average length of pores in a single alumina slab is proportional to the size of the slab and its average value was found to be around 800 nm.

In summary, polymeric template assisted sol-gel process using the EISA method again proved to be a convenient method for producing mesoporous γ-alumina with high surface area, small crystal domain size, and high chemical purity due to the homogeneity of the initial materials. Furthermore, samples SA-0.98-700 and SA-1.47-700 (despite the lower degree of ordering) offer the possibility of being used in different applications, such as automobile emission control, adsorbents, separators and catalyst supports in refining industry; due to their high thermal stability, relatively large pore diameter, high surface area and total pore volume. These properties permit high loading of reactive catalytic species and improve the mass transfer of reactant molecules. Tailoring and optimizing the textural properties of the organized mesoporous alumina enhance their potential to be used in such applications. One special feature of the present paper is the demonstration of image analysis as a tool for measuring pore size as well as pore length distributions.

Acknowledgment

We thank Prof. Dongyuan Zhao for access to Fudan University small-angle X-ray scattering equipment. We acknowledge Dr. Bardia Yousefi at Computer Vision and Systems Laboratory (CVSL) from the Department of Electrical and Computer Engineering at Laval University for his constructive comments and help on image analysis. The financial support of Natural Science and Engineering Council of Canada (NSERC) is gratefully acknowledged.

Chapter 3

Green diesel production via continuous hydrotreatment of triglycerides over mesostructured γ-alumina supported NiMo/CoMo catalysts

Arsia Afshar Taromi and Serge Kaliaguine, Fuel Processing Technology, Volume 171, March 2018, Pages 20-30.

Résumé

Dans la présente étude, la désoxygénation de l'huile de canola a été effectuée dans un réacteur à lit fixe continu. Une alumine-γ mésostructurée avec des pores et des domaines cristallins de taille nanométrique dans la gamme de 8 nm a été synthétisée en une seule étape par une voie sol-gel accompagnée d'un auto-assemblage induit par évaporation (EISA) en présence d'un gabarit polymère. Les catalyseurs nanoporeux ont été préparés en utilisant un procédé de co-imprégnation par voie humide (incipient wetness co-impregnation) suivie d'une étape de calcination, 15% en poids de MoO_3 et 3% en poids de NiO ou CoO, ont été imprégnés sur le support nanoporeux. Les deux catalyseurs ont favorisé la voie de réaction d'hydrodésoxygénation et les hydrocarbures liquides étaient principalement constitués de n-alcanes en C15-C18. Les effets du LHSV et de la température sur la composition du produit liquide ont été étudiés dans la gamme de LHSV: 1 à 3 h^{-1} et une température de 325 à 400°C, tout en maintenant les autres conditions réactionnelles constantes à une pression de 450 psi et un rapport H_2/huile de 600 $mLmL^{-1}$. Une activité catalytique légèrement meilleure a été perçue pour NiMo-S/alumine-γ à une LHSV plus élevée par rapport au catalyseur CoMo-S/alumine-γ. La conversion en liquide sur NiMo-S/alumine-γ est supérieure à celle de CoMo-S/alumine-γ dans la plage de température de 325 à 350°C. À 375°C, la conversion a atteint 100% sur les deux catalyseurs. La production de produits liquides dans la gamme du diesel vert sur NiMo-S/alumine-γ et CoMo-S/alumine-γ a été jugée optimale à 325°C et 1 h^{-1} LHSV.

Abstract

In the present study, the deoxygenation of canola oil was performed in a continuous fix-bed reactor. Wormhole-like mesostructured γ-alumina with nano-sized crystalline domains and pores in the range of 8 nm was one-pot synthesized using polymeric template assisted sol-gel method via evaporation-induced self-assembly (EISA). Nanoporous catalysts were prepared by employing the incipient wetness co-impregnation method followed by a calcination step, 15% wt. MoO_3 and 3% wt. NiO or CoO, were impregnated on the nanoporous support. Both catalysts favored the hydrodeoxygenation reaction pathway, and the liquid hydrocarbons consisted mostly of C15-C18 n-alkanes. The effects of LHSV and temperature on the liquid product composition were investigated in the range of, LHSV: 1 to 3 h^{-1}, and temperature of 325 to 400°C while keeping other reaction conditions constant at a pressure of 450 psi and H_2/oil of 600 $mLmL^{-1}$. Slightly better catalytic activity was perceived for NiMo-S/γ-alumina at higher LHSV compared to CoMo-S γ-alumina catalyst. The liquid conversion on NiMo-S/γ-alumina is higher than that on CoMo-S/γ-alumina over the temperature range of 325 to 350°C. At 375°C, the conversion reached 100% over both catalysts. The production of green diesel range liquid products over NiMo-S/γ-alumina and CoMo-S/γ-alumina was found optimal at 325ºC and 1 h^{-1} LHSV.

3.1 Introduction

The increasing energy demand, worries over the exhaustion of fossil fuels and environmental pollution have led many researchers to investigate alternative sources of energy. Fossil fuels are presently the essential source of energy, but they increase the overall greenhouse gas (GHG) emission, particularly carbon dioxide (CO_2) which causes global warming. Among different available alternative of renewable energies such as hydropower, solar power, wind power and fuel cells, biomass is the only source capable of storing the produced energy in the form of materials. Furthermore, biomass is carbon-neutral and do not partake in GHG emission. The biomass-derived products which can be solid, liquid, or gas could be used as fuel or as raw materials to produce downstream value-added products such as polymers and chemicals (bio-based). These products are currently derived from fossil fuel sources and thus reduce their consumption. Besides, the use of biomass can generate hiring personnel in the different geographical sector, strengthening the economy and reducing the rural to urban area migration [121], [122].

Presently, the only feasible, green renewable source for producing liquid fuels is lipid feedstock. Lipid feedstocks cover vegetable oils, animal fats, waste cooking oils and the oils derived from microalgae [15], [123]–[127]. Triglycerides are the main components of all vegetable oils and fat structures. The significant difference between various vegetable oils is in the type of fatty acids in the triglyceride molecules. They are formed from a single molecule of glycerol combined with three molecules of fatty acid. The alkyl chains of triglycerides could be saturated, monounsaturated, or polyunsaturated. They are usually categorized based on their length and degree of saturation. The chain length of these fatty acids in naturally occurring triglycerides could be of varying lengths; but 16, 18 and 20 are the dominant ones with a maximum of three unsaturated bonds. One of the processes which make it possible to fabricate high quality (oxygen, sulfur, and aromatic free) fuels is the deoxygenation process of bio-derived triglycerides [128]. Less greenhouse gas emission, domestic production resulting in the improvement of agronomics in the rural zones and increased national energy security due to less dependence on fossil fuels are some of the benefits of green-based fuels [18]. The fatty acid methyl ester (FAME) which is also known as first generation biodiesel is presently made from the transesterification of vegetable oils

with alcohols. As a result of the different chemical composition of esters (C=C and C=O bonds remain) [12] and hydrocarbons, biodiesel has some drawbacks for use in the diesel engine [53]. The presence of unsaturated double bonds results in low oxidation stability, low heating value, corrosion problems, etc. The flash point of FAME is also high compared to normal diesel. Another important alternative fuel made from renewable resources such as vegetable oils is green diesel, which is also known as the second generation of biodiesel and is a result of hydrotreatment of vegetable oils. During hydrotreatment, all of the unsaturated C=C bonds are hydrogenated, and all of the oxygen molecules are removed. Therefore, the final product comprises a mixture of long chain alkanes with a carbon number in the diesel-range [12], [129].

Existing petroleum refinery infrastructure could be used for the hydrotreatment of triglycerides, but the catalysts should be modified for this process due to the different nature of the reactants. The high activity and selectivity for the target products are the key factors of a suitable catalyst [130], [131]. Since the energy input during the process is an important issue, finding a suitable catalyst in which the requested conversion conditions are milder, is contemplated. Conversion of triglycerides to green diesel at elevated pressure and temperature consists of three main pathways namely: hydrodeoxygenation (HDO), decarbonylation (DCO) and decarboxylation (DCO_2). Among them, HDO is an exothermic reaction which removes oxygen from triglyceride molecules in the form of water. In this case, the hydrotreated product is normal alkane with the same carbon number as the corresponding fatty acid. DCO and DCO_2 are both mildly endothermic and remove the oxygen molecules in the form of CO/water and CO_2 respectively, and water. If the reaction goes through these two paths, the produced n-alkanes have one carbon less than the initial corresponding fatty acids. Among these three pathways, decarboxylation has the lowest hydrogen consumption, 1 mol of hydrogen per ester bond, while decarbonylation requires 2 mol of hydrogen per ester bond and hydrodeoxygenation needs the highest amount of 4 mol of hydrogen [33], [37]. Thus, finding a low-cost catalyst and economical process conditions is worth exploring. Two classes of catalysts have been reported as potent catalysts to convert vegetable oils to diesel range hydrocarbons: high-cost noble metal catalysts (such as supported Pd, Pt) and low-cost sulfided hydrotreating bimetallic catalysts (such as Ni-Mo, Co-Mo, Ni-W) loaded on porous supports. [31], [49], [52], [53], [70]. In this study, nanoporous sulfided bimetallic catalysts

(NiMo/γ-alumina and CoMo/γ-alumina) were prepared and used. The catalytic performance is predominantly affected by the support porous structure properties including specific surface area, pore size, pore volume and crystal phase. Thus, to develop the catalysts for the production of green diesel from canola oil; first, a high surface area mesoporous γ-alumina support was synthesized by employing sol-gel method via EISA process. The catalysts were then formed by loading the active metals on the mesoporous γ-alumina and used in the hydrotreatment process. A comparison was made between the performance of NiMo/γ-alumina and CoMo/γ-alumina catalysts for green diesel production from canola oil in a continuous fixed bed reactor over the temperature range of (325-400°C), and liquid space velocity range of (1-3 h^{-1}). Moreover, the influences of temperature and LHSV on the composition of the final liquid products were also highlighted.

3.2 Experimental

The selected triglyceride source to produce green diesel was Canola oil which was supplied by Saporito Inc., Canada. The fatty acid's composition in feed oil, provided by the manufacturer is presented in Table 1.1.

Table 3.1. Fatty acids content (% wt.) in Canola oil.

Structure	Formula	Name	% wt.
C16:0	$C_{16}H_{32}O_2$	palmitic	4.1
C18:0	$C_{18}H_{36}O_2$	stearic	1.8
C18:1	$C_{18}H_{34}O_2$	oleic	62.7
C18:2	$C_{18}H_{32}O_2$	linoleic	19.6
C18:3	$C_{18}H_{30}O_2$	linolenic	9.0
C20:0	$C_{20}H_{40}O_2$	arachidic	0.6
C22:0	$C_{22}H_{44}O_2$	behenic	0.3

3.2.1 γ-alumina synthesis

Mesostructured wormhole-like γ-alumina with high surface area was synthesized through template-assisted sol-gel method. Initially a specific amount of Pluronic P123 (poly (ethylene

oxide)$_{20}$-poly(propylene oxide)$_{70}$-poly(ethylene oxide)$_{20}$ triblock copolymer), (Average Mn ≈ 5800 g/mol, Sigma-Aldrich, CAS no. 9003-11-6), as a soft template, was dissolved in 60 mL of anhydrous ethanol (Commercial Alcohols, CAS no.67-17-5) using a magnetic stirrer at ambient temperature. 4.2 mL of HNO_3 69% wt. (Sigma-Aldrich, CAS no. 7697-37-2) was added to the solution to regulate the pH. Then the aluminum source was added to the solution in the form of 30 mmol of Al(O-i-Pr)$_3$ (Sigma-Aldrich, CAS no. 555-31-7). The molar composition of the reaction mixture Al(O-i-Pr)$_3$/P123/Et-OH/HNO_3 was 0.03/0.0010/1/0.1. All chemicals were used as received without any purification. The solution was unceasingly stirred at ambient temperature overnight. Then, the solution was poured into Petri dishes and kept at 60°C for four days which let the solvent evaporate during EISA process. The obtained sample was then calcined while the temperature increased from ambient to 700°C (3 h soaking time) with a heating rate of 1°Cmin^{-1}. The slowly employed heating rate prevents the formation of any collapse in the alumina structure due to quick dehydration, non-uniform heat transfer, and fast grain growth.

3.2.2 Catalyst synthesis

NiMo and CoMo catalysts were prepared using a wet co-impregnation method of the γ-alumina support (NiMo/γ-alumina and CoMo/γ-alumina). The synthesized flakes of γ-alumina support were ground and sieved before being impregnated with catalysts precursor solution via the simultaneous co-incipient wetness. The chemicals used for catalyst preparation were ammonium molybdate (VI) tetrahydrate ($(NH_4)_6Mo_7O_{24}\cdot 4H_2O$), CAS no.12054-85-2, nickel (II) nitrate hexahydrate (Ni $(NO_3)_2.6H_2O$), CAS no.13478-00-7 and cobalt (II) nitrate hexahydrate ($Co(NO_3)_2\cdot 6H_2O$), CAS: 10026-22-9, all purchased from Sigma-Aldrich. The loadings of metal oxides were adjusted to 15% wt. MoO_3, and 3% wt. NiO or CoO. The materials were mixed for 12 h at 60°C in a jacketed Pyrex reactor. In the next step, the resulting materials were dried at 60°C overnight, then ground to form a homogenous powder. Subsequently, the catalysts were formed through a calcination step from 25 to 700°C with a heating rate of 1°Cmin^{-1} with a 3 h soaking time and a heating rate of 1°C min^{-1} in an air flow. They were pressed in the form of pellet disks and crushed before being loaded into the reactor. The designation of NiMo and CoMo were used for calcined

NiMo/γ-alumina and CoMo/γ-alumina catalysts, respectively, while NiMo-S and CoMo-S were used for sulfided ones.

3.2.3 Characterization

3.2.3.1 Nitrogen adsorption-desorption analysis

This analysis was conducted using a Quantachrome Nova 2000 instrument at -196°C. The Autosorb-1 software, (Quantachrome Instruments) was used for all calculations. Before the test, a specific amount of sample (around 400-500 mg) was degassed at 200°C under vacuum for 5 h until a residual pressure of 10^{-6} mbar was achieved. Standard Brunauer-Emmett-Teller (BET) equation was employed to determine the specific surface area (S_{BET}) of the sample in the range of 0.05-0.2 (linear part) relative pressure (P/P_0). The volume of adsorbed nitrogen at the relative pressure of $P/P_0 = 0.99$ was used for the total pore volume (V_t) calculation. To calculate the pore width, the Barrett-Joyner-Halenda (BJH) method was used considering the adsorption branch of the isotherms. Non-local density functional theory (NLDFT) method was also used to calculate the specific surface area, total pore volume and pore width (S_{DFT}, V_{DFT}, and W_{DFT}, respectively). The determination of the pore size distribution was done using the kernel of NLDFT applying the equilibrium isotherm of N_2 at -196°C on silica, considering the cylindrical shape of pores.

3.2.3.2 X-ray diffraction (XRD)

Patterns of wide-angle X-ray scattering (WAXS) were obtained using a Siemens D5000 diffractometer with a monochromatized radiation source of Cu Kα (wavelength of 0.154059 nm); working at a constant power source of 40 kV and 30 mA at ambient temperature. Counts in the range of 10 to 90°, were collected at a scan speed of 1°/min every 0.02° (2θ). Before the analysis, the samples were finely ground (< 100 µm). Phase recognition was carried out comparing the obtained diffraction patterns with those in Joint Committee on Powder Diffraction Standards (JCPDS) database. Warren's correction for instrumental broadening using Scherrer's formula: $D = K\lambda/\beta\text{Cos}\theta$, was used to roughly determine the average crystallite size of samples, where $K \approx 0.9$ (Scherrer constant), $\lambda = 1.54059$ Å, and θ is the Bragg's diffraction angle position. By using $\beta^2 = B^2 - b^2$ formula, β (effective linewidth of the X-ray reflection) is calculated. B and b (both in radians) represent the full width half

maximum (FWHM) and instrumental broadening established using the FWHM of quartz X-ray reflection, including particles larger than 150 nm, at $2\theta \approx 27°$ [99]. The lattice parameters (a) are calculated by incorporation of the interplanar spacing d_{hkl} set of cubic lattice planes [132].

$$d_{hkl} = \frac{\alpha_{hkl}}{\sqrt{h^2+k^2+l^2}} \quad (3.1)$$

where *h,k,l* are the Miller integer indices for a set of lattice planes.

3.2.3.3 X-ray photoelectron spectroscopy (XPS)

To determine the type of metal oxides species and their sulfides on the surface of catalysts, a KRATOS Axis-Ultra electron spectrometer (UK) was used to collect X-ray photoelectron spectroscopy (XPS) spectra, which worked at a power of 300 W with a monochromatic Al Kα X-ray excitation source. The vacuum was in the range of 10^{-8} Torr, and the samples were placed in a stainless steel cup. To optimize the counting rate parameters and the energy resolution, the electrostatic charge was neutralized using a very low energy integrated electron flood gun. The survey spectra were recorded using a pass energy of 160 eV and a step size of 1 eV. High-resolution Ni2p, Co2p, Mo3d, S2p and C1s spectra were recorded with pass energies of 20 or 40 eV, and step sizes of 0.05 and 0.1 eV respectively. The CasaXPS version 2.3.17PR1.1 software was used for the deconvolution of the collected spectra. Au4f7/2, Ag3d5/2, and Cu2p3/2 at binding energies of 83.95, 368.2, 932.6 eV, respectively, were used to calibrate the instrument. Binding energies were corrected by setting the C-H carbon peak at 285.0 eV.

3.2.3.4 Electron probe microanalysis

CAMECA SX-100 Electron Probe Micro-Analyzer (EPMA) possessing 5 wavelength dispersive X-ray spectroscopy (WDS) spectrometers was used to chemically analyze Al, Mo, Ni, Co, and S. Samples were mounted in epoxy resin under vacuum, succeeding a polishing down with diamond abrasives to 1 μm. The analyses were executed with a 1 μm beam size and a 100 nA beam current at a 15 kV accelerating voltage.

3.2.3.5 Transmission electron microscopy (TEM)

A JEM-1230 (JEOL) transmission electron microscope possessing a lanthanum hexaboride (LaB6) filament thermionic emission source was used for morphological analysis of the samples. Gatan Ultrascan 1000XP was employed adjusting the electron beam acceleration voltage to 80 kV. Samples were finely ground and dispersed in methanol following mild sonication for 10 min. Then a drop of solution (≈ 5 µL) was placed uniformly on a Formvar film coated nickel grid (200 mesh) by a pipette. The grid was dried in air at ambient temperature before the analysis.

3.2.3.6 Fourier transform infrared spectroscopy (FTIR)

BIO-RAD FTS-60 FTIR spectrometer, in transmission mode, was used to collect the infrared spectra of liquid samples. A drop of liquid was placed on the sample holder between 2 KBr round crystal windows (diameter × thickness = 25 mm × 4 mm). The data were collected in the range of 4000 to 400 cm^{-1}, averaging 32 scans.

3.2.3.7 High-performance liquid chromatography (HPLC)

The liquid samples were analyzed for their triglycerides (TG), diglycerides (DG) and monoglycerides (MG) content employing UHPLC (UltiMate 3000 Dionex) equipped with a UV detector (Thermo SCIENTIFIC Dionex UltiMate 3000). An AcclaimTM 120, C18, 5 µm, 120 A, 4.6 × 100 mm column was used for the separation. The calibration curves were obtained by injecting a series of ten triglycerides samples of known concentration. Acetonitrile, hexane, and isopropanol (HPLC grade - Fisher Scientific) were used as eluent solvents with a flow rate of 0.5 $mLmin^{-1}$. The injection volume of 10 µL and the measurement time of 60 min were selected to have a complete drainage of the injected liquids. Sigma-Aldrich analytical standards were used for peak identification. During the analysis, the gradient elution mode was set. Each analysis was repeated three times.

3.2.3.8 Gas chromatography-mass spectrometry (GC-MS)

To separate the distilled products and provide a detailed distribution of liquid components, GC-MS analysis was performed. The analyses were carried out using a Thermo Scientific™ ultra-trace GC ITQ-900 ion trap spectrometer equipped with a flame ionization detector (FID) and a DB-5ms 30 m, 0.25 mm, 0.25 µm column (Agilent). The equilibrium temperature

of the GC oven was set to 70ºC for 30 s. The MS source and the FID detector temperatures were adjusted at 200 and 220ºC, respectively. The column temperature was increased from the equilibrium temperature (70ºC) to 300ºC with a heating rate of $10^{o}Cmin^{-1}$ and kept at this temperature for 15 min. To let all the components exit, the column temperature was raised to 350ºC and held 10 min at this temperature. The scan spectra were acquired from 50 to 650 m/z. The injected volume was 1 µL and the samples were diluted with GC grade, CS_2, (Sigma-Aldrich, CAS no.75-15-0). The GC-MS instrument was calibrated using ASTM-D2887 quantitative calibration solution (Supelco). Xcalibur™ Software version 2.1 was used for data acquisition and analysis.

3.2.4 Catalytic tests

A tubular reactor made of stainless steel 316 with an internal diameter of 25.8 mm and a height of 400 mm, yielding a volume of 209 cm^3, was used for hydrotreatment process. The temperature of the system was controlled by using a tubular electrical furnace manufactured by Thermoscientific Industries. A second thermocouple was installed inside the reactor below the bottom of the catalyst bed to read the temperature of the reactor. Oil was fed into the reactor at a constant rate with high-pressure HPLC pump, Lab Alliance Series II (0.01-10 $mLmin^{-1}$, 6000 psi max pressure). Meanwhile, hydrogen and nitrogen were introduced into the reactor from two high-pressure cylinders using Bronkhorst Co. mass flow controllers (2100 psi max pressure). The pressure in the reaction system was controlled by a back pressure regulator, 26-1700 Series, and an electro-pneumatic pressure controller, Tescom ER3000 series. Process parameters such as temperature, pressure and gas/liquid volumetric flow rate were controlled using LabVIEW 2010 National Instruments software. A condenser coupled with a cooling bath was set between the reactor exit and the high-pressure separator to collect liquid products. The catalyst bed was located in the middle of the reactor. A schematic diagram of the hydroprocessing setup is illustrated in Figure 3.1.

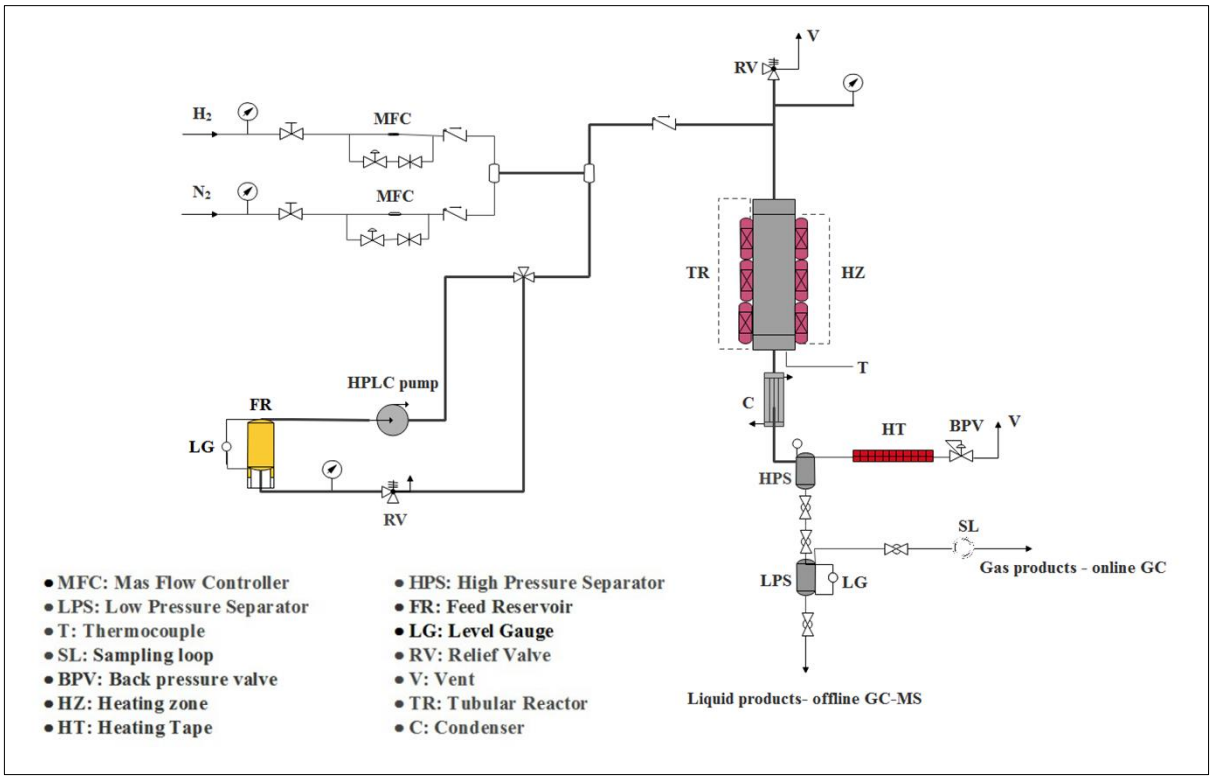

Figure 3.1. Simplified process flow diagram (PFD).

Hydrotreating of canola oil was performed in the reactor wherein the catalyst was loaded. Before the reaction, both CoMo and NiMo were pre-sulfided ex-situ in the same hydrotreatment reactor tube, by using a mixture of 10% H_2S in H_2 (a flow rate of 50 $mLmin^{-1}$), heating to 400°C at the rate of 10°C min^{-1}, and finally keeping at this temperature for 6 h. To maintain the catalyst in the active form 1-2% wt. of DMDS was added to the oil feed reservoir. Once the catalyst activation step was done, the reactor was cooled down to room temperature. Next, the reactor containing the sulfided catalyst was installed on the hydrotreatment unit. Then the reactor was heated and pressurized with N_2 to the required reaction pressure. While the temperature was increased, the oil flow rate was adjusted to the setpoint value in the feed circuit line. When the pressure and temperature reached the steady state, the oil and hydrogen were introduced into the reactor. The effect of LHSV and temperature on the liquid product composition were investigated at constant reaction condition of P = 450 psi and H_2/oil = 600 $mLmL^{-1}$. Triglycerides concentrations and the

distribution of normal alkanes in the product were calculated from HPLC and GC-MS analysis. The terms conversion (C) is hereafter specified as follows:

$$Conversion\ (C) = \frac{Total\ mass\ of\ triglyceride\ consumed}{Initial\ mass\ of\ triglyceride} \times 100 \quad (3.2)$$

3.3 Results and discussion

3.3.1 Nitrogen adsorption-desorption analysis

3.3.1.1 Mesoporous γ-alumina

The nitrogen adsorption-desorption isotherm and related pore size distribution curves of the prepared γ-alumina and catalysts are presented in Figure 3.2. In the case of γ-alumina (Figure 3.2a), the synthesized sample exhibits the classical shape of type IV adsorption-desorption isotherms with H2 type hysteresis loop slightly shifted to H3 type (representative of materials with channel-like or ink-bottle pore connectivity with a rather narrow pore size distribution representing pores with cylindrical morphology and numerous interconnections) [100]. The capillary condensation step is quite steep and starts at around (P/P_0) ≈ 0.44 indicating the presence of a uniform structure and a small mesopore diameter [133]. As can be observed in the inset of Figure 3.2a, the pore size distribution of this sample, centered at ca. ≈ 6 nm, is quite narrow. The large N_2-uptake at low relative pressure is caused by the monolayer adsorption of nitrogen molecules in the mesopores. The textural properties of the synthesized alumina are summarized in Table 3.2. A surface area of 259 m^2/g, a pore volume of 0.506 cm^3/g and an average pore diameter of 7.8 nm are obtained which shows that the mesoporous structure is well formed and thermally stable under the calcination conditions, which is consistent with TEM images (See Figure 3.7a, b, c, d). Such a sample with relatively high pore volume and large pores could be considered as a good catalyst support; this will facilitate the movement of heavy and large reactant molecules inside the pores towards the active sites and increases the active metal loading [48].

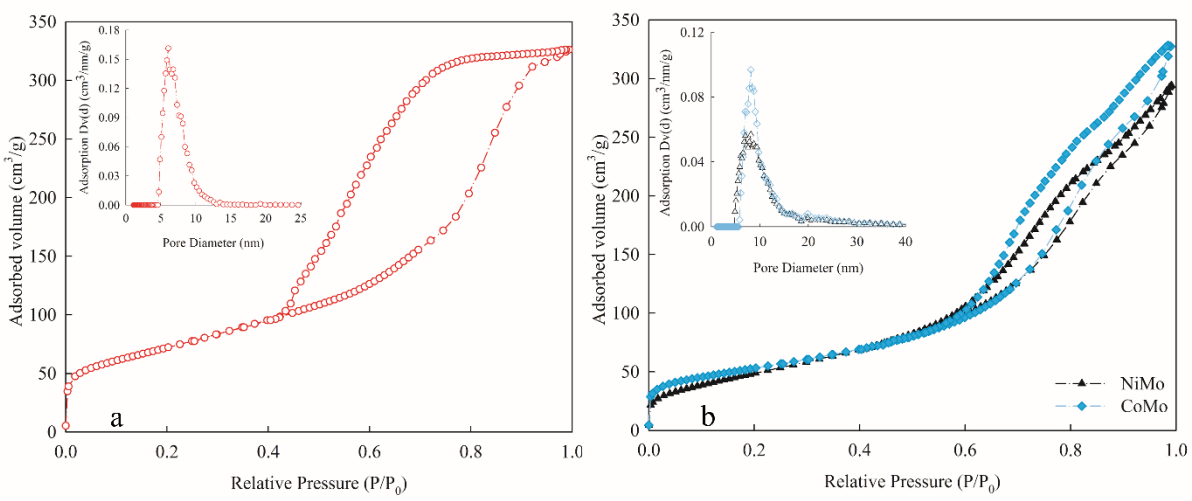

Figure 3.2. Nitrogen adsorption-desorption isotherms and the corresponding PSDs for (a): γ-alumina and (b): NiMo/CoMo samples.

3.3.1.2 NiMo and CoMo catalysts

The physisorption analysis at Figure 3.2b reveals the presence of type IV isotherm with an H3 type hysteresis loop without any adsorption limitation at high relative pressure which corresponds to the characteristic of slit-shaped mesoporous structure [25, 26]. As can be seen from the inset of Figure 2b the catalysts exhibit a quite narrow unimodal pore size distribution located in the mesopore region. Comparing the adsorbed volume of bare mesoporous γ-alumina support (Figure 3.2a) with both catalysts (Figure 3.2b); at relative pressure of P/P_0 = 1, the adsorbed volume remains the same as support in CoMo and slightly shifts to lower values in NiMo, which are around 330 and 300 cm^3/g (STP) respectively. Upon impregnation, the surface area and pore volume did not vary much for both catalysts; a 28.6% reduction in the surface area is observed for both catalysts to an average of 185 m^2/g. The total pore volume of NiMo showed a 10% reduction to 0.457 cm^3/g, but for CoMo the total pore volume remained the same as γ-alumina. The average pore width increased in both catalysts to 10 and 10.8 nm for NiMo and CoMo, respectively. The pore size distributions of NiMo and CoMo catalysts are quite narrow but broader than that of bare γ-alumina and has shifted to higher values, respectively centered at ca. 8.1 nm and 7.6 nm which corresponds to an increase of 37% and 29%. The formation of the hysteresis loop at higher relative partial

pressure compared to bare alumina indicates the presence of larger pores in the catalysts [135].

This reflects the filling of small pores with metal oxides or/and the formation of pores with larger diameters due to the second calcination step [136]. For both catalysts, the surface area and pore volume are reduced compared to pure γ-alumina, suggesting that the metal species filled and plugged the support pores with partial collapse and deterioration after impregnation and calcination [130], [137]. The detailed textural properties of samples, mesoporous γ-alumina, NiMo, and CoMo are summarized in Table 3.2.

Table 3.2. Properties of calcined mesoporous alumina and supported NiMo, and CoMo catalysts.

Samples	S_{BET} (m^2/g)	S_{DFT} (m^2/g)	V_t (cm^3/g)	V_{DFT} (cm^3/g)	W_{BJH} (nm)	W_{DFT} (nm)
Mesoporous γ-alumina	259	283	0.506	0.488	7.8	6.1
NiMo	182	171	0.457	0.427	10.0	8.2
CoMo	188	187	0.508	0.487	10.8	8.2

Specific surface area (S_{BET}) is calculated from adsorption data in the relative pressure range of 0.05 to 0.2. Single point pore volume (V_t) calculated from the adsorption isotherm at the relative pressure of 0.99. Barrett-Joyner-Halenda (BJH) method is applied to calculate pore width at the maximum of the PSD using adsorption branch. The kernel of NLDFT equilibrium capillary condensation isotherms of N_2 at 77K on silica is used to calculate S_{DFT} (specific surface area), V_{DFT} (total pore volume) and W_{DFT} (pore diameter).

3.3.2 X-ray diffraction (XRD)

The XRD patterns of the synthesized γ-alumina and the calcined bimetallic catalysts, NiMo and CoMo, are shown in Figure 3.3. The two typical diffraction peaks (400) and (440) that are respectively located at $2\theta = 46$ and 67° are the ones indexed to γ-Al_2O_3 phase with a cubic structure (unit cell parameter: a, b and c are equal to 0.790 nm) (JCPDS card No. 10-0425). Due to the fine nature of nano-sized crystalline domains along with a few imperfection, a high degree of broadness is acquired in all diffraction peaks. Neither nickel and cobalt oxide nor molybdenum oxide corresponding phases diffraction peaks is legible which results in the similarity of the XRD patterns of alumina and the catalysts. Their broad diffraction peaks confirm the presence of small alumina crystalline domains. This suggests that even at the

high metal loading of this study, the metal oxides being not XRD visible, are therefore well dispersed at nano-size scale on the support. This could be due to the promoting effect of nickel and cobalt which is also in good agreement with TEM images (see Figure 3.7e, f, g, and h). The roughly estimated mean crystallite size of the samples are listed in Table 3.3 (calculated using Scherrer equation from the full-width half-maximum of the isolated (400) and (440) diffraction peaks). It is suggested that the incorporation of metal species leads to a slight increase in crystal size. It can also be proposed that the second calcination (with 3 h soaking time) can affect the crystalline domain size [136]. Moreover, the estimated average crystal domain size (Table 3.3) increases after metal loading, which is more noticeable for the nickel catalyst than the cobalt catalyst.

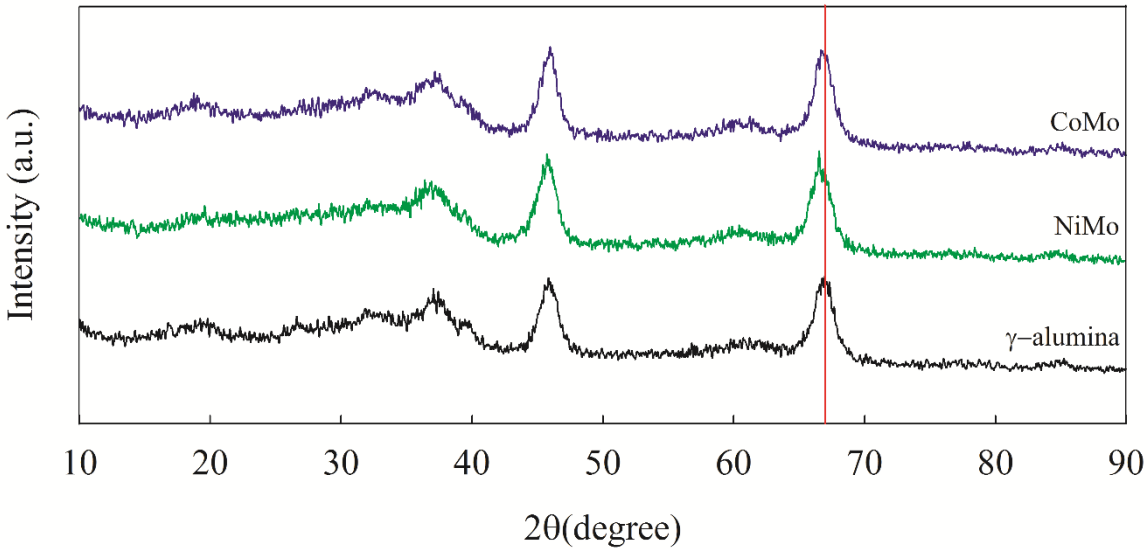

Figure 3.3. X-ray diffraction patterns γ-alumina and impregnated catalysts.

Table 3.3. Average γ-alumina crystal domain size of samples.

Sample	Lattice parameter (α)	Crystal size (nm)
Mesoporous γ-alumina	7.9054	6.61
NiMo	7.9272	7.46
CoMo	7.9063	6.89

In the incipient wetness co-impregnation applied in this study, no significant incorporation of the active metals at the atomic level, to the mesoporous γ-alumina framework is expected, as these are assumed to be present on the channel walls of mesoporous alumina [62]. The impregnation of active metals in the alumina resulted, however, in a slight change in the calculated lattice parameter of the catalysts (see Table 3.3). The nickel/cobalt loading seems to be associated with the incorporation of Ni^{2+} or Co^{2+} in small quantity, in the alumina lattice. The incorporation of nickel in the alumina results in a slight increase in the lattice parameter compared to pure alumina, but in the cobalt case, little change in alumina's lattice parameter is observed. A shift to smaller diffraction angles in the position of the (440) diffraction peak of alumina is observed in the presence of Ni, but for cobalt catalyst, this displacement was barely detectable. A similar result is also reported in other work [138]. The ionic radii of the metal ions follow the sequence of Co^{2+} (88.5 pm) > Ni^{2+} (83 pm) > Al^{3+} (68 pm) [139], [140]. Thus the Ni^{2+} ion is more likely to be inserted into the alumina lattice than Co^{2+}.

3.3.3 Chemical mapping analysis

The spatial distribution of metal atoms was illustrated using an electron probe microanalyzer (EPMA). As can be seen in Figure 3.4, cracks are visible on the surface of both catalysts; while Ni/Co, Mo, and S are distributed on the γ-alumina support after calcination and subsequent sulfidation. All the metals and sulfur are uniformly dispersed on the alumina substrate, and no obvious metal species aggregation is detected at the spatial resolution of the instrument (1 μm).

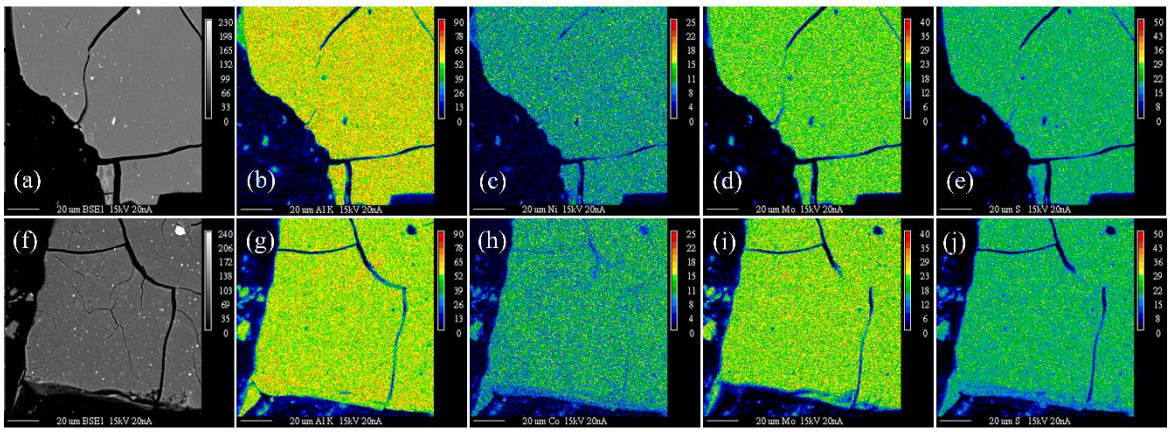

Figure 3.4. BSE micrograph and EPMA maps of NiMo (up) and CoMo (down) by electron microprobe; (a) and (f) are backscattered SEM images, (b, g), (c), (h), (d, i) and (e, j) are the maps of Al, Ni, Co, Mo, and S, respectively.

3.3.4 X-ray photoelectron spectroscopy (XPS)

XPS was used to determine the chemical state of the species and the atomic ratio of elements near the surface layer of the catalysts. The Ni2p (NiMo and NiMo-S) and Co2p (CoMo and CoMo-S) spectra are depicted in Figure 3.5. The observed binding energies for Ni2p3/2 and Ni2p1/2 in the NiMo catalyst are approximately 856.2±0.1 and 873.8±0.1 eV, respectively, both being ascribed to Ni^{2+} species. The absence of any peaks below 856.2±0.1 eV along with the position of the strong shake-up satellite peaks centered approximately at 862.6±0.1 and 880.7±0.1 eV, proves that the NiO phase is not present on the surface of the catalyst and the Ni^{2+} species may consist of $NiMoO_4$ or $NiAl_2O_4$ [141]. After sulfidation, two additional peaks around 854.6±0.1 and 871.2±0.1 eV appear in the Ni2p spectrum (see Figure 3.5), which are possibly attributed to the formation of Ni-Mo-S phase. The absence of peak below 853.8±0.1 eV shows that no NiS_x phase, which might be NiS, Ni_2S_3, or Ni_9S_8 is formed during sulfidation. In a previous work, two peaks positioned at binding energies of 856.3 and 873.9±0.1 eV, coupled with the fact that no NiO species were found in the XPS spectrum of NiMo, was sometimes attributed to $Ni(OH)_2$ [142]. The Co2p3/2 and Co2p1/2 main peaks with their corresponding shake-up satellite peaks in CoMo and CoMo-S catalysts are also

presented in Figure 3.5. In CoMo, the lines of Co2p3/2 and Co2p1/2 are located at binding energies of approximately 781.4±0.1 and 797.2±0.1 eV, respectively. The Co2p3/2 peak coupled with a rather strong shake-up satellite peak (3d to 4s) at a higher binding energy of approximately 786.0±0.1 eV combined with the lack of a peak around 791±0.1 eV (characteristic of Co^{3+}) revealed the presence of cobalt oxide only under the Co^{2+} form [143]. After sulfidation, new lines appeared in the XPS spectra. The peaks centered at around 778.9±0.1 and 793.7±0.1 eV are associated with the formation of CoMo-S phase. The lack of peak at 778.0±0.1 eV shows that Co_9S_8 species are not present on the surface of CoMo-S catalyst [133], [144].

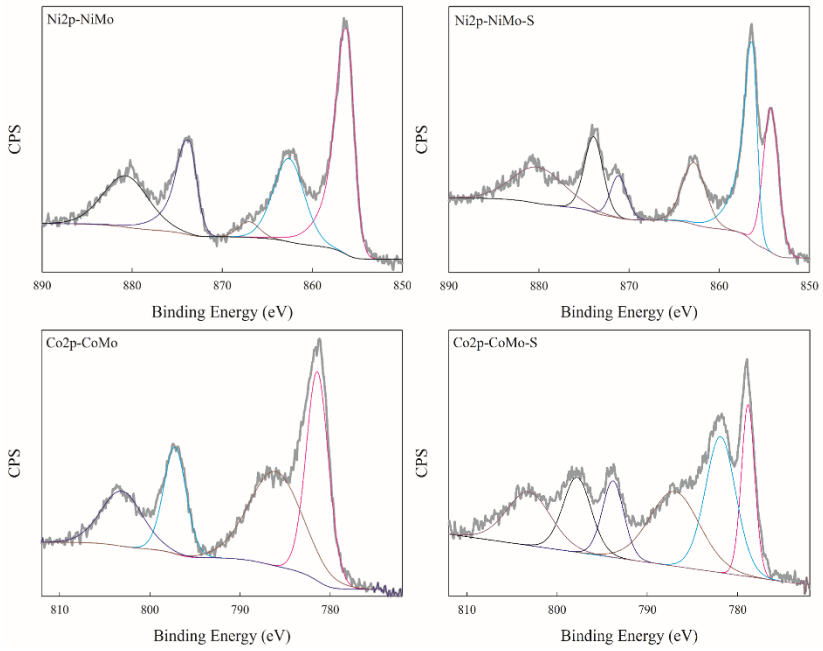

Figure 3.5. XPS spectra of Ni2p and Co2p of catalysts in oxidic and sulfided forms.

The XPS spectra of Mo3d in the oxidic and sulfided form for both nickel and cobalt catalysts are presented in Figure 3.6. Different types of molybdenum ions such as Mo^{4+} (sulfide), Mo^{5+} (oxysulfide), and Mo^{6+} (oxide) may be present in the samples [143]. As can be seen, in the Mo3d spectra of NiMo and CoMo the two main peaks centered at 232.8±0.1 and 236.0±0.1 eV, respectively corresponding to Mo3d5/2 and Mo3d3/2, can be attributed to the presence

of Mo^{6+} species. The Mo3d spectrum of sample NiMo-S shows additional peaks at the binding energies of 229.3±0.1 and 232.9±0.1 eV which are respectively attributed to Mo^{4+} and Mo^{6+}. A minor peak positioned at a binding energy of 230.5±0.1 eV is attributed to Mo^{5+}. Another peak is also visible at 226.4±0.1 eV which is ascribed to S^{2-} [145], [146]. Mo3d XPS spectra of CoMo and CoMo-S resemble those of nickel catalyst regarding their types of molybdenum species and corresponding binding energies. A minor shoulder at approximatively 228±0.4 eV manifesting on XPS spectra of CoMo-S could possibly be ascribed to a minor amount of MoOx or MoS_2 [147] .

As illustrated in the XPS spectra of S2p for sulfided nickel and cobalt catalysts, the peaks at 162.2±0.1 and 162.4± eV both revealed the presence of S^{2-}. Peaks at 163.4±1 eV present in both NiMo-S and CoMo-S spectra are attributed to S_2^{2-}, and the wide peaks in the range of 169.0±1 to 169.4±1 eV belong to S^{6+} in SO_4^{2-}, in both NiMo-S and CoMo-S [146], [148]. This surface oxidation is likely produced when contacting with air during sample transportation to the XPS instrument. The surface atomic ratio obtained from XPS analysis and the bulk theoretical values for all samples are presented in Table 3.4.

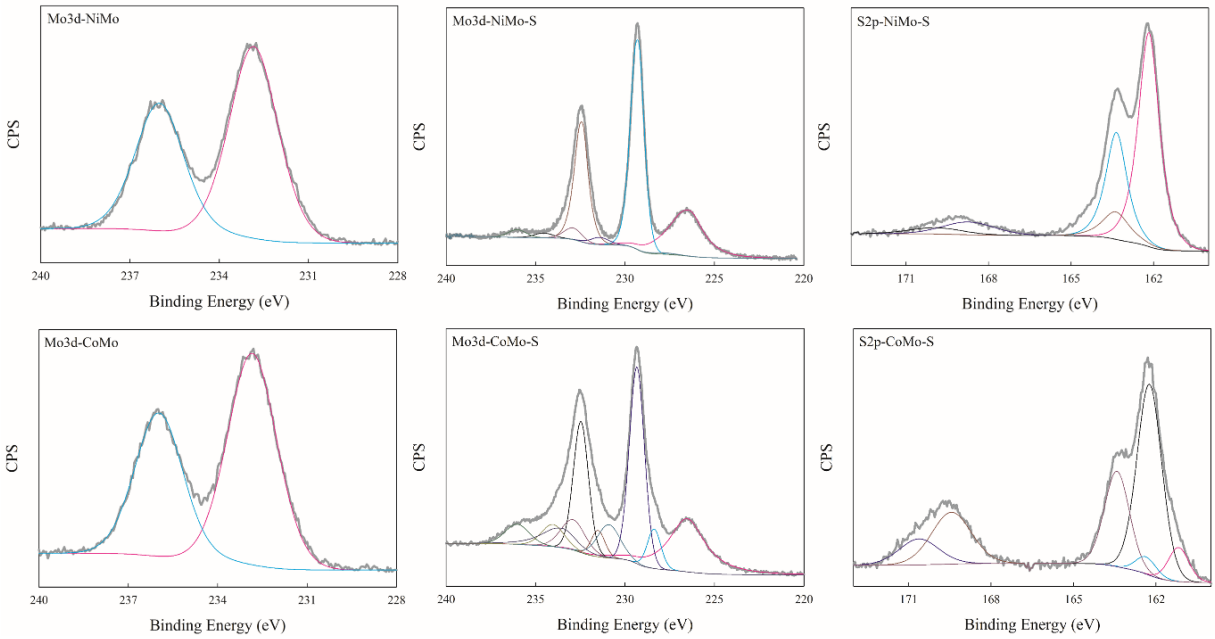

Figure 3.6. spectra of Mo3d (oxidic and sulfided) and S2p spectra of catalysts.

Table 3.4. Atomic ratio values of the catalysts: experimental from (XPS) and bulk calculated material composition.

Sample	Ni/Al		Co/Al		Mo/Al		S/Al
	XPS	bulk	XPS	bulk	XPS	bulk	XPS
NiMo	0.046	0.054	NA		0.132	0.209	NA
NiMo-S	0.043	NA	NA		0.263	NA	0.311
CoMo	NA		0.053	0.054	0.175	0.209	NA
CoMo-S	NA		0.048	NA	0.149	NA	0.207

Comparing the ratio of Ni/Al and Co/Al in the non-sulfided catalyst revealed that Ni species are surface depleted in the γ-alumina particles whereas no such an effect is observed for Co species. Mo/Al ratio for both catalysts show significant surface depletion of Mo. This effect is more pronounced in NiMo than CoMo. These results determine that when using nickel as a promoter, both active metal atoms are more concentrated inside the alumina bulk phase compared to cobalt catalyst.

The S/Al ratio was found higher in NiMo-S than in CoMo-S and similar differences were observed for Mo/Al, whereas Ni/Al and Co/Al were almost the same (within 10%). This suggests that sulfur is more closely associated with molybdenum than either Co or Ni. The change in Ni/Al and Co/Al upon sulfidation is also minor compared to Mo/Al which increases in the Ni catalyst but decreases for Co one. This may indicate a difference in the effect of the promoter in stabilizing Mo during sulfidation.

Table 3.5 shows the distributions of the various species of each element based on the respective surface areas of the deconvoluted XPS lines. In the Mo species, it is found that the fraction of Mo^{6+} is commensurate with that of SO_4^{2-} in the sulfur line. This also suggests that the oxidic Mo^{6+} is also associated with incidental oxidation. The higher $Mo^{4+/}$ Mo^{5+} ratio in the NiMo-S compared to CoMo-S suggests that the former catalyst is more sulfided, since Mo^{5+} is usually associated to oxysulfide. It may thus be expected to be more active as HDO catalyst.

Table 3.5. Percentages of each species (XPS) calculated from the deconvolution of Ni2p, Co2p, and Mo3d lines.

Sample	Ni^{2+}	NiMo-S	Co^{2+}	CoMo-S	Mo^{4+}	Mo^{5+}	Mo^{6+}	S^{2-}/ S_2^{2-}	SO_4^{2-}
NiMo	100	0	NA	NA	0	0	100	0	0
NiMo-S	73.0	27.0	NA	NA	89.1	4.3	6.6	89.8	10.2
CoMo	NA	NA	100	0	0	0	100	0	0
CoMo-S	NA	NA	77.1	22.9	70.3	15.1	14.6	72.7	27.3

3.3.5 Transmission electron microscopy (TEM)

TEM micrographs of the synthesized mesostructured wormhole-like γ-alumina and the oxidic NiMo and CoMo catalysts are shown in Figure 3.7. The TEM images of γ-alumina (Figure 3.7a, b, c, and d) demonstrate the formation of a mesoporous structure due to the high degree of hydrogen bonding and long-chain molecules of the polymeric template [108]. The mesostructure is detectable in the TEM pictures of both catalysts confirming that active metals are homogeneously filled and dispersed on the mesoporous structure (Figure 3.7e, f, g, and h). These observations are in accordance with XRD (Figure 3.3) and chemical mapping analysis (Figure 3.4) results.

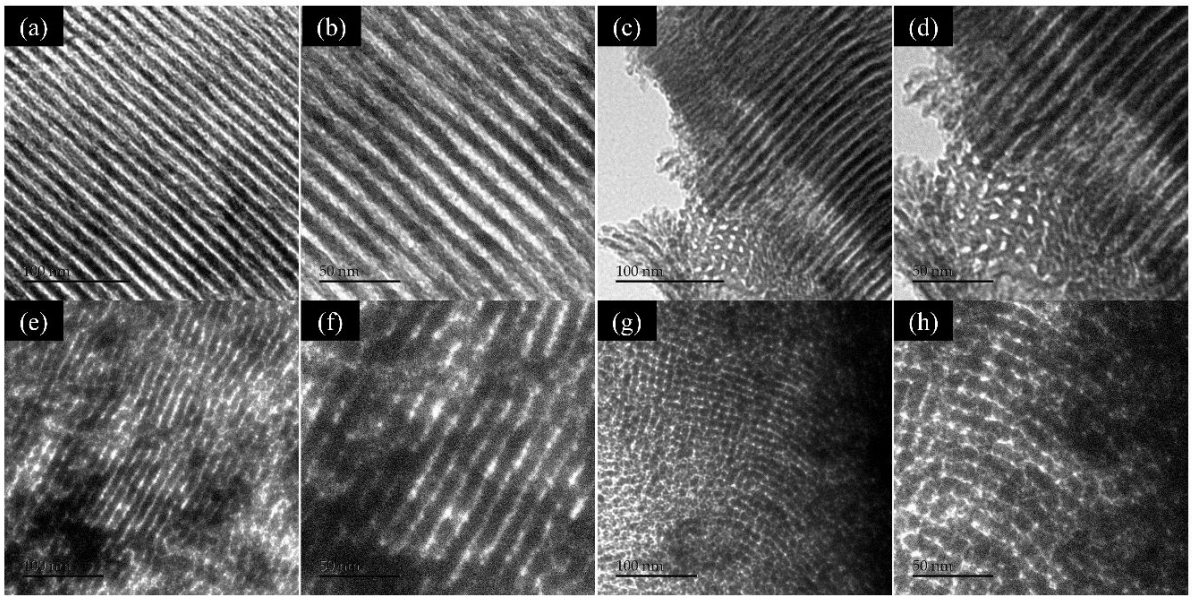

Figure 3.7. (Up) TEM images of mesoporous γ-alumina (a, b, c, d) and (down) oxidic catalysts: NiMo (e, f) and CoMo (g, h). View along 110 direction at two magnifications.

3.3.6 Catalytic activity

3.3.6.1 Fourier transform infrared spectroscopy (FTIR)

To evaluate the efficiency of the synthesized catalysts, liquid samples of canola oil hydrotreated at different process temperatures were collected. Figures 3.8 and 3.9 present the IR spectra of the products obtained at different LHSV of 1, 2 and 3 h^{-1} under the reaction conditions of T = 350°C, P = 450 psi and H_2/oil = 600 $mLmL^{-1}$ over NiMo-S and CoMo-S catalysts, respectively. The IR spectrum of canola oil is presented for comparison.

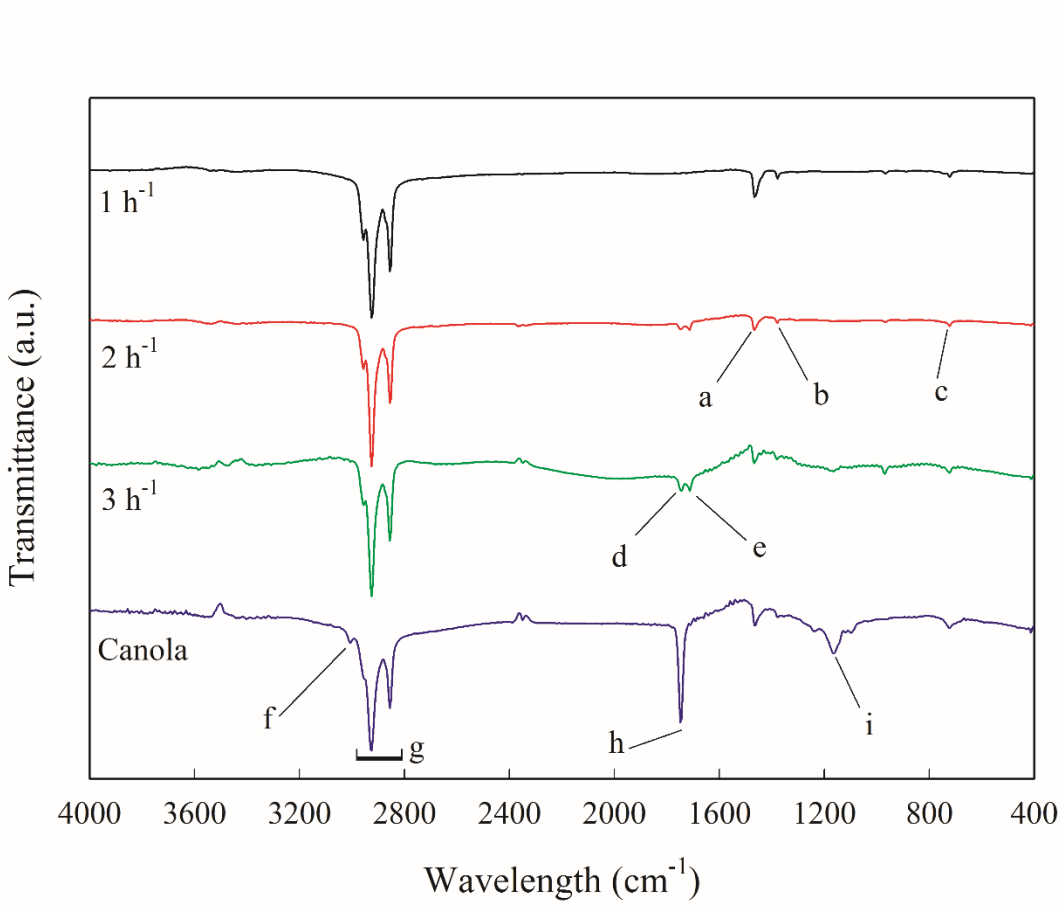

Figure 3.8. FTIR spectra of hydrotreated canola oil over NiMo-S at various LHSV, T = 350°C, P = 450 psi, and H_2/oil = 600 $mLmL^{-1}$; a: $-CH_2$, b: CH_3, c: $-(CH_2)-_n$, d/h: Ester C=O, e: Acid C=O, f: Alkene =C-H, g: C-H groups and i: Ester C-O-C.

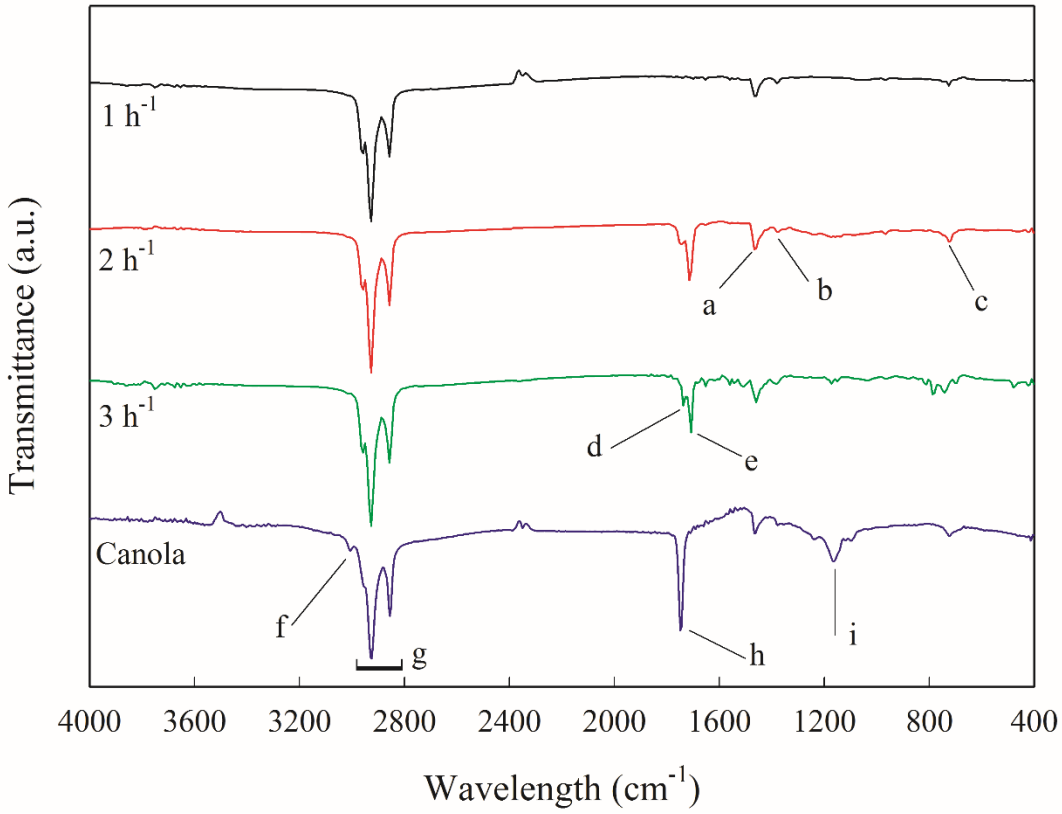

Figure 3.9. FTIR spectra of hydrotreated Canola oil over CoMo-S at various LHSV, T = 350°C, P = 450 psi, and H_2/oil = 600 mLmL^{-1}; a: -CH_2, b: CH_3, c: -$(CH_2)_n$-, d/h: Ester C=O, e: Acid C=O, f: Alkene =C-H, g: C-H groups and i: Ester C-O-C.

Canola oil showed absorbance bands at 1170 cm^{-1} (ester C-O-C), 1742 cm^{-1} (ester C=O), and above 3000 cm^{-1} (alkene =C-H) as characteristic of triglycerides. As presented, in both catalysts at LHSV = 3 h^{-1} the sharp peak centered at 1742 cm^{-1}, representing ester groups in Canola oil, is weakened and shifted to 1711 cm^{-1} belonging to C=O groups of fatty acids [149]. Moreover, the peak centered at 1170 cm^{-1} also decreased. This peak had much lower intensity at higher LHSV (3 h^{-1}) for NiMo-S compared to CoMo-S, showing the higher activity of this catalyst at lower contact time with the reactant. At 2 h^{-1} LHSV, this superiority is kept for NiMo-S. For both catalysts the bands at 722 cm^{-1} and 1300 to 1475 cm^{-1} belonging to -$(CH_2)_n$, and to (-CH_2) and (-CH_3) groups are apparent. Finally, at LHSV = 1h^{-1} both catalysts lead to the formation of alkanes, and all peaks belonging to oxygenates are removed.

The peaks centered at the region of 2800 to 3000 cm^{-1} (C-H groups) are present in both canola oil and hydrotreated product; the only differences are the disappearance of the peaks above 3000 cm^{-1} belonging to alkene (=C-H) groups. These results show that the final obtained products are saturated alkanes [83]. They also indicate that NiMo-S exhibits higher glyceride conversion at lower contact time. Temperature is one of the main parameters in the hydrotreatment process; it can influence the composition of the final product. Due to the fast triglyceride conversion over NiMo-S at the studied process conditions, it was not possible to carefully determine the differences in the IR spectra in the temperature range of 300 to 350°C and LHSV = 1 h^{-1}. That is why, only the FTIR spectra of CoMo-S catalyst at different temperatures of 300, 325, and 350°C and reaction conditions of, LHSV = 1 h^{-1}, P = 450 psi, and H_2/oil = 600 $mLmL^{-1}$ are presented in Figure 3.10. As can be observed in Figure 3.10, the minimum temperature of 350°C is necessary for the complete conversion to normal alkanes.

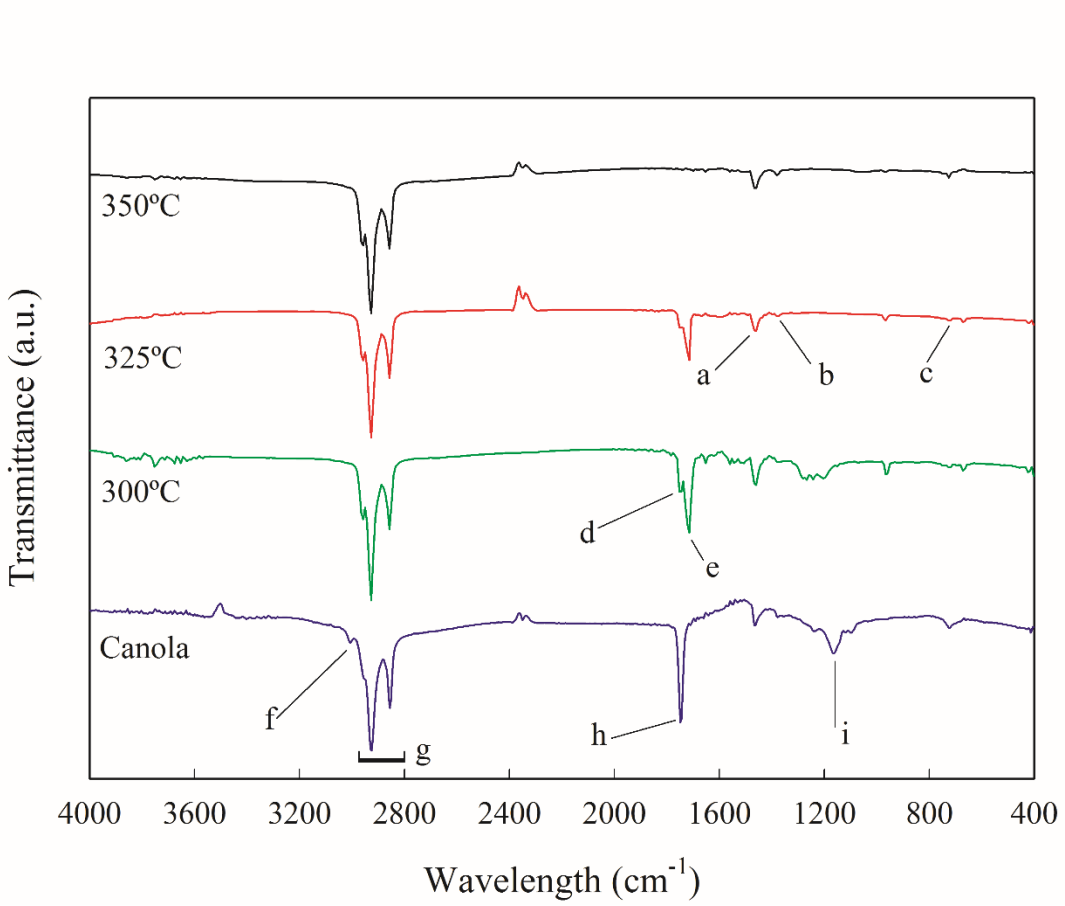

Figure 3.10. FTIR spectra of hydrotreated canola oil over CoMo-S at various temperatures, LHSV = 1 h^{-1}, P = 450 psi and H_2/oil = 600 $mLmL^{-1}$; a: -CH_2, b: CH_3, c: -(CH_2)-$_n$, d/h: Ester C=O, e: Acid C=O, f: Alkene =C-H, g: C-H groups and i: Ester C-O-C.

3.3.6.2 HPLC analysis of the hydrotreated oil

HPLC chromatograms, recorded at different conversions, are presented in Figure 3.11. Triglyceride conversions were calculated by using quantified values of peaks surface area with high accuracy ±1% [75].

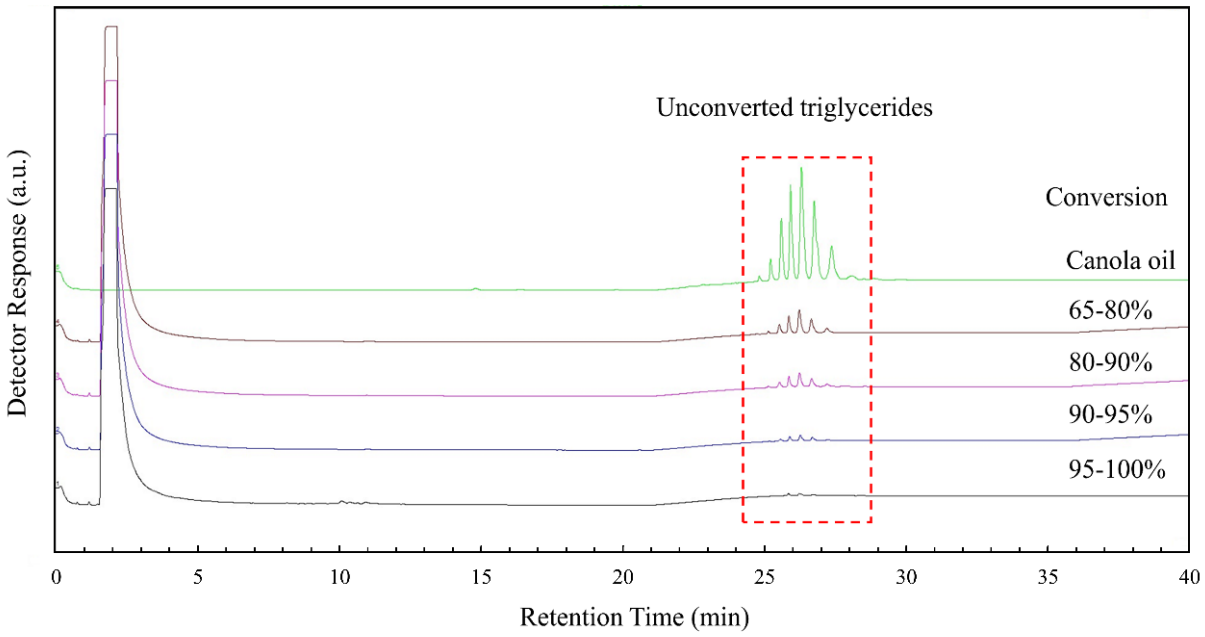

Figure 3.11. Representative HPLC chromatograms of Canola oil, and hydrotreated products at various triglyceride conversion ranges.

The conversion of triglycerides to the final liquid products is presented in Figure 3.12. The liquid conversions obtained over NiMo-S are higher than those on CoMo-S over the temperature range of 325 to 375°C. At 400°C the conversion reached 100% for both catalysts.

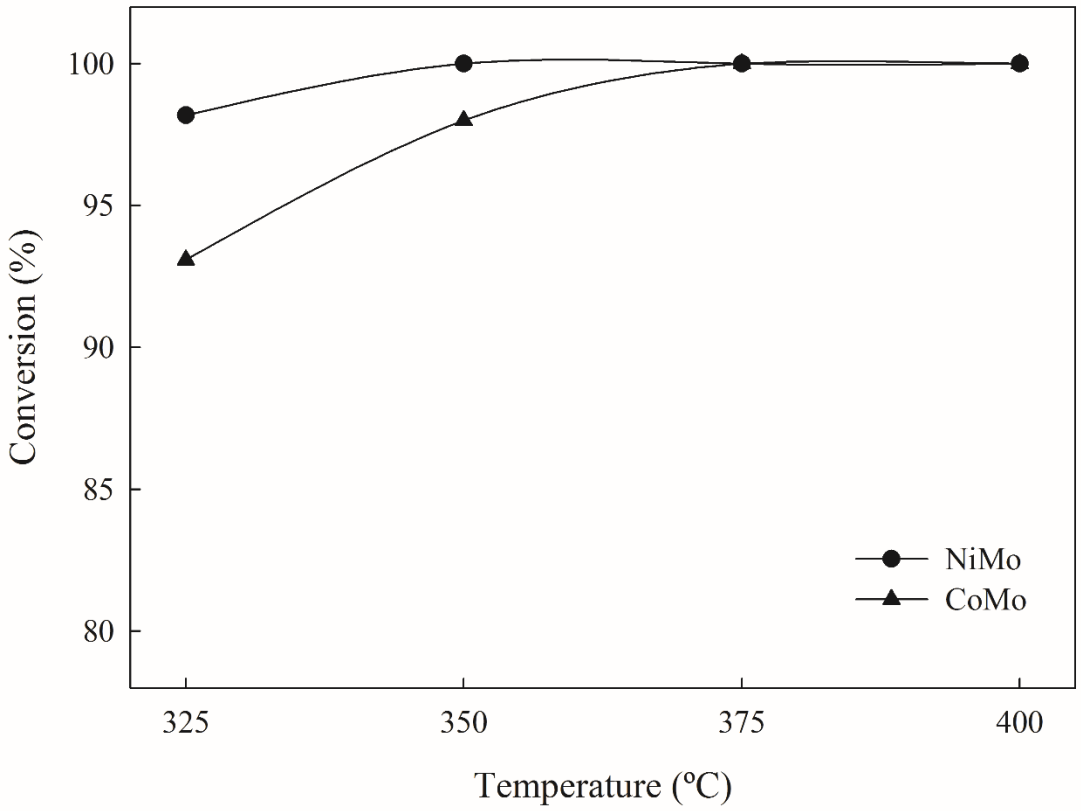

Figure 3.12. Conversion of triglycerides over NiMo-S and CoMo-S at different temperatures, LHSV = 1 h^{-1}, P = 450 psi and H_2/oil = 600 $mLmL^{-1}$.

3.3.6.3 GC-MS analysis of the hydrotreated oil

In the presence of metal-loaded γ-alumina, hydrocracking takes place along with the different hydrocarbon producing reactions. The extent of hydrocracking reaction depends on the loaded active metals and their concentrations. The hydrocracking process converts higher molecular weight molecules into lower molecular weight ones by simultaneous or subsequent hydrogenation and carbon bond breakage. Catalysts have a dual function which are hydrogenation-dehydrogenation and cracking [150]. Hydrocarbon composition of the hydrotreated products was analyzed with GC-MS. The final detected products consist mainly of n-alkanes with carbon chain lengths ranging from C9 to C30, with the majority of n-alkanes with carbon atom number in the range of C15 to C18 and maximum of C18 chain length. The triglyceride molecules of the feedstock indeed consist of 98.1% of the fatty acid

molecules with chain lengths of C16 and C18 with the maximum frequency of C18 (see Table 3.1).

Decarbonylation (DCO) and decarboxylation (DCO_2) reaction pathways lead to the formation of n-alkanes with an odd number of carbon atoms chain length, whereas hydrodeoxygenation (HDO) reaction pathways result in products with an even number of carbon atoms chain lengths [53]. Thus the ratio of C16/C15 or C18/C17, respectively derived from C16 and C18 chains in the triglycerides constitutive fatty acids, are indicative of selectivity ratios of HDO with respect to DCO+DCO_2. These are plotted as a function of reaction temperature in Figure 3.13. Both catalysts favor the hydrodeoxygenation reaction pathway over the temperature range of 325 to 400°C.

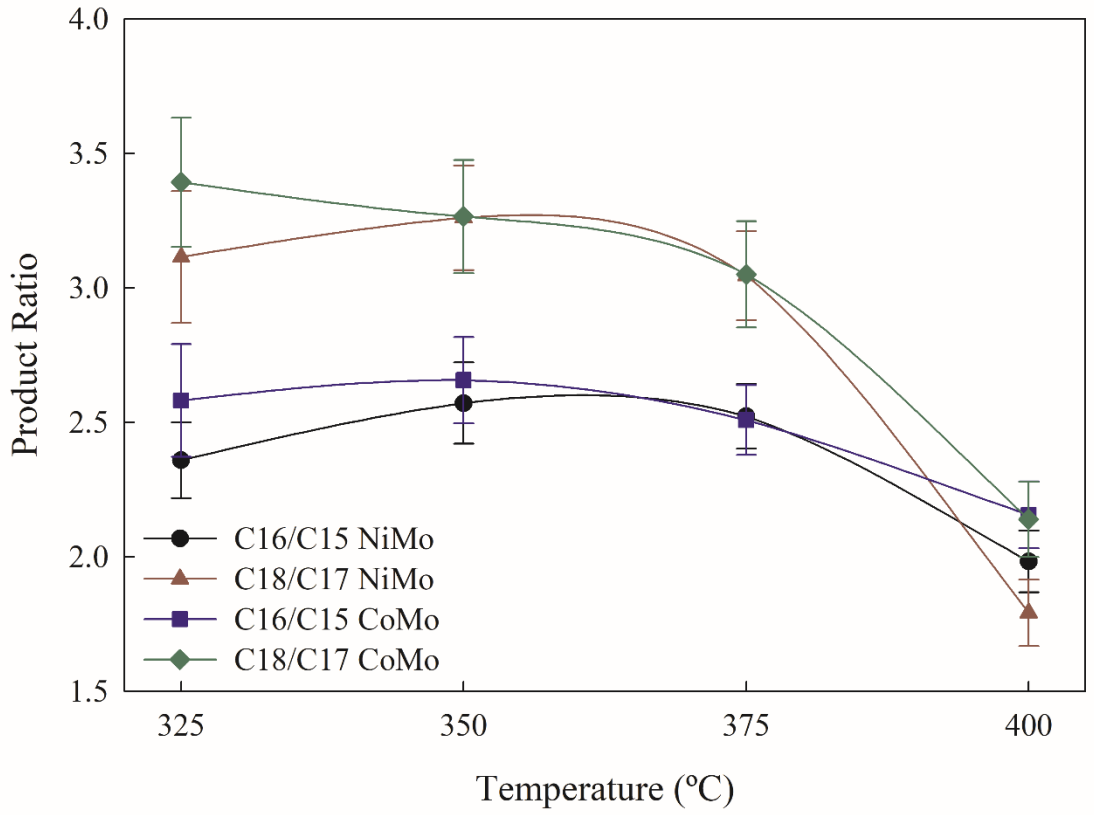

Figure 3.13. HDO/(DCO+DCO_2) selectivity ratios for NiMo-S and CoMo-S at different temperatures, LHSV = 1 h^{-1}, P = 450 psi and H_2/oil = 600 $mLmL^{-1}$.

The evolution of the chain length distribution with the reaction temperature for the two catalysts is reported in Figure 3.14.

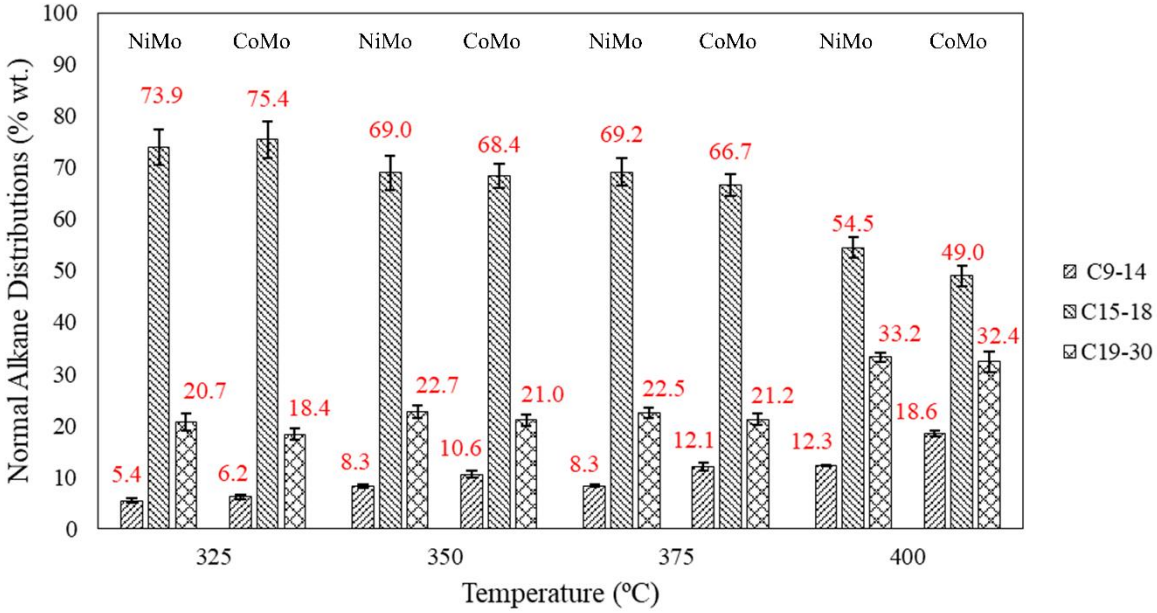

Figure 3.14. Normal alkane distributions of liquid products over NiMo-S and CoMo-S catalysts at different temperatures, LHSV = 1 h^{-1}, P = 450 psi and H_2/oil = 600 $mLmL^{-1}$.

The distribution of hydrocarbon chain length in the liquid products over both catalysts are presented as three fractions with chain lengths: C9 to C14 considered as hydrocracked light molecules, C15 to C18 as the desired paraffin products and C19 to C30 as the oligomerized heavy fraction. The formation of light molecules is due to hydrocracking while the formation of heavier molecules is caused by the oligomerization reactions [151].

The results in Figure 3.14 indicate that the two catalysts behave in a similar fashion while increasing temperature. The fraction of C15-C18 in the liquid products is higher at 325ºC and decreases progressively with temperature over the two catalysts. Increasing temperature favors both hydrocracking and oligomerization reactions. Both are catalyzed by acid sites usually found at the alumina support which would explain the similar behavior of NiMo-S and CoMo-S. From Figure 3.14, it may also be noted that all fractions of C9-C14 obtained at

the four temperatures are slightly lower for NiMo than CoMo sulfided catalysts. The opposite trend is observed for C19-C30 components. This suggests that the two kinds of reactions (hydrocracking and oligomerization) are not activated by the same acid sites, with the oligomerization sites being of higher surface density on CoMo catalyst.

Similarly, the results in Figure 3.13 show that both catalysts also display comparable behavior with higher selectivity to HDO than to DCO-DCO_2. The effect of increasing temperature on their selectivity is also quite the same. Figure 3.12, obtained from HPLC results similar to those reported in Figure 3.11, illustrates the high triglyceride conversion obtained above 325ºC with the two catalysts. As illustrated by the FTIR results shown in Figure 3.10, the converted products are mostly hydrocarbons at this temperature, since only a minor residual ester C=O line (1742 cm^{-1}) is observed over the sulfided CoMo-S catalyst. This minor peak is not present in the spectrum of the liquid produced with the same conditions over NiMo-S (not shown). Since the total conversion is also higher on the latter (Figure 3.12). It seems that the NiMo-S catalyst has a slight advantage over CoMo-S.

3.4 Conclusion

In this study, the polymeric template assisted sol-gel method via evaporation-induced self-assembly (EISA) process was employed for catalysts support preparation. A wormhole-like mesostructured nanoporous γ-alumina with pores in the range of 8 nm and nano-sized crystalline domains was synthesized. By applying incipient wetness co-impregnation followed by a second calcination step, the active metals were homogeneously impregnated and nanodispersed on the support. A comparison was made between sulfided NiMo and CoMo catalysts supported on mesostructured γ-alumina with the composition of (15% wt. MoO_3 and 3% wt. NiO or CoO). These catalysts were tested in the continuous hydrotreatment of vegetable oil (canola) yielding diesel range liquid hydrocarbons (C15-C18) in a high yield. The effects of LHSV and temperature were investigated over the ranges of 1 to 3 h^{-1} and 325 to 400ºC at constant pressure of 450 psi and H_2/Oil of 600 $mLmL^{-1}$. Both catalysts showed satisfactory catalytic properties with some minor advantages in terms of reaction rate and selectivity to green diesel production, observed in NiMo-S/γ-alumina catalyst.

Acknowledgements

We acknowledge Dr. Alain Adnot from the Chemical Engineering Department at Laval University for his constructive comments and help on XPS analysis. The financial support of Natural Science and Engineering Council of Canada (NSERC, Grant numbers: STPGP 396579 and RGPIN-2015-06175) is gratefully acknowledged.

Chapter 4

Hydrodeoxygenation over reduced mesostructured Ni/γ-alumina catalysts prepared via one-pot sol-gel route for green diesel production

Arsia Afshar Taromi and Serge Kaliaguine, Applied Catalysis A Journal, Under revision, 2017.

Résumé

Des catalyseurs Ni/alumine-γ mésostructurés non sulfurés écologiques ont été synthétisés et développés pour produire du diesel vert à partir de l'huile de canola. Les catalyseurs ont été préparés soit par la voie sol-gel en une étape (SG) accompagnée d'un auto-assemblage induit par évaporation (EISA), soit par imprégnation par voie humide (incipient wetness impregnation, IMP). Ils ont été caractérisés par l'analyse des isothermes d'adsorption-désorption de l'azote, XRD, XPS et TEM. En raison de l'incorporation du nickel dans le réseau mésostructuré, les espèces d'oxyde de nickel sont en plus faibles concentrations dans le cœur du solide pour les catalyseurs SG comparativement aux IMP. La formation de nickel métallique actif a été confirmée après pré-réduction in situ dans H_2 pour les catalyseurs SG et IMP. L'hydrotraitement continu de l'huile de canola a été effectué dans un réacteur à lit fixe à écoulement descendant, et les hydrocarbures liquides produits contiennent principalement des n-alcanes C15-C18. Le catalyseur SG présentait une meilleure stabilité jusqu'à 10 h de temps en ligne (TOS). Le catalyseur IMP a initialement montré une conversion plus élevée que SG jusqu'à TOS: 300 min; il a ensuite diminué nettement à des valeurs inférieures à celles de SG.

Abstract

Environmentally friendly non-sulfided mesostructured Ni/γ-alumina catalysts were synthesized and developed to produce green diesel from canola oil. The catalysts were prepared either by a one-pot sol-gel (SG) via evaporation-induced self-assembly (EISA) or by incipient wetness impregnation (IMP). They were characterized by N_2 adsorption-desorption, XRD, XPS, and TEM. Due to the incorporation of nickel in the mesostructured framework, bulk nickel oxide species are lower for SG catalysts compared to IMP ones. Formation of active metallic nickel was confirmed after in-situ pre-reduction in H_2 for both SG and IMP catalysts. Continuous hydrotreatment of canola oil was performed in a down-flow fixed-bed reactor, and the liquid hydrocarbon products mainly contained C15-C18 n-alkanes. SG catalyst exhibited a better stability up to 10 h of time on stream (TOS). The IMP catalyst initially showed higher conversion than SG up to TOS: 300 min; it thereafter decreased sharply to values lower than those of SG.

4.1 Introduction

Fossil fuels are currently the essential source of energy. These exhausting sources of energy increase greenhouse gas (GHG) emission, particularly carbon dioxide, and consequently lead to global warming. Since the energy demand is steadily growing; many research studies have focussed on finding some alternative sustainable energy sources [137], [152]. Among all types of renewable energy sources such as hydropower, solar power, wind power and fuel cells; the only one that is capable of producing stored energy in the form of material is biomass. Noticeably, it does not contribute to GHG emission owing to its carbon-neutrality. Moreover, biomass-derived products, which might be in solid, liquid, or gas form, could be directly used as fuel or as raw materials to produce downstream valueadded products such as bio-based polymers and chemicals. The use of biomass can also create employment in different geographical sectors for local residents, strengthening the economy, reducing the rural to urban area migration and increasing the national energy security [121], [122], [153].

Among the constituents of biomass that can be used as a raw material to make green liquid fuels are triglycerides. The primary feedstock sources of triglycerides are plants, waste cooking derived oils, animal fats and algae [15], [123]–[126], [154]. A recently developed method for producing pure green diesel is the catalytic deoxygenation of bio-derived triglyceride molecules via hydrotreatment process. The hydrotreated products mainly consist of a mixture of n-alkanes with carbon numbers in the range of that of diesel hydrocarbons. In this process, first, all C=C bonds are saturated in the presence of hydrogen, followed by removal of oxygen molecules. The removal of the oxygen could mainly take place via three different reaction pathways involving: hydrodeoxygenation (HDO), decarbonylation (DCO) and decarboxylation (DCO_2) removing oxygen in the form of H_2O, H_2O/CO, and CO_2, respectively. The hydrotreating reaction can go through HDO or DCO-DCO_2 pathways. In the former, the final product will consist of molecules with the same carbon number as the corresponding fatty acids present in the triglycerides molecules, while in the latter the carbon number of the product molecules will be one less. The hydrogen consumption trend through these patterns follows the sequence of HDO > DCO > DCO_2 leading to HDO being the dominant pathway under high H_2 pressure. This causes particular economic interest to find

suitable process conditions and prominent catalysts favoring the latter two pathways [12], [155].

Two groups of metals; precious noble metals (Pt and Pd) and promoted transition metals (NiMo, CoMo, etc.) loaded on different supports such as γ-alumina, zeolites, and activated carbons were used as catalysts for the hydrotreatment of triglycerides [29], [50], [70], [72], [136], [156], [157].

The main drawbacks of noble metals to be used in the catalysts include high cost and difficult accessibility (the cost of Pt/Pd is around 3223/3015 times and 497/465 times higher than Ni and Co, respectively) [158]. On the other hand, transition metals are used in their sulfided form, and it is required to maintain their sulfided form along the reaction. This can be done by introducing sulfur bearing agents in the feed. The leaching of sulfur from catalysts is harmful to human health and gives rise to environmental pollution. Also, sulfur causes infrastructure damage and trace contamination of the products [44]. These disadvantages have led to a considerable interest to find non-sulfided efficient catalysts for triglyceride hydrotreating. Textural properties of the catalysts such as specific surface area, pore size, pore volume and metal species crystallite domain size, significantly affect the catalytic efficiency. High surface area and large pore diameter enhance the catalytic activity in hydrotreatment of triglycerides. The pores diameter of the catalyst should be large enough to allow the large triglyceride molecules (the size of a triglyceride molecule is estimated to be 15-25 Å) to easily enter the pores and reach the active sites of the catalyst [48], [49]. The high-cost zeolite supports have small pore diameters which is not desired when the reactants are bulky molecules such as triglycerides. Also, the high acidity of these supports leads to an increase in the yield of lighter products as a consequence of enhanced cracking [50]. Hydrotreatment of triglycerides tends to the accumulation of coke on the surface of the catalysts. When carbon is used as a support, in most of the cases, it is not possible to regenerate the catalysts via economic air combustion and reuse the catalysts [51], [159]. Mesoporous γ-alumina with tunable textural properties, mild acidity, and high thermal stability could be a good candidate to be used as support for the diesel-like hydrocarbons production via hydrotreatment [74].

Gousi et al., have recently explored the usefulness of the co-precipitated monometallic Ni/alumina in reduced form, on the deoxygenation of sunflower oil. They used a semi-batch reactor with reaction conditions set at H_2 pressure of 40 bar, and a temperature of 310ºC. The final product that was obtained under such conditions mainly consisted of n-C15 to n-C18 [71]. Hachemi et al., employed the wetness impregnation method using nickel salt and commercial γ-alumina to synthesize 5% wt. Ni/γ-Al_2O_3. They demonstrated a high selectivity to C17 hydrocarbons over Ni/γ-Al_2O_3 in the hydrotreatment of stearic acid as a model compound in a semi-batch system [72]. Li et al., produced jet fuel from waste cooking and palm oils over reduced Ni catalysts loaded on different zeolite supports via hydrotreatment in a batch reactor [157], [160]. Kim et al., employed reduced Ni and Pt catalysts for the hydrotreatment of soybean oil in an autoclave reactor and reported that DCO-DCO_2 were the dominant pathways over both catalysts [73]. Yenumala et al. prepared Ni/γ-alumina catalysts using commercial γ-alumina as the support. They performed the hydrotreatment of karanja oil in a semi-batch reactor. The obtained results proved the formation of diesel range hydrocarbons by preserving the triglycerides backbone chains [74].

To date, there has been very little research exploring the use of monometallic transition metals for the hydrotreatment of triglycerides in a continuous process [161]. Kubička and Kaluža used Ni/Al_2O_3 in the sulfided form for the hydrotreating of refined rapeseed oil in a continuous fixed-bed reactor. They found a very low oxygen removal efficiency and showed that DCO-DCO_2 are the predominant pathways [3]. Santinllan-Jimenez et al. showed that the DCO-DCO_2 reaction pathways are dominant over different supported monometallic Ni catalysts in a continuous semi-batch reactor. However, the triglycerides percentages in the feed introduced to the reactor was very low [76]. Kaewmeesri et al. and Srifa et al. used reduced Ni/γ-alumina for continuous hydrotreating of triglycerides. It was found that the dominant pathway is the DCO-DCO_2 and reported a longer TOS over Ni/γ-alumina compared to Co/γ-alumina [15], [37], [79]. Since the sol-gel method allows stabilizing and confining of the metal particles in the mesoporous framework and yields homogeneous distribution of metal species, the sol-gel synthesized catalysts showed high stability over time while being used in different chemical reactions. This high stability arises from some reduction in sintering of the metallic nanoparticles due to the strong interaction between the mesoporous support and the particles [162], [163]. Thus, in this study, nickel is chosen as the

transitional metal for the hydrotreatment of canola oil as a triglycerides source. To elucidate the dependence of catalytic efficiency and stability over time to the structure of the catalysts; one pot sol-gel via Evaporation-Induced Self-Assembly (EISA) and conventional incipient wetness methods were employed for catalysts synthesis. The performance of these two kinds of Ni-based catalysts was compared for the production of green diesel in a continuous down-flow fixed bed reactor.

4.2 Materials and methods

4.2.1 Catalyst synthesis

Ni/γ-alumina catalysts were prepared by a one-pot sol-gel method via evaporation-induced self-assembly (EISA). A specific amount of triblock copolymer (Pluronic P123): Poly(ethylene glycol)$_{20}$-block-poly(propylene glycol)$_{70}$-block-poly(ethylene glycol)$_{20}$ (Average $M_n \approx 5800$ g/mol, Sigma-Aldrich, CAS no.9003-11-6) as a soft template was dissolved at ambient temperature using a magnetic stirrer in 20 mL anhydrous ethanol (Commercial alcohols Co., CAS no.67-17-5). The desired amount of (Ni $(NO_3)_2.6H_2O$) (Sigma-Aldrich, CAS no. 13478-00-7) was then added to the above solution and agitated at least for 6 h (solution A). In another beaker Al (O-i-Pr)$_3$ (Sigma-Aldrich, CAS no. 555-31-7) as the alumina precursor and 3.2 mL HNO_3 69% wt. (Sigma-Aldrich, CAS no. 7697-37-2) were added to 20 mL anhydrous ethanol and mixed for 6 h (solution B). Solutions A and B were mixed and continuously stirred (600 rpm) together overnight at ambient temperature. The resulting solutions were poured into Petri dishes and aged in a drying oven for 4 days at 60ºC letting the solvent to evaporate and the EISA process to take place. After the EISA process green to light green homogeneous solids were obtained. The total quantity of (Al+Ni) was kept constant, corresponding to a molar composition of 20 mmol. The mass ratio of Ni/Al was adjusted accordingly to (5%, 10%, 15%, and 20%). The mass ratio of P123/Al(O-i-Pr)$_3$ was equal to 1.07 for all samples. For comparison, a sample was also prepared with 10% wt. nickel without using the P123 polymeric template. All chemicals were used as received.

Calcination was carried out by gently heating the samples from 50 to 700ºC with a four-step calcination procedure in the air atmosphere. First, the temperature was increased from 50 to

160ºC and remained at this temperature for 2 h. The temperature was then raised from 160 to 280ºC and kept constant for 2 h. Afterward, the temperature was raised again from 280 to 400ºC with a 2 h residence time, and finally from 400 to 700ºC and maintained for 3h. Between plateaus, the heating rate remained constant for the whole calcination procedure at $1^{o}Cmin^{-1}$ ramping rate. This stepwise calcination process secures the complete removal of the polymeric template along with the formation of crystalline metal oxide species. For comparison, Ni/γ-alumina sample was prepared via traditional impregnation method. In short, home-made mesoporous γ-alumina (details can be found in [136]), and nickel (II) hexahydrate ($Ni(NO_3)_2.6H_2O$) (Sigma-Aldrich, CAS no. 13478-00-7) were agitated with deionized water inside a double jacket Pyrex reactor connected to a digitally-controlled water bath at 60ºC for 12 h. The loading of nickel was adjusted to 10% wt. Ni. The resulting solution was then dried at 60ºC for 24 h and ground to a fine homogeneous powder. Subsequently, the calcination process was performed in the air from 50 to 700ºC, with a rate of $1^{o}Cmin^{-1}$ and a soaking time of 3 h at the final temperature. All the catalysts were in-situ reduced inside the reactor under H_2 atmosphere prior to being used. The designation of SG-X% indicates mesoporous ordered catalysts prepared via one pot sol-gel method where X% represents the weight percentages of the introduced nickel on alumina. The WT, IMP, and R designations are denoting the samples without template, impregnated and reduced catalysts, respectively.

4.2.2 Catalytic activity measurement

Canola oil provided by Saporito Inc., Canada, with the fatty acid composition of (palmitic) C16:0 = 4.1, (stearic) C18:0 = 1.8, (oleic) C18:1 = 62.7, (linoleic) C18:2 = 19.6, (linolenic) C18:3 = 9.0, (arachidic) C20:0 = 0.6 and (behenic) C22:0 = 0.3 in % wt. was selected as feed. The feed was hydrotreated in a stainless steel 316 custom made tubular fixed-bed down-flow reactor (25.8 mm internal diameter and 400 mm length). The catalyst samples were prepared by making compressed pellets from powders using a hydraulic press. Then, they were crushed and held inside the reactor between quartz wool on a stainless steel grid. Before the reaction, the reactor was loaded with catalyst. To remove oxygen and the adsorbed species on the surface of the catalysts, N_2 (60 $mLmin^{-1}$) was introduced to the reactor, and the temperature was raised to 250ºC for 30 min; then cooled down to room temperature. Next, the catalysts were reduced in-situ by increasing the temperature from 50 to 600ºC with a

heating rate of 10ºCmin^{-1} and 3 h soaking time under H_2 flow with a rate of 60 mLmin^{-1} at atmospheric pressure. The reactor was then pressurized under N_2 and cooled down to the reaction temperature. After reaching steady state, the hydrogen gas and oil were introduced to the reactor at constant reaction condition of T = 400ºC, P = 500 psi, LHSV = 0.5 h^{-1}, and H_2/oil = 600 mLmL^{-1}. The effect of different catalyst types on the liquid composition was then investigated. Liquid products were collected after passing through a high-pressure condenser connected to a cooling circulator by the aid of a high-pressure low-temperature separator.

The oil was introduced into the reactor (without any dilution) at a constant rate using a high-pressure HPLC pump, Lab Alliance Serie II (6000 psi max pressure, 0.01-10 mLmin^{-1}). The feed flow rate was adjusted to the setpoint in a circuit line while the reactor temperature and pressure stabilized. Tubular electrical furnace (Thermo scientific^{TM}) was used to set-out the reactor temperature. For superior accuracy, a second thermocouple was placed inside the reactor alongside the catalyst bed in the middle of the reactor. Gases (H_2/N_2) were fed using Bronkhorst Co. mass flow controller (2100 psi max pressure). A back pressure regulator, 26-1700 series (TESCOM) coupled with an electropneumatic actuator, ER3000 series (TESCOM) were utilized to control the reactor operating pressure. The concentration of triglycerides and normal alkane distributions in the product were obtained from HPLC and GC-MS analysis, respectively. The oil conversion (C) was defined as follows.

$$Conversion\ (C) = \frac{Total\ mass\ of\ triglyceride\ consumed}{Initial\ mass\ of\ triglyceride} \times 100 \qquad (4.1)$$

4.2.3 Characterization

4.2.3.1 Nitrogen adsorption-desorption analysis

The adsorption-desorption isotherms of the synthesized catalysts were collected using a Quantachrome Nova 2000 instruments at -196°C. The calculations were done using the Autosorb-1 software, (Quantachrome Instruments). About 400-500 mg of the samples were put into the glass cell, and the degasification was performed by reaching a residual pressure of 10^{-6} mbar, at 200°C for a 5 h residence time. To determine the specific surface area, Standard Brunauer-Emmett-Teller (BET) isotherm was used considering the linear part of the isotherm in the relative pressure (P/P_0) range of 0.05-0.2. Barrett-Joyner-Halenda (BJH)

calculation method was employed using the adsorption branch of the isotherms to calculate the pore width. The total pore volumes (V_t) were calculated according to the volume of adsorbed nitrogen at a relative pressure of $P/P_0 = 0.99$. Non-local density functional theory (NLDFT) was also applied to determine the specific surface area (S_{DFT}), total pore volume (V_{DFT}) and pore width (W_{DFT}). Considering the cylindrical shape of pores, pore size distributions were determined using the kernel of NLDFT with the equilibrium isotherm of N_2 at -196°C on silica.

4.2.3.2 X-ray diffraction (XRD)

Wide-angle X-ray scattering (WAXS) patterns were acquired using a Siemens D5000 monochromatic diffractometer with a radiation source of Cu Kα; operating at room temperature, a voltage of 40kV and a current of 30 mA. The count time was 1.2 s with a step size of 0.02°. The counts were recorded in the range of 2θ = 10 to 90°. The samples were finely ground (< 100 µm) before the test. An additional Poly (methyl methacrylate) (PMMA) sample holder was used for the samples with low content. Crystalline phase identification was established by comparison of the recorded diffraction patterns with Joint Committee on Powder Diffraction Standards (JCPDS) database using X'pert HighScore software (version 1.0d, PAN analytical B.V., Almelo, Netherlands). Scherrer's equation was employed with applied Warren's correction to roughly calculate the mean crystal domain size of the samples.

$$D = \frac{K\lambda}{\beta \mathrm{Cos}\theta} \tag{4.2}$$

where K ≈ 0.9 (Scherrer constant), λ = 1.54059 Å (wavelength), and θ is the position of Bragg's diffraction angle. β (efficient linewidth of the X-ray reflection) is obtained considering $\beta^2 = B^2 - b^2$, where B is the full width at half maximum (FWHM), and b represents the value of instrumental broadening defined by the X-ray reflection of quartz with particle size ≥ 150 nm, at 2θ ≈ 27° FWHM, respectively, in radians [99]. Using interplanar spacing cubic lattice planes (d_{hkl}) for a set of lattice planes, the lattice parameter (a) of samples were calculated using equation (4.3).

$$d_{hkl} = \frac{a_{hkl}}{\sqrt{h^2+k^2+l^2}} \tag{4.3}$$

where *h,k,l* are the Miller integer indices [132].

4.2.3.3 X-ray photoelectron spectroscopy (XPS)

A KRATOS Axis-Ultra electron spectrometer (UK) was used to record X-ray photoelectron spectroscopy (XPS) spectra employing an Al monochromatic or Mg non-monochromatic source operating at 300 watts. The samples were placed on a stainless steel sample holder, and the pressure was 10^{-8} Torr or lower during the analysis. The survey scans were acquired using a pass energy of 160 eV and a step size of 1 eV. The Ni2p and C1s high-resolution spectra were recorded with step sizes of 0.10 and 0.05 eV and pass energies of 40 and 20 eV respectively. The electrostatic charge was neutralized using a very low energy and integrated electron flood gun for the optimization of the counting rate parameters and energy resolution. The CasaXPS software (version 2.3.17PR1.1) was used to analyze the collected spectra and calculate the surface atomic ratios. The binding energy scales were calibrated by Au4f7/2, Ag3d5/2, and Cu2p3/2 at binding energies of 83.95, 368.2, 932.6 eV, respectively. The C-H carbon peak at 285.0 eV was used to correct the binding energies.

4.2.3.4 Transmission electron microscopy (TEM)

For morphological evaluation of the synthesized catalysts, a JEM-1230 (JEOL) transmission electron microscope (TEM) with a filament thermionic emission source of lanthanum hexaboride (LaB6) was utilized. The acceleration voltage of the electron beam was set at 80 kV, and the Gatan Ultrascan 1000XP was used to adjust the electron beam. The samples were finely powdered and dispersed in methanol; followed by a mild sonication for 10 min. Then, a drop of the prepared solution (≈ 5 µL) was attentively placed on a Formvar film coated nickel grid (200 mesh) and dried at room temperature in the air atmosphere. The histogram analysis of TEM micrographs were acquired by measuring at least 100 individual particles using the ImageJ software.

4.2.3.5 High-performance liquid chromatography (HPLC)

A UHPLC (UltiMate 3000 Dionex) coupled with a UV (Thermo SCIENTIFIC Dionex UltiMate 3000) equipped with variable wavelength detector was used for analysis of liquid samples containing triglycerides (TG), diglycerides (DG) and monoglycerides (MG). The eluent solvents were acetonitrile, hexane, and isopropanol (HPLC grade - Fisher Scientific)

set at a flow rate of 0.5 $mLmin^{-1}$ (the gradient elution mode was chosen during the analysis). Acclaim™ 120, C18, 5 µm, 120 A, 4.6 × 100 mm column was used for separation. To completely drain the injected liquids, the injected volume and the measurement time were respectively adjusted to 10 µL and 60 min. The peak identifications were done by comparing the recorded peaks with those of known standards. The experiment was repeated three times for each sample.

4.2.3.6 Gas chromatography-mass spectrometry (GC-MS)

The analysis was performed using a Thermo Scientific™ ultra-trace GC ITQ-900 ion trap mass spectrometer and a DB-5ms 30m, 0.25mm, 0.25µm column (Agilent) using a flame ionization detector (FID). The Xcalibur™ Software version 2.1 was used for peak identification and concentration determination using standard analytical solution (ASTM® D2887 quantitative calibration solution, Supelco) providing the detailed distribution of the components. The protocol used for the analysis was as follows: The samples were diluted (volume: 1 µL) with CS_2, GC grade, (Sigma-Aldrich, CAS no. 75-15-0). The temperature of the GC oven was adjusted at 70ºC for 30 s to reach equilibrium. Then, the column temperature was raised with a heating rate of 10ºC min^{-1} to 300ºC and maintained at this temperature for 15 min. The temperature of FID detector and the MS source were set at 220 and 200ºC respectively, and 50 to 650 m/z scan spectra were recorded. Between two injections, the column temperature was raised to 350ºC and kept at this temperature for 10 min letting all components elute. Each injection was performed three times.

4.3 Results and discussion

4.3.1 Nitrogen adsorption-desorption analysis

The N_2 adsorption-desorption isotherms and the pore size distribution curves of γ-alumina support and the nickel catalysts are presented in Figure 4.1. As can be seen, the catalysts synthesized by sol-gel method exhibited a type IV isotherm with H2 hysteresis loop. The presence of capillary condensation step along with the presence of a defined plateau region at higher relative pressure (P/P_0) revealed the mesoporous nature of the catalysts. γ-alumina samples show type IV isotherm with H2 type hysteresis loop slightly shifted to H3, representing materials with fairly narrow pore size distribution and interconnected cylindrical

pore morphology [100]. The IMP-10% catalyst showed type IV isotherm with an H3 type hysteresis loop without any plateau region due to any adsorption limitation at high relative pressure corresponding to the slit-shaped mesostructured pores of this sample [134]. The differences between the hysteresis loops of the sol-gel and impregnated catalysts are related to the different methods of catalyst preparation. In the one-pot sol-gel synthesis method, the mesoporous structure is formed in the presence of nickel, whereas for samples prepared via incipient wet impregnation, the nickel is deposited in the mesoporous channels of the synthesized γ-alumina support that is in good agreement with the results obtained from XRD, and TEM (presented below in Figures 4.2 and 4.4, respectively). It should be noted that the PSD curves are positioned in the range of about 4 to 15 nm illustrating the mesoporous nature of the catalysts according to IUPAC classification.

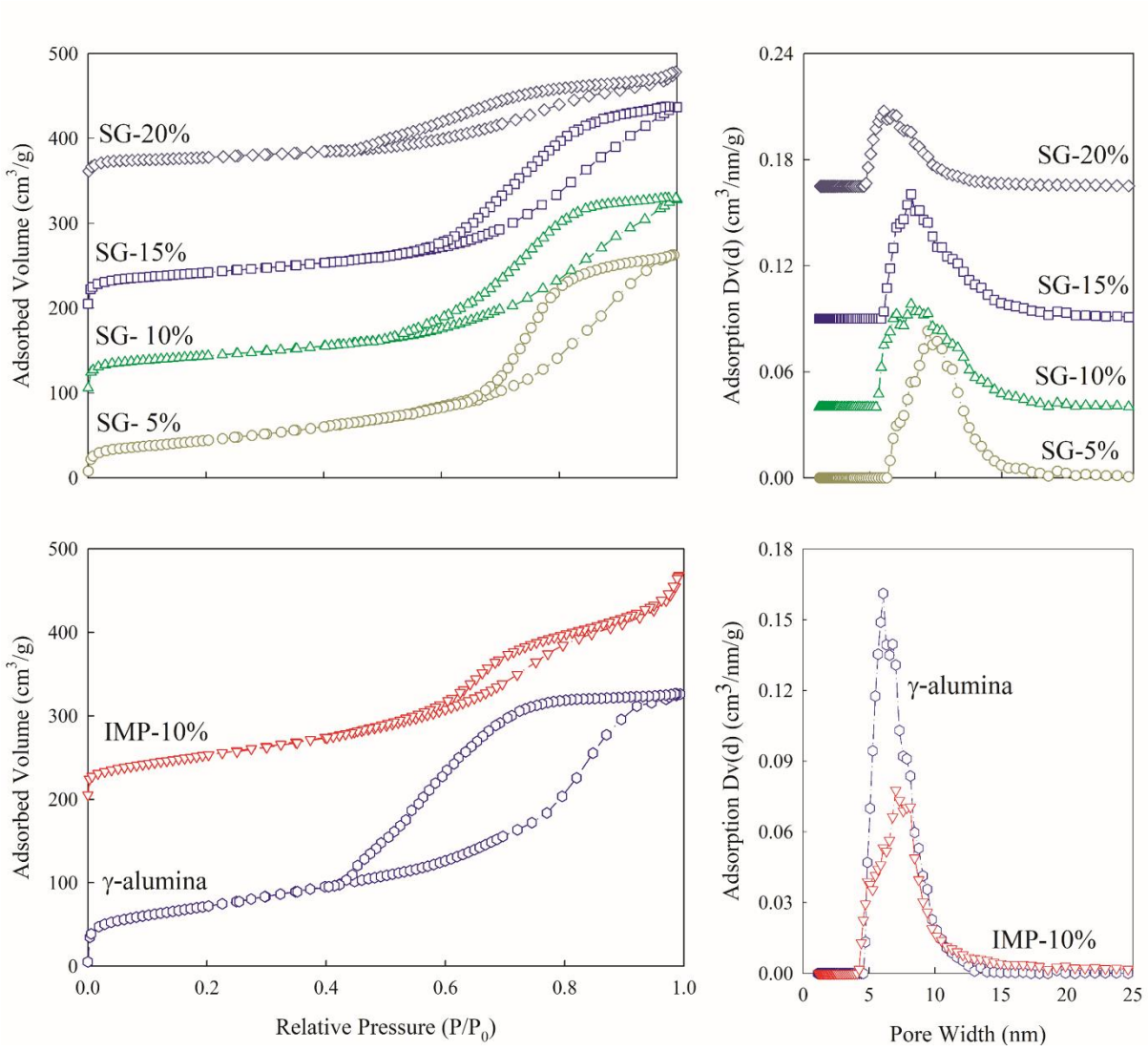

Figure 4.1. Nitrogen adsorption-desorption isotherms (left) and pore size distributions (right) for Ni catalysts, sol-gel (up). Left offset: 0, 100, 200, and 350 (cm^3/g) and right offset: 0, 0.04, 0.09, and 0.165 ($cm^3/nm/g$) on y-axis, and for γ-alumina and impregnated Ni catalyst (down). Left offset: 0 and 200 (cm^3/g) on y-axis.

Detailed textural characteristics of samples are listed in Table 4.1.

Table 4.1. Adsorption properties of the samples with different metal loadings.

Samples	S_{BET} (m^2/g)	S_{DFT} (m^2/g)	V_t (cm^3/g)	V_{DFT} (cm^3/g)	W_{BJH} (nm)	W_{DFT} (nm)
SG-5%	159	152	0.412	0.392	10.7	9.4
SG-10%	152	149	0.354	0.346	9.3	8.1
SG-15%	134	136	0.346	0.337	10.3	8.4
SG-20%	94	94	0.199	0.182	8.4	6.1
IMP-10%	201	174	0.416	0.365	8.3	7.0
γ-alumina	259	283	0.506	0.488	7.8	6.1

As can be seen in Table 4.1, it is clear that increasing the incorporated nickel content from 5% wt. up to 20% wt. led to a continuous reduction in the surface area and pore volume in sol-gel derived samples that are in agreement with previous studies [162], [164]. The S_{BET} and V_t of IMP-10% are 32.2% and 17.5% higher than those of SG-10% catalyst due to different synthesis method. A detailed description of the γ-alumina was reported in our previous work [136].

4.3.2 X-ray diffraction (XRD)

The XRD patterns of Ni-based catalysts are presented in Figure 4.2. The profiles of diffraction lines are rather asymmetric revealing a homogeneous distribution of metal species. In the non-reduced state, two nickel species could be observed: NiO formed on the surface of γ-alumina or incorporated with Al_2O_3 in the form of $NiAl_2O_4$ spinel-like species. Under similar preparation conditions, the amount of metal loading affects the formation of these different phase types [165]. As observed in Figure 4.2, the alumina sample shows the presence of γ-alumina phase (*Fd3m* cubic crystal structure) with diffraction peaks of (400) at $2\theta \approx 46.0°$ and (440) at $2\theta \approx 66.8°$ which correspond to aluminum oxide (JCPDS No. 29-0063). The IMP-10% XRD patterns show the peaks of γ-alumina with additional three diffraction peaks located at $2\theta \approx 43$, and 63° which are respectively related to (200), and (220) planes of NiO with *Fm3m* cubic crystal structure (JCPDS No. 04-0835), showing the

presence of NiO phase for this sample. No characteristic peak of metallic Ni was observed for any non-reduced catalyst samples [166]. For SG-5%, three minor broad peaks are detected at $2\theta \approx 37, 45, 66°$ which are mainly ascribed to $NiAl_2O_4$ with *Fd3m* cubic crystal structure (JCPDS No. 81-0716). These peaks are extremely weak for SG-5%, however, they are more clearly observed at higher nickel contents (above 10%) [123]. The γ-alumina phase was not observed at 10% nickel, and the $NiAl_2O_4$ phase was formed after diffusion of nickel into the amorphous alumina phase. The broader diffraction pattern of SG-5% indicates that the Ni particles were highly dispersed in this alumina phase. Further increase in nickel content (SG-10%) results in a slight shift of the γ-alumina peak at ≈ 66° to a lower 2θ value suggesting an increase in $NiAl_2O_4$ phase. No diffraction peak associated with NiO phase ($2\theta \approx 37, 43,$ and 63°) was observed for SG-5% and SG-10% samples revealing that nickel was well dispersed and incorporated into the alumina structure through the one-pot sol-gel assisted EISA strategy [162]. Comparing the XRD patterns of IMP-10% with SG-10% shows that the NiO phase is only observed for IMP-10%, revealing that employment of the one-pot sol-gel approach, hindered the formation of large NiO species on the surface of SG-10% catalyst and stabilized nickel in the alumina phase. For SG-15% and SG-20% samples, the peaks at $2\theta \approx$ 37, 43, and 63° are respectively attributed to (111), (200), and (220) planes of NiO phase. The similar intensity of these peaks in the XRD patterns of IMP-10% and SG-15% indicates the sol-gel method was more efficient in the $NiAl_2O_4$ spinel formation. The peaks are sharpened at SG-20% sample, pointing out that further increase in the Ni content led to the formation of large NiO crystals on the surface, and the excess Ni did not diffuse into the alumina framework. The average crystallite sizes roughly calculated from (200) plane of NiO were 17.9, 16.9, 23.3, and 28.6 nm for IMP-10%, SG-10%-WT, SG-15%, and SG-20%, respectively. The NiO crystallite sizes of SG-5% and SG-10% were not estimated due to lack of XRD peaks associated with NiO phase for these samples. The NiO crystallite size of IMP-10% and SG-10%-WT were comparable suggesting the stabilizing effect of P123 polymeric template on the incorporation of nickel in the mesostructured framework. Further increase in the nickel content (SG-15% and SG-20%) led to the formation of larger NiO crystallites which is in accordance with the larger nickel particle size on the surface of the catalyst in TEM micrographs presented in Figure 4.4. It seems that there is a metal loading concentration above which the nickel species start accumulating as NiO on the surface of the catalysts.

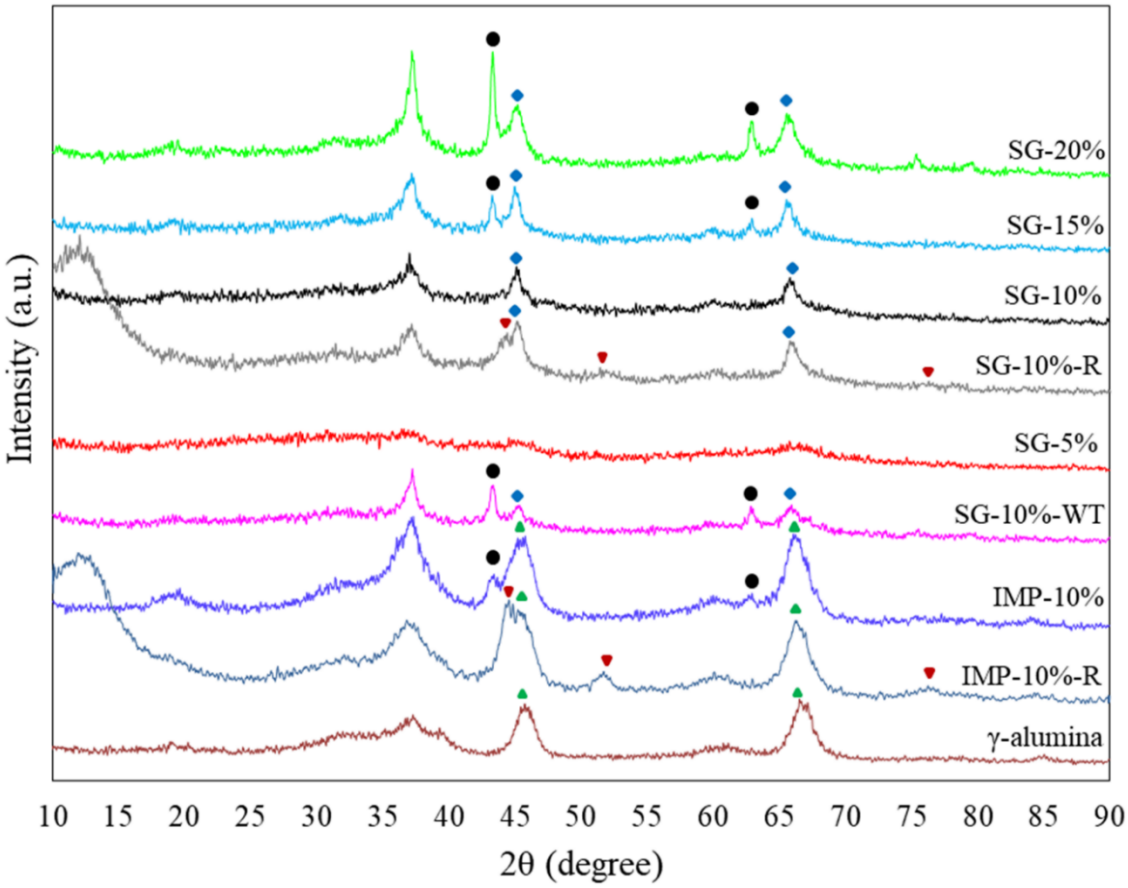

Figure 4.2. X-ray diffraction patterns of Ni-based catalysts (NiO ●, Ni^0 ▼, $NiAl_2O_4$ ◆, γ-alumina ▲).

The lattice parameters of the catalysts are presented in Table 4.2.

Table 4.2. γ-alumina lattice parameter of the samples.

Sample	Lattice parameter (nm)
γ-alumina	0.7917
SG-5%	0.7943
SG-10%	0.8034
SG-15%	0.8038
SG-20%	0.8023
SG-10%-WT	0.8002
IMP-10%	0.7939

The ionic radius of alumina is smaller than that of nickel, and thus the addition of nickel leads to a lattice expansion [138], [167]. As can be seen in Table 4.2 the lattice parameters of the γ-alumina phase increased from sample SG-5% to SG-10% which shows that the amount of nickel incorporated in the γ-alumina lattice was increased. For SG-15% and SG-20% samples, due to the small intensity and overlapping of the alumina peaks, refinement technique was employed, which made the rough estimation of the lattice parameters possible. This rough calculation and the lattice parameter values of these two samples let us to believe that further increase in nickel content does not notably affect the lattice parameter resulting in the approximately same lattice parameters for SG-10, 15 and 20% samples.

It can thus be concluded that at concentrations above 10% wt. nickel, the Ni species were not well-introduced into the alumina lattice and accumulated on the surface of the mesoporous structure in the form of nickel oxide. Comparing the lattice parameter of SG-10% and SG-10%-WT proves the efficiency of the EISA method for introduction of nickel in the mesoporous framework. The lattice parameter of IMP-10% is nearly the same as that of γ-alumina showing that nickel species are not incorporated into the γ-alumina lattice. This indicates that nickel species are present in the form of NiO on the walls of the alumina porous structure which is in accordance with obtained XRD patterns (Figure 4.2). All studies reported below were therefore performed using catalysts loaded with 10% wt. of nickel.

The XRD patterns of SG-10%-R and IMP-10%-R samples show the diffraction peaks locate at $2\theta \approx 44, 52, 76^{o}$ which is attributed to Ni^{0} with *Fm3m* cubic crystal structure (JCPDS No. 04-0850). To be more precise, the same sample contents reduced in the reaction chamber of the XPS device were used for the XRD analysis using a Poly (methyl methacrylate) (PMMA) sample holder (due to the small amount of samples). Thus, the broad peaks in reduced sample patterns ($2\theta \approx 10$ to 25^{o}) are likely from the sample holder. A higher reduction is achieved under the same conditions for sample IMP-10% compared to SG-10% considering the same XRD pattern counts scales and the sharper Ni^{0} peaks of IMP-10% compared to SG-10%. This could be due to the presence of more accessible reducible nickel species on the IMP-10% sample.

4.3.3 X-ray photoelectron spectroscopy (XPS)

XPS spectra of SG-10%-WT in oxidic form and SG-10% and SG-10%-IMP in oxidic and reduced forms are presented in Figure 4.3. To avoid re-oxidation of the reduced samples, the catalysts were reduced in-situ in the reaction chamber of the XPS spectrometer by increasing the temperature from 25 to 600ºC under H_2 flow of 60 $mLmin^{-1}$, with a heating rate of 10ºC min^{-1} and 3 h soaking time. As depicted in Figure 4.3, the Ni2p spectra of oxidic SG-10%, SG-10%-WT and IMP-10% samples consist of Ni2p3/2 (respectively positioned at ca. 855.7±0.1, 855.8±0.1 and 855.8±0.1 eV) and Ni2p1/2 peaks (positioned respectively at ca. 873.1±0.1, 873.2±0.1 and 873.3±0.1 eV). It is normally not possible to clearly distinguish the NiO and $NiAl_2O_4$ phases with XPS, due to the similarity of their binding energy values. Generally, the reported binding energies for $NiAl_2O_4$ are slightly higher (about 0.5 eV) than those of NiO [147].

Therefore it might be hypothesized that the Ni2p3/2 lines observed at 858.1, 857.1 and 857.3 eV in the deconvolution of these peaks belong to Ni in $NiAl_2O_4$ for samples SG-10%WT, SG-10%, and IMP-10% respectively. This would be in agreement with the observation of this phase by XRD patterns of SG-10%WT and SG-10%. The XRD patterns of IMP-10% do not show the lines of $NiAl_2O_4$, clearly indicating that this phase would be highly dispersed in this sample. The XPS derived surface atomic fractions values are presented in Table 4.3. The Ni/Al atomic ratio is lower in SG-10% compared to IMP-10% and SG-10%-WT samples (by about 27.4% and 25.6%, respectively). This reveals the effectiveness of evaporation-induced self-assembly in incorporating nickel species in the mesoporous framework in addition to the role of constructing the mesoporous structure. Both reduced samples show lower Ni/Al ratio than their non-reduced counterparts. These results are in good agreement with lattice parameter order of 0.7939 > 0.8002 > 0.8034 for IMP-10%, SG-10%-WT, and SG-10% presented in Table 4.2, which also suggests a higher incorporation of Ni ions in the alumina lattice of SG-10%. All samples show higher Ni/Al atomic ratio values than the Ni/Al atomic ratio value of the bulk (≈ 0.051) which would result from some surface segregation [168].

Table 4.3. The atomic ratio values of the catalysts obtained from XPS.

Sample	Ni2p	Al2p	O1s	Ni/Al
SG-10%	3.42	30.48	64.82	0.122
IMP-10%	5.09	30.35	61.94	0.168
SG-10%-WT	4.44	27.04	64.18	0.164
SG-10%-R	2.28	30.32	66.00	0.075
IMP-10%-R	4.04	28.21	65.85	0.143

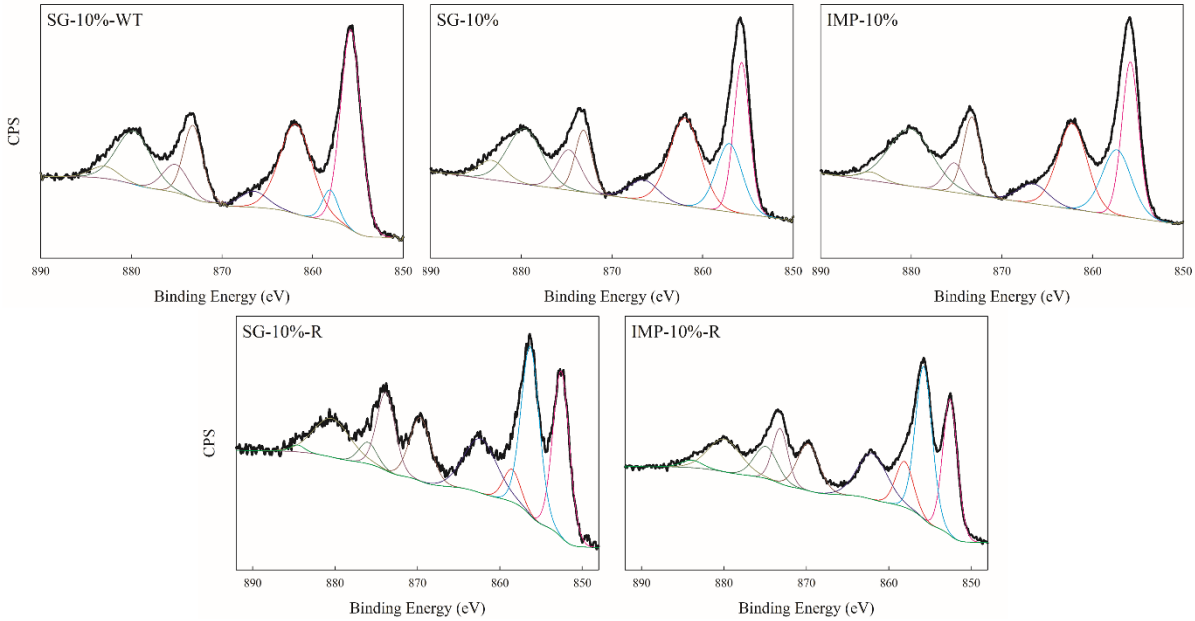

Figure 4.3. XPS spectra of Ni2p of catalysts in oxidic and reduced form.

The XPS spectra of reduced samples of SG-10%-R and IMP-10%-R are also presented in Figure 4.3. After reduction, peaks approximatively centered at binding energies of 852.6±0.1 and 869.6±0.1 eV are manifested for sample SG-10%-R. For IMP-10%-R sample, these peaks are positioned at binding energies of 852.5±0.1 and 869.8±0.1 eV. These peaks are respectively attributed to Ni2p3/2 and Ni2p1/2 in the metallic state (Ni^0) [71], [169].

Just like oxidized samples, SG-10%-R, and IMP-10%-R samples have peaks centered at ca. 856.3±0.1 and 855.7±0.1 eV and 873.8±0.1 and 873.2±0.1 eV respectively, which are attributed to Ni2p3/2 and Ni2p1/2 lines of NiO. The coexistence of $Ni^{2+}$and Ni^{0} species for both reduced samples revealed that, under the applied conditions, the reduction is only partial. These results are in good agreement with the XRD patterns of the reduced samples.

The percentages of Ni^{0} peak area calculated from the deconvolution of the Ni2p lines are 32.1% and 28.8% for SG-10%-R and IMP-10%-R, respectively. The atomic fraction of Ni sensed by XPS in SG-10%-R and IMP-10%-R are equal to 2.28% and 4.04% respectively (see Table 4.3). Thus, the overall metallic nickel at the surface of IMP-10%-R compared to SG-10%-R is ≈ 1.59 times higher. This could explain the higher conversion of triglycerides reached with the impregnated catalyst

4.3.4 Transmission electron microscopy (TEM)

TEM micrographs and particle size distributions of the catalysts are illustrated in Figure 4.4, to investigate the effect of metal species and various synthesis methods on the morphological properties of the catalysts. The average particle size of the Ni bearing phase measured from TEM micrographs of sol-gel derived samples are also presented.

Nickel particles are perceived in the form of black spots. TEM micrographs of the catalysts synthesized by the sol-gel method provide the evidence that nickel particles are fairly dispersed, and the mesoporous structure is maintained which is also confirmed by BET (Figure 4.1). It can be found that increasing the metal content led to an increase in the particle size which is also detectable by a reduction in the surface area of samples from SG-5% to SG-20% (see Table 4.1). At high nickel content, in samples SG-15% and SG-20% nickel particles agglomeration is observed.

As can be seen in Figure 4.4a, SG-5% has a narrow particle size distribution centered at approximately 2.6 nm. Further increase in nickel content up to 10% wt. brings an increase to 5.8 nm in the average particle diameter (Figure 4.4b). Due to the incorporation of metal species into the alumina support, the contrast between the particle and the alumina structure is not high leading to some inaccuracies in the detection of particles from TEM micrographs. Considering this error, these results are in accordance with the XRD patterns of sample SG-

5% and SG-10% (Figure 4.2) revealing a small particle size and uniform dispersion of nickel in the mesoporous structure.

For SG-15% and SG-20% samples (Figures 4.4c and d), particle growth and agglomeration were observed. The roughly measured average particle sizes of about 13.8 and 23.9 nm are obtained which follows the same trend of the crystallite sizes calculated from Scherrer's equation from XRD patterns. These observations are in accordance with the presence of sharp peaks associated with NiO phase in XRD patterns of SG-15% and SG-20% samples (Figure 4.2) and confirmed the large grain size of these samples. As can be seen in Figure 4.4, less homogeneity is observed in the TEM micrograph of sample SG-10%-WT (Figure 4.4e) compared to SG-10% (Figure 4.4b). The black agglomerated area is possibly formed due to the lack of the P123 polymeric template in the synthesis step. The TEM micrograph of the mesostructured γ-alumina and the IMP-10% samples are respectively shown in Figures 4.4f and g. The γ-alumina support shows long range mesopores which are partially filled by dispersed nickel while introducing metal species via impregnation method. The presence of mesopores is evident even after nickel loading. These observations are in line with N_2 adsorption-desorption isotherm of the IMP-10% sample presented in Figure 4.1.

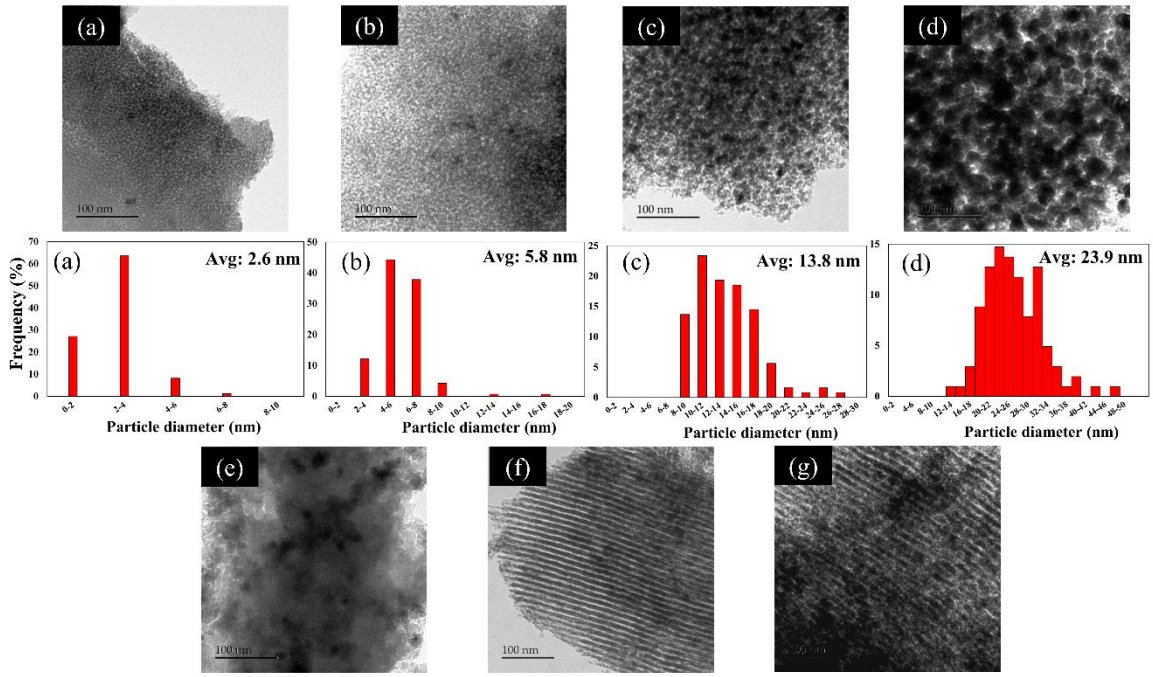

Figure 4.4. TEM micrographs of (a) SG-5%, (b) SG-10%, (c) SG-15% and (d) SG-20% catalysts and their corresponding PSD histograms, (e) SG-10%-WT, (f) γ-alumina, and (g) IMP-10%.

4.3.5 Hydrotreatment over the prepared catalysts

To evaluate the effects of the two different synthesis methods on the catalytic properties, sample SG-10%-R, and IMP-10%-R were chosen as catalysts for the hydrotreatment of canola oil. The conversion of the triglycerides up to 600 min over catalysts are presented in Figure 4.5, left. The liquid conversion over IMP-10%-R for TOS of 150 and 300 min is 81.5% and 76.8% respectively. For the first 300 min of the reaction, the liquid conversion over IMP-10%-R is higher than that over SG-10% sample. This could be due to the higher surface area of reduced nickel on the surface of IMP-10%-R compared to SG-10%-R (confirmed with XRD and XPS analysis). At TOS of 300 to 450 min, IMP-10%-R lost its activity, and the liquid conversion decreased sharply and reached about 37.4%. After this sharp reduction, the conversion remained relatively stable and reached 30.9% at the TOS of 600 min. This fast deactivation could probably be related to the adsorption of the unsaturated triglycerides on the surface of the catalyst, leading to coke formation on the acidic sites of

the catalyst or due to the sintering of the nickel species on the γ-alumina surface [170]. For SG-10%-R, a continuous decline of the conversion started at TOS of 150 min (68.6%) up to 600 min (54.0%). The lower conversion of SG-10%-R could be due to the fewer accessible reduced nickel on this sample compared to IMP-10%-R. The confinement of the nickel species in the mesoporous framework of SG-10%-R reduced the activity through blocking some metallic nickel sites. On the other hand, it also prevents the fast deactivation of this catalyst. This lower deactivation rate is gained at the cost of a reduced catalytic activity. The transformation of canola oil to green diesel could be executed either by HDO or DCO-DCO_2 pathways. If the reaction goes through HDO, the n-alkane products have the same number of carbon atoms as that the corresponding fatty acid of the triglycerides molecules. If the reaction goes through DCO-DCO_2, the resulting n-alkane has one carbon less than the corresponding fatty acids. Hence, the ratios of C17/C18 and C15/C16 show the selectivity over HDO and DCO-DCO_2. Figure 4.5 (right) displays the C15/C16 and C17/C18 as functions of TOS. Both catalysts favored the DCO-DCO_2 pathway in the TOS range of 150 to 600 min which corresponds to a lower hydrogen consumption. The two ratios are slightly reduced from 150 to 600 min of TOS over both catalysts. The 17/C18 ratios are similar over SG-10%-R and IMP-10%-R. The C15/C16 ratio is higher for IMP-10%-R compared to SG-10%-R, indicating a higher tendency of IMP-10%-R catalyst for the DCO-DCO_2 pathways on shorter chain fatty acids.

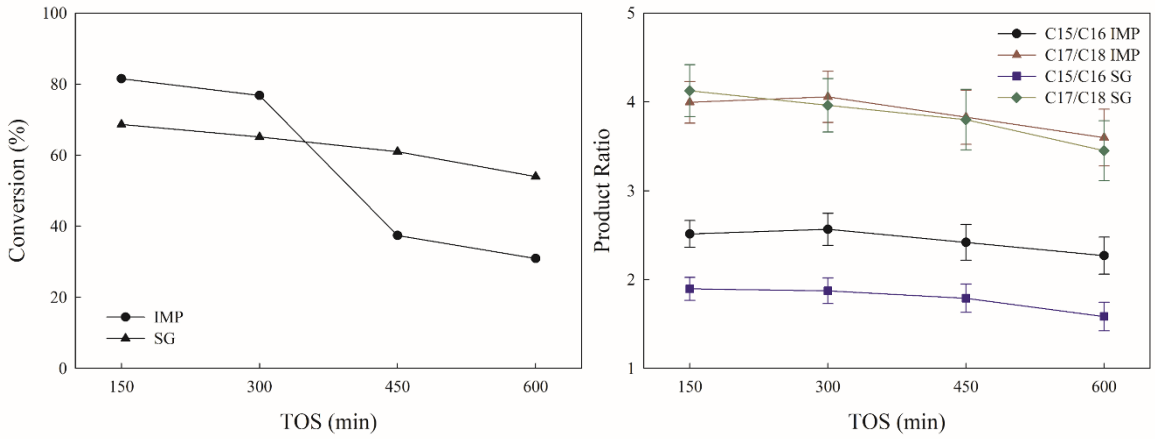

Figure 4.5. Triglycerides (left) conversion and (right) DCO-DCO_2/HDO selectivity ratio over IMP-10%-R and SG-10%-R catalysts at different TOS, T = 400ºC, P = 500 psi, H_2/oil = 600 $mLmL^{-1}$ and LHSV = 0.5 h^{-1}.

The liquid normal alkane chain length distributions of the hydrotreated products over IMP-10%-R and SG-10%-R are presented in Figure 4.6. The three represented fractions of C9-14, C15-C18, and C19-C30 are respectively considered as cracked, diesel, and oligomerized fractions. As can be seen, up to TOS of 300 min, IMP-10%-R (left) shows higher cracked components compared to SG-10%-R (right). This could be caused by a higher acidity of this sample due to the presence of the γ-alumina structure. From TOS of 150 min to 600 min, a reduction of about 7.5% in cracked products, and a 4.4 times increase in oligomerized product was observed for IMP-10%-R (Figure 4.6 left). These oligomerized products might be generated as coke precursors and their increased fraction are correlated with decreasing conversion. Interestingly, the rapid deactivation observed between 300 and 450 min is accompanied by an abrupt change in both C9-C14 and C19-C30 ratios (Figure 4.6, down). The evolution with conversion (or TOS) of these two ratios follows the same trends (at different values) for the two catalysts. IMP-10%-R shows higher cracking activity (C9-C14) suggesting a higher surface concentration of acid sites. Although the diesel fraction values are higher for IMP-10%-R catalyst, the lower conversion of IMP-10%-R at TOS above 450 min is the limiting factor of this catalyst.

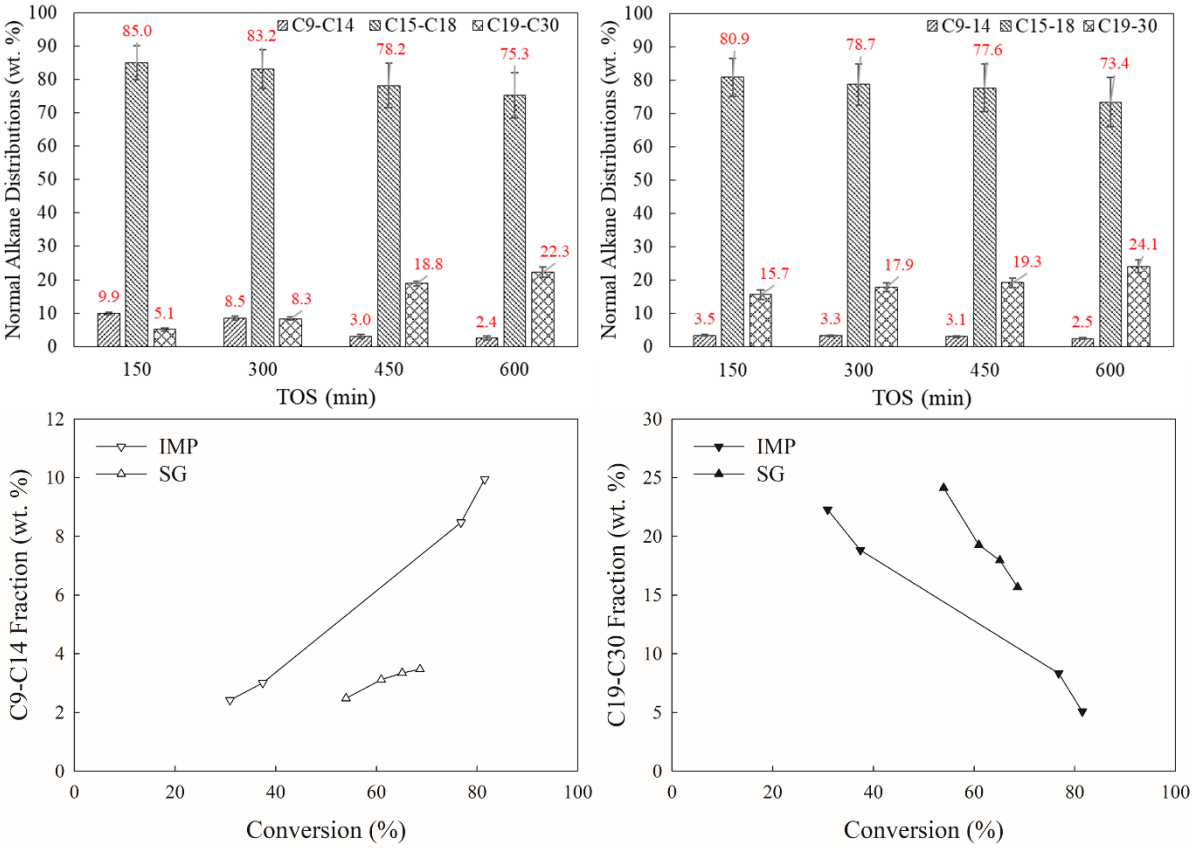

Figure 4.6. Normal alkane distributions of liquid products over (up left) IMP-10%-R and (up right) SG-10%-R catalysts at different TOS, T = 400ºC, P = 500 psi, H_2/oil = 600 $mLmL^{-1}$ and LHSV = 0.5 h^{-1}, cracked fraction (down left) and oligomerized fraction (down right) of product.

A lower acidity of SG-10%-R due to the formation of $NiAl_2O_4$ spinel-like phase is in agreement with literature data [170]. The opposite trends of C9-C14 and C19-C30 as functions of conversion, suggest that the two processes of cracking and oligomerization are not occurring on the same sites with the two kinds of sites being affected differently upon deactivation. To conclude, the diesel/cracking and oligomerized products decreased and increased respectively over both catalysts. Moreover, higher stability observed for SG-10%-R as a result of smooth deactivation trend over the studied reaction time range. The SG-10%-

R catalyst shows better stability during hydrotreatment which may be due to the confinement of active metals caused by the employed sol-gel method.

4.4 Conclusion

This work confirms that triglycerides hydrotreatment in a continuous down-flow reactor is possible to run over a non-sulfided metal catalyst supported on alumina. The catalyst preparation method is shown to be of importance for the catalytic properties in this reaction. The sol-gel technique involving evaporation-induced self-assembly was shown to yield more stable properties than the conventional γ-alumina impregnation method. This difference between the two materials was associated with the formation of a $NiAl_2O_4$ phase and a less acidic support.

Acknowledgements

We acknowledge Dr. Alain Adnot, Jean Frenette and Pierre Audet from Departments of Chemical Engineering, Geological Engineering, and Chemistry at Laval University for their constructive comments and help on XPS, XRD, and GC-MS analysis. The financial support of Natural Science and Engineering Council of Canada (NSERC, Grant numbers: STPGP 396579 and RGPIN-2015-06175) is gratefully acknowledged.

Chapter 5

Conclusions and recommendations

5.1 General conclusions

The development of clean, sustainable fuels from renewable resources, as a replacement for fossil fuels, is considered to be vital on account of the negative effect of the latter particularly on the environment especially with respect to global warming. This is why this work was devoted to the development of hydroprocessing of vegetable oils over various catalysts.

First, mesoporous alumina was synthesized via one-pot sol-gel assisted method along with the EISA process. Aluminum isopropoxide $Al(O\text{-}i\text{-}Pr)_3$ was used as aluminum source and (Pluronic P123) triblock copolymer poly (ethylene oxide)$_{20}$-poly (propylene oxide)70-poly (ethylene oxide)20 as structure directing agent. The effects of different contents of polymeric template ranging from P123/$Al(O\text{-}i\text{-}Pr)_3$ mass ratios of 0.49 to 1.96 and calcination temperatures ranging from 650 to 1050ºC were investigated. Increasing the P123/$Al(O\text{-}i\text{-}Pr)_3$ ratio from 0.49 to 1.96 resulted in the formation of different pore morphologies. Among different P123/$Al(O\text{-}i\text{-}Pr)_3$ mass ratios, the ratios of 0.98 and 1.47 along with a calcination temperature of 700ºC led to the formation of γ-alumina with the highest surface area and pore volume. Those samples were then thermally treated and the minimum of 700ºC with a residence time of 3 h was found to be required for complete removal of the polymeric template which led to the formation of the mesostructured γ-alumina. The increase in calcination temperature resulted in the formation of larger pores and a reduced surface area. All samples showed thermal stability up to 950ºC. Above this temperature at 1050ºC the surface area and the total pore volume drastically decreased. XRD analysis showed that the γ-alumina phase is retained up to 950ºC. Above this temperature at 1000ºC a polymorph of γ-alumina and α-alumina phases is appearing which by further increasing the temperature to

1050ºC is transformed to the α-alumina phase. From 950 to 1050ºC the crystalline domain size of the mesoporous alumina increased from 9.9 to 29.6 nm which occurred simultaneously with a mesostructure collapse. TEM observation revealed that a mesoporous structure with pore diameter in the range of 5 to 10 nm was produced. It was shown that the properties of this mesoporous material with good thermal stability could be tuned to be applied as catalysts support. Furthermore, the relatively high surface area and pore volume are appropriate when the reactants are large molecules such as triglycerides and also make possible a higher loading of active metals on the support.

Next, the mesostructured γ-alumina with P123/Al(O-i-Pr)$_3$ mass ratio of 0.98 and the calcination temperature of 700ºC with 3 h soaking time was used as hydrotreatment catalyst support. NiMo/γ-alumina and CoMo/γ-alumina catalysts were prepared via incipient wetness co-impregnation by loading 15% wt. MoO_3 and 3% wt. NiO or CoO. Canola oil was used as triglycerides source, and the hydrotreatment was performed in a fixed-bed down-flow reactor. The effect of temperature and LHSV in the ranges of 325 to 400ºC and 1 to 3 h^{-1} respectively, on the green diesel properties were investigated while keeping other reaction conditions constant (P: 450 psi and H_2/oil: 600 $mLmL^{-1}$). The hydrotreating of canola oil on both supported NiMo and CoMo sulfided catalysts makes possible the production of diesel range liquid hydrocarbons mostly C15-C18 due to the high surface area and large porosity of the γ-alumina support. The temperature of 325ºC and LHSV of 1 h^{-1} were found to be optimum, and both sulfided NiMo and CoMo catalysts could be considered as promising catalysts systems for hydrotreating of canola oil. Some minor advantages regarding reaction rate and selectivity to green diesel production were found for NiMo/γ-alumina compared to CoMo/γ-alumina. Increasing temperature for both catalysts resulted in an increase in cracking and oligomerization reactions.

Finally, metal sulfided catalysts needed to be sulfided at high temperature using a sulfiding agent. Without using the sulfiding agent, the catalytic activity is limited. The sulfide will however leach to the products, which is harmful to human health, environment and also causes damages to the infrastructures. Therefore, developing a new type of inexpensive and non-sulfided catalyst is a fascinating subject. In this part of the work, non-sulfided Ni/γ-alumina catalysts were synthesized via conventional wet impregnation and one-pot sol-gel

methods. The results confirmed that the hydrotreatment of vegetable oil is possible over non-sulfided heterogeneous Ni/γ-alumina at the reaction conditions of T: 400ºC, P: 500 psi, LHSV: 0.5 h^{-1} and H_2/oil 600 $mLmL^{-1}$. Due to the incorporation of nickel in the mesostructured framework lower level of bulk nickel oxide is present on the surface of the sol-gel derived catalyst compared to the impregnated one. Finally, both catalysts favored the decarboxylation-decarbonylation reaction routes affecting the hydrogen consumption. Higher stability was found for the sol-gel catalyst, associated with the formation of $NiAl_2O_4$ phase resulting in a lower acidity support.

5.2 Recommendations for future work

In the field of hydroprocessing of vegetable oils and to extend the application range of various catalysts, the following directions are suggested for future works:

- Utilization of other structure directing polymeric templates and investigate their effect on the textural properties of synthesized γ-alumina to enhance their industrial application as a catalyst support depending on the reactant type.

- The feasibility of highly active NiMo/γ-alumina and CoMo/γ-alumina synthesized via co-incipient wetness impregnation technique has been verified. Various controllable parameters could be further studied; such as active metal concentration (regarding the structural properties of the support), the optimized ratio of promoter to molybdenum, adding protocol of deposition of active metals and finding the best temperature for impregnation process.

- Use of other potential metals as promoters (or active metal) and study their sulfided state to better understand their complex behavior in interaction with the molybdenum active phase.

- Investigation on the incorporation of other active metals rather than Ni into the mesoporous framework via sol-gel process and study of distribution and interaction of these metals with the mesoporous support material.

- Study of the carbon deposition in bi- and monometallic catalysts considering different loaded metals and their interaction with the support.

- Use of non-edible source oils such as WCO and algae, as feedstock. Since WCOs have high water and free fatty acid contents, they are likely to be further studied. Algae oils have different triglyceride chain lengths than other oils and contain impurities such as phospholipids which may affect the composition of the final product, and could therefore be of interest for further investigations.

References

[1] "International Energy Outlook," 2016.

[2] R. Gorham, "Air Pollution From Ground Transportation an Assessment of Causes , Strategies and Tactics , and Proposed Actions for the International Community," 2002.

[3] D. Kubička and L. Kaluža, "Deoxygenation of vegetable oils over sulfided Ni, Mo and NiMo catalysts," *Appl. Catal. A Gen.*, vol. 372, no. 2, pp. 199–208, 2010.

[4] X. Zhao, L. Wei, S. Cheng, and J. Julson, "Review of Heterogeneous Catalysts for Catalytically Upgrading Vegetable Oils into Hydrocarbon Biofuels," *Catalysts*, vol. 7, no. 3, 2017.

[5] Z. Si, X. Zhang, C. Wang, L. Ma, and R. Dong, "An Overview on Catalytic Hydrodeoxygenation of Pyrolysis Oil and Its Model Compounds," *Catalysts*, vol. 7, no. 6, 2017.

[6] A. V. Bridgwater, "Review of fast pyrolysis of biomass and product upgrading," *Biomass and Bioenergy*, vol. 38, pp. 68–94, Mar. 2012.

[7] J.-H. Tsai, S.-J. Chen, K.-L. Huang, Y.-C. Lin, W.-J. Lee, C.-C. Lin, and W.-Y. Lin, "PM, carbon, and PAH emissions from a diesel generator fuelled with soy-biodiesel blends," *J. Hazard. Mater.*, vol. 179, no. 1, pp. 237–243, 2010.

[8] E. G. Shay, "Diesel fuel from vegetable oils: Status and opportunities," *Biomass and Bioenergy*, vol. 4, no. 4, pp. 227–242, 1993.

[9] T. J. Wallington, C. K. Lambert, and W. C. Ruona, "Diesel vehicles and sustainable mobility in the U.S.," *Energy Policy*, vol. 54, pp. 47–53, 2013.

[10] A. . Ramadhas, S. Jayaraj, and C. Muraleedharan, "Use of vegetable oils as I.C. engine fuels—A review," *Renew. Energy*, vol. 29, no. 5, pp. 727–742, Apr. 2004.

[11] C.-C. Chang and S.-W. Wan, "China's Motor Fuels from Tung Oil," *Ind. Eng. Chem.*, vol. 39, no. 12, pp. 1543–1548, Dec. 1947.

[12] Y. Liu, R. Sotelo-Boyás, K. Murata, T. Minowa, and K. Sakanishi, "Hydrotreatment

of Vegetable Oils to Produce Bio-Hydrogenated Diesel and Liquefied Petroleum Gas Fuel over Catalysts Containing Sulfided Ni–Mo and Solid Acids," *Energy & Fuels*, vol. 25, no. 10, pp. 4675–4685, 2011.

[13] S. R. Chia, H. C. Ong, K. W. Chew, P. L. Show, S.-M. Phang, T. C. Ling, D. Nagarajan, D.-J. Lee, and J.-S. Chang, "Sustainable approaches for algae utilisation in bioenergy production," *Renew. Energy*, Apr. 2017.

[14] M. Toba, Y. Abe, H. Kuramochi, M. Osako, T. Mochizuki, and Y. Yoshimura, "Hydrodeoxygenation of waste vegetable oil over sulfide catalysts," *Catal. Today*, vol. 164, no. 1, pp. 533–537, Apr. 2011.

[15] R. Kaewmeesri, A. Srifa, V. Itthibenchapong, and K. Faungnawakij, "Deoxygenation of Waste Chicken Fats to Green Diesel over Ni/Al_2O_3: Effect of Water and Free Fatty Acid Content," *Energy & Fuels*, vol. 29, no. 2, pp. 833–840, 2015.

[16] M. Chiappero, P. T. M. Do, S. Crossley, L. L. Lobban, and D. E. Resasco, "Direct conversion of triglycerides to olefins and paraffins over noble metal supported catalysts," *Fuel*, vol. 90, no. 3, pp. 1155–1165, 2011.

[17] Y. C. Sharma and B. Singh, "Development of biodiesel from karanja, a tree found in rural India," *Fuel*, vol. 87, no. 8–9, pp. 1740–1742, 2008.

[18] S. Gong, A. Shinozaki, M. Shi, and E. W. Qian, "Hydrotreating of Jatropha Oil over Alumina Based Catalysts," *Energy & Fuels*, vol. 26, no. 4, pp. 2394–2399, 2012.

[19] K. Openshaw, "A review of Jatropha curcas: an oil plant of unfulfilled promise," *Biomass and Bioenergy*, vol. 19, no. 1, pp. 1–15, 2000.

[20] L. M. L. Laurens, M. Chen-Glasser, and J. D. McMillan, "A perspective on renewable bioenergy from photosynthetic algae as feedstock for biofuels and bioproducts," *Algal Res.*, vol. 24, pp. 261–264, 2017.

[21] N. R. Council, *Biobased Industrial Products: Research and Commercialization Priorities*. Washington, DC: The National Academies Press, 2000.

[22] T. Kandaramath Hari, Z. Yaakob, and N. N. Binitha, "Aviation biofuel from renewable resources: Routes, opportunities and challenges," *Renew. Sustain. Energy*

Rev., vol. 42, pp. 1234–1244, Feb. 2015.

[23] A. Philippaerts, P. Jacobs, and B. Sels, "CHAPTER 10 Catalytic Hydrogenation of Vegetable Oils," in *Catalytic Hydrogenation for Biomass Valorization*, The Royal Society of Chemistry, 2015, pp. 223–241.

[24] X. Dupain, D. J. Costa, C. J. Schaverien, M. Makkee, and J. A. Moulijn, "Cracking of a rapeseed vegetable oil under realistic FCC conditions," *Appl. Catal. B Environ.*, vol. 72, no. 1, pp. 44–61, 2007.

[25] R. Sotelo-Boyás, F. Trejo-Zárraga, and F. de J. Hernández-Loyo, "Hydroconversion of Triglycerides into Green Liquid Fuels," in *Hydrogenation*, I. Karamé, Ed. Rijeka: InTech, 2012.

[26] M. J. Ramos, C. M. Fernández, A. Casas, L. Rodríguez, and Á. Pérez, "Influence of fatty acid composition of raw materials on biodiesel properties," *Bioresour. Technol.*, vol. 100, no. 1, pp. 261–268, 2009.

[27] S. Yan, C. DiMaggio, H. Wang, S. Mohan, M. Kim, L. Yang, S. O. Salley, and K. Y. S. Ng, "Catalytic conversion of triglycerides to liquid biofuels through transesterification, cracking, and hydrotreatment processes," *Curr. Catal.*, vol. 1, pp. 41–51, 2012.

[28] J. Hancsok, "Investigation of fuel components produced by the isomerization of bio-paraffin mixture," *Hungarian J. Ind. Chem.*, vol. 39, no. 1, pp. 121–126, 2011.

[29] M. Snåre, I. Kubičková, P. Mäki-Arvela, K. Eränen, and D. Y. Murzin, "Heterogeneous Catalytic Deoxygenation of Stearic Acid for Production of Biodiesel," *Ind. Eng. Chem. Res.*, vol. 45, no. 16, pp. 5708–5715, Aug. 2006.

[30] M. Mohammad, T. Kandaramath Hari, Z. Yaakob, Y. Chandra Sharma, and K. Sopian, "Overview on the production of paraffin based-biofuels via catalytic hydrodeoxygenation," *Renew. Sustain. Energy Rev.*, vol. 22, no. 0, pp. 121–132, 2013.

[31] B. Veriansyah, J. Y. Han, S. K. Kim, S.-A. Hong, Y. J. Kim, J. S. Lim, Y.-W. Shu, S.-G. Oh, and J. Kim, "Production of renewable diesel by hydroprocessing of soybean oil: Effect of catalysts," *Fuel*, vol. 94, no. 0, pp. 578–585, 2012.

[32] G. W. Huber, P. O'Connor, and A. Corma, "Processing biomass in conventional oil refineries: Production of high quality diesel by hydrotreating vegetable oils in heavy vacuum oil mixtures," *Appl. Catal. A Gen.*, vol. 329, no. 0, pp. 120–129, 2007.

[33] S. K. Kim, S. Brand, H. Lee, Y. Kim, and J. Kim, "Production of renewable diesel by hydrotreatment of soybean oil: Effect of reaction parameters," *Chem. Eng. J.*, vol. 228, no. 0, pp. 114–123, 2013.

[34] P. Šimáček, D. Kubička, I. Kubičková, F. Homola, M. Pospíšil, and J. Chudoba, "Premium quality renewable diesel fuel by hydroprocessing of sunflower oil," *Fuel*, vol. 90, no. 7, pp. 2473–2479, 2011.

[35] C. Zhao, T. Bruck, and J. A. Lercher, "Catalytic deoxygenation of microalgae oil to green hydrocarbons," *Green Chem.*, vol. 15, no. 7, pp. 1720–1739, 2013.

[36] I. Kubičková and D. Kubička, "Utilization of Triglycerides and Related Feedstocks for Production of Clean Hydrocarbon Fuels and Petrochemicals: A Review," *Waste and Biomass Valorization*, vol. 1, no. 3, pp. 293–308, 2010.

[37] A. Srifa, K. Faungnawakij, V. Itthibenchapong, and S. Assabumrungrat, "Roles of monometallic catalysts in hydrodeoxygenation of palm oil to green diesel," *Chem. Eng. J.*, vol. 278, pp. 249–258, Oct. 2015.

[38] S. Mikkonen, "Second-generation renewable diesel offers advantages," *Hydrocarb. Process.*, vol. 87, no. 2, pp. 63–66, 2008.

[39] T. N. Kalnes, K. P. Koers, T. Marker, and D. R. Shonnard, "A technoeconomic and environmental life cycle comparison of green diesel to biodiesel and syndiesel," *Environ. Prog. Sustain. Energy*, vol. 28, no. 1, pp. 111–120, 2009.

[40] M. Canakci and H. Sanli, "Biodiesel production from various feedstocks and their effects on the fuel properties," *J. Ind. Microbiol. Biotechnol.*, vol. 35, no. 5, pp. 431–441, 2008.

[41] P. Šimáček, D. Kubička, G. Šebor, and M. Pospíšil, "Hydroprocessed rapeseed oil as a source of hydrocarbon-based biodiesel," *Fuel*, vol. 88, no. 3, pp. 456–460, 2009.

[42] J. Hancsók, T. Kasza, S. Kovács, P. Solymosi, and A. Holló, "Production of bioparaffins by the catalytic hydrogenation of natural triglycerides," *J. Clean. Prod.*,

vol. 34, no. 0, pp. 76–81, 2012.

[43] A. Guzman, J. E. Torres, L. P. Prada, and M. L. Nuñez, “Hydroprocessing of crude palm oil at pilot plant scale,” *Catal. Today*, vol. 156, no. 1–2, pp. 38–43, 2010.

[44] L. Siswati, P. Mäki-Arvela, J. Beltramini, G. Q. M. Lu, and D. Y. Murzin, “Transforming Triglycerides and Fatty Acids into Biofuels,” *ChemSusChem*, vol. 2, no. 12, pp. 1109–1119, 2009.

[45] “http://www.infomine.com/chartsanddata. London Metal Exchange (LME) accessed Aug 2017,” 2017.

[46] P. P. Nunes, “Docteur-Ingenieur thesis, Hydrocraquage de l’huile de soja sur des catalyseurs au rhodium et au ruthenium supportes. Université Pierre et Marie Curie, Paris.,” 1984.

[47] O. İ. Şenol, T.-R. Viljava, and A. O. I. Krause, “Hydrodeoxygenation of methyl esters on sulphided NiMo/γ-Al_2O_3 and CoMo/γ-Al_2O_3 catalysts,” *Catal. Today*, vol. 100, no. 3–4, pp. 331–335, Feb. 2005.

[48] M. W. Balakos and E. E. Hernandez, “Catalyst characteristics and performance in edible oil hydrogenation,” *Catal. Today*, vol. 35, no. 4, pp. 415–425, 1997.

[49] R. Tiwari, B. S. Rana, R. Kumar, D. Verma, R. Kumar, R. K. Joshi, M. O. Garg, and A. K. Sinha, “Hydrotreating and hydrocracking catalysts for processing of waste soya-oil and refinery-oil mixtures,” *Catal. Commun.*, vol. 12, no. 6, pp. 559–562, 2011.

[50] J. Duan, J. Han, H. Sun, P. Chen, H. Lou, and X. Zheng, “Diesel-like hydrocarbons obtained by direct hydrodeoxygenation of sunflower oil over Pd/Al-SBA-15 catalysts,” *Catal. Commun.*, vol. 17, pp. 76–80, 2012.

[51] E. Santillan-Jimenez, T. Morgan, J. Shoup, A. E. Harman-Ware, and M. Crocker, “Catalytic deoxygenation of triglycerides and fatty acids to hydrocarbons over Ni–Al layered double hydroxide,” *Catal. Today*, vol. 237, pp. 136–144, Nov. 2014.

[52] R. Sotelo-Boyás, Y. Liu, and T. Minowa, “Renewable Diesel Production from the Hydrotreating of Rapeseed Oil with Pt/Zeolite and NiMo/Al_2O_3 Catalysts,” *Ind. Eng. Chem. Res.*, vol. 50, no. 5, pp. 2791–2799, 2010.

[53] Y. Liu, R. Sotelo-Boyás, K. Murata, T. Minowa, and K. Sakanishi, “Hydrotreatment of Jatropha Oil to Produce Green Diesel over Trifunctional Ni–Mo/SiO_2–Al_2O_3 Catalyst,” *Chem. Lett.*, vol. 38, no. 6, pp. 552–553, 2009.

[54] G. B. Kunde and G. D. Yadav, “Green approach in the sol–gel synthesis of defect free unsupported mesoporous alumina films,” *Microporous Mesoporous Mater.*, vol. 224, pp. 43–50, Apr. 2016.

[55] G. Cao and Y. Wang, *Nanostructures and Nanomaterials Synthesis, Properties, and Applications 2nd Edition*. World Scientific Publishing, 2011.

[56] W. Wu, Z. Wan, M. Zhu, and D. Zhang, “A facile route to aqueous phase synthesis of mesoporous alumina with controllable structural properties,” *Microporous Mesoporous Mater.*, vol. 223, pp. 203–212, 2016.

[57] W. Wu, Z. Wan, W. Chen, M. Zhu, and D. Zhang, “Synthesis of mesoporous alumina with tunable structural properties,” *Microporous Mesoporous Mater.*, vol. 217, pp. 12–20, Nov. 2015.

[58] Z.-X. Sun, T.-T. Zheng, Q.-B. Bo, M. Du, and W. Forsling, “Effects of calcination temperature on the pore size and wall crystalline structure of mesoporous alumina.,” *J. Colloid Interface Sci.*, vol. 319, no. 1, pp. 247–51, Mar. 2008.

[59] N. Suzuki and Y. Yamauchi, “One-step synthesis of hierarchical porous γ-alumina with high surface area,” *J. Sol-Gel Sci. Technol.*, vol. 53, no. 2, pp. 428–433, Dec. 2009.

[60] P. G. Savva, K. Goundani, J. Vakros, K. Bourikas, C. Fountzoula, D. Vattis, A. Lycourghiotis, and C. Kordulis, “Benzene hydrogenation over Ni/Al_2O_3 catalysts prepared by conventional and sol–gel techniques,” *Appl. Catal. B Environ.*, vol. 79, no. 3, pp. 199–207, 2008.

[61] M. V Bykova, D. Y. Ermakov, V. V Kaichev, O. A. Bulavchenko, A. A. Saraev, M. Y. Lebedev, and V. A. Yakovlev, “Ni-based sol–gel catalysts as promising systems for crude bio-oil upgrading: Guaiacol hydrodeoxygenation study,” *Appl. Catal. B Environ.*, vol. 113, pp. 296–307, 2012.

[62] J. Newnham, K. Mantri, M. H. Amin, J. Tardio, and S. K. Bhargava, “Highly stable

and active Ni-mesoporous alumina catalysts for dry reforming of methane," *Int. J. Hydrogen Energy*, vol. 37, no. 2, pp. 1454–1464, Jan. 2012.

[63] H. Tian, S. Li, L. Zeng, H. Ma, and J. Gong, "Assembly of ordered mesoporous alumina-supported nickel nanoparticles with high temperature stability for CO methanation," *Sci. China Mater.*, vol. 58, no. 1, pp. 9–15, 2015.

[64] S. Texier, G. Berhault, G. Pérot, and F. Diehl, "Activation of alumina-supported hydrotreating catalysts by organosulfides or H2S: Effect of the H2S partial pressure used during the activation process," *Appl. Catal. A Gen.*, vol. 293, no. 0, pp. 105–119, 2005.

[65] T. Wei-qian, L. Jing, L. Can, F. Kai, and R. Long, "Hydrotreatment of jatropha oil over CoMoS/gamma Al_2O_3 catalyst," *J Fuel Chem Technol*, vol. 41, no. 2, pp. 207–213, 2013.

[66] D. Kubička and J. Horáček, "Deactivation of HDS catalysts in deoxygenation of vegetable oils," *Appl. Catal. A Gen.*, vol. 394, no. 1–2, pp. 9–17, 2011.

[67] O. İ. Şenol, T.-R. Viljava, and A. O. I. Krause, "Effect of sulphiding agents on the hydrodeoxygenation of aliphatic esters on sulphided catalysts," *Appl. Catal. A Gen.*, vol. 326, no. 2, pp. 236–244, 2007.

[68] O. İ. Şenol, E. M. Ryymin, T. R. Viljava, and A. O. I. Krause, "Effect of hydrogen sulphide on the hydrodeoxygenation of aromatic and aliphatic oxygenates on sulphided catalysts," *J. Mol. Catal. A Chem.*, vol. 277, no. 1–2, pp. 107–112, 2007.

[69] M. Al-Sabawi, J. Chen, and S. Ng, "Fluid Catalytic Cracking of Biomass-Derived Oils and Their Blends with Petroleum Feedstocks: A Review," *Energy & Fuels*, vol. 26, no. 9, pp. 5355–5372, Sep. 2012.

[70] M. Krár, S. Kovács, D. Kalló, and J. Hancsók, "Fuel purpose hydrotreating of sunflower oil on CoMo/Al_2O_3 catalyst," *Bioresour. Technol.*, vol. 101, no. 23, pp. 9287–9293, 2010.

[71] M. Gousi, C. Andriopoulou, K. Bourikas, S. Ladas, M. Sotiriou, C. Kordulis, and A. Lycourghiotis, "Green diesel production over nickel-alumina co-precipitated catalysts," *Appl. Catal. A Gen.*, vol. 536, pp. 45–56, 2017.

[72] I. Hachemi, N. Kumar, P. Mäki-Arvela, J. Roine, M. Peurla, J. Hemming, J. Salonen, and D. Y. Murzin, “Sulfur-free Ni catalyst for production of green diesel by hydrodeoxygenation,” *J. Catal.*, vol. 347, pp. 205–221, 2017.

[73] S. K. Kim, J. Y. Han, H. Lee, T. Yum, Y. Kim, and J. Kim, “Production of renewable diesel via catalytic deoxygenation of natural triglycerides: Comprehensive understanding of reaction intermediates and hydrocarbons,” *Appl. Energy*, vol. 116, pp. 199–205, Mar. 2014.

[74] S. R. Yenumala, S. K. Maity, and D. Shee, “Hydrodeoxygenation of karanja oil over supported nickel catalysts: influence of support and nickel loading,” *Catal. Sci. Technol.*, vol. 6, no. 9, pp. 3156–3165, 2016.

[75] E. Santillan-Jimenez, T. Morgan, J. Lacny, S. Mohapatra, and M. Crocker, “Catalytic deoxygenation of triglycerides and fatty acids to hydrocarbons over carbon-supported nickel,” *Fuel*, vol. 103, pp. 1010–1017, Jan. 2013.

[76] E. Santillan-Jimenez, T. Morgan, R. Loe, and M. Crocker, “Continuous catalytic deoxygenation of model and algal lipids to fuel-like hydrocarbons over Ni–Al layered double hydroxide,” *Catal. Today*, vol. 258, pp. 284–293, 2015.

[77] L. Jia, M. Raad, S. Hamieh, J. Toufaily, T. Hamieh, M. Bettahar, G. Mauviel, M. Tarrighi, L. Pinard, and A. Dufour, “Catalytic fast pyrolysis of biomass: superior selectivity of hierarchical zeolite to aromatics,” *Green Chem.*, vol. 19, no. 22, pp. 5442–5459, 2017.

[78] E. Santillan-Jimenez, R. Pace, S. Marques, T. Morgan, C. McKelphin, J. Mobley, and M. Crocker, “Extraction, characterization, purification and catalytic upgrading of algae lipids to fuel-like hydrocarbons,” *Fuel*, vol. 180, pp. 668–678, 2016.

[79] A. Srifa, N. Viriya-empikul, S. Assabumrungrat, and K. Faungnawakij, “Catalytic behaviors of Ni/[gamma]-Al_2O_3 and Co/[gamma]-Al_2O_3 during the hydrodeoxygenation of palm oil,” *Catal. Sci. Technol.*, vol. 5, no. 7, pp. 3693–3705, 2015.

[80] S. Bezergianni, A. Dimitriadis, A. Kalogianni, and P. A. Pilavachi, “Hydrotreating of waste cooking oil for biodiesel production. Part I: Effect of temperature on

product yields and heteroatom removal," *Bioresour. Technol.*, vol. 101, no. 17, pp. 6651–6656, 2010.

[81] S. Bezergianni, A. Dimitriadis, T. Sfetsas, and A. Kalogianni, "Hydrotreating of waste cooking oil for biodiesel production. Part II: Effect of temperature on hydrocarbon composition," *Bioresour. Technol.*, vol. 101, no. 19, pp. 7658–7660, 2010.

[82] J. Liu, C. Liu, G. Zhou, S. Shen, and L. Rong, "Hydrotreatment of Jatropha oil over NiMoLa/Al_2O_3 catalyst," *Green Chem.*, vol. 14, no. 9, pp. 2499–2505, 2012.

[83] L. M. Orozco, D. A. Echeverri, L. Sánchez, and L. A. Rios, "Second-generation green diesel from castor oil: Development of a new and efficient continuous-production process," *Chem. Eng. J.*, vol. 322, pp. 149–156, 2017.

[84] M. Anand and A. K. Sinha, "Temperature-dependent reaction pathways for the anomalous hydrocracking of triglycerides in the presence of sulfided Co–Mo-catalyst," *Bioresour. Technol.*, vol. 126, pp. 148–155, 2012.

[85] K.-N. P. Kumar, J. Tranto, B. N. Nair, J. Kumar, J. W. Høj, and J. E. Engell, "Effect of sintering atmosphere on the pore-structure stability of cerium-doped nanostructured alumina," *Mater. Res. Bull.*, vol. 29, no. 5, pp. 551–558, May 1994.

[86] Y. Men, H. Gnaser, and C. Ziegler, "Adsorption/desorption studies on nanocrystalline alumina surfaces," *Anal. Bioanal. Chem.*, vol. 375, no. 7, pp. 912–916, 2003.

[87] C. Marquez-Alvarez, N. Zilkova, J. Perez-Pariente, and J. Cejka, "Synthesis, characterization and catalytic applications of organized mesoporous aluminas," *Catal. Rev. Eng.*, vol. 50, no. 2, pp. 222–286, 2008.

[88] C. J. Brinker, Y. Lu, A. Sellinger, and H. Fan, "Evaporation-Induced Self-Assembly: Nanostructures Made Easy," *Adv. Mater.*, vol. 11, no. 7, pp. 579–585, 1999.

[89] D. Grosso, F. Cagnol, G. J. de A. A. Soler-Illia, E. L. Crepaldi, H. Amenitsch, A. Brunet-Bruneau, A. Bourgeois, and C. Sanchez, "Fundamentals of Mesostructuring Through Evaporation-Induced Self-Assembly," *Adv. Funct. Mater.*, vol. 14, no. 4, pp. 309–322, Apr. 2004.

[90] V. V Vinogradov, A. V Vinogradov, A. S. Kraev, A. V Agafonov, and V. G. Kessler, “Sol--gel synthesis, characterization and catalytic activity of γ-alumina with bimodal mesopore distribution,” *J. Sol-Gel Sci. Technol.*, vol. 68, no. 2, pp. 155–161, 2013.

[91] T. Onfroy, W.-C. Li, F. Schuth, and H. Knozinger, “Surface chemistry of carbon-templated mesoporous aluminas,” *Phys. Chem. Chem. Phys.*, vol. 11, no. 19, pp. 3671–3679, 2009.

[92] D. Han, X. Li, L. Zhang, Y. Wang, Z. Yan, and S. Liu, “Hierarchically ordered meso/macroporous γ-alumina for enhanced hydrodesulfurization performance,” *Microporous Mesoporous Mater.*, vol. 158, pp. 1–6, Aug. 2012.

[93] J. C. Ray, K.-S. You, J.-W. Ahn, and W.-S. Ahn, “Mesoporous alumina (I): Comparison of synthesis schemes using anionic, cationic, and non-ionic surfactants,” *Microporous Mesoporous Mater.*, vol. 100, no. 1–3, pp. 183–190, Mar. 2007.

[94] B. Sathyaseelan, I. Baskaran, and K. Sivakumar, “Phase Transition Behavior of Nanocrystalline Al_2O_3 Powders,” *Soft Nanosci. Lett.*, vol. 3, no. 4, pp. 69–74, 2013.

[95] J. Gangwar, B. K. Gupta, S. K. Tripathi, and A. K. Srivastava, “Phase dependent thermal and spectroscopic responses of Al_2O_3 nanostructures with different morphogenesis,” *Nanoscale*, vol. 7, no. 32, pp. 13313–13344, 2015.

[96] S. M. Grant, A. Vinu, S. Pikus, and M. Jaroniec, “Adsorption and structural properties of ordered mesoporous alumina synthesized in the presence of F127 block copolymer,” *Colloids Surfaces A Physicochem. Eng. Asp.*, vol. 385, no. 1–3, pp. 121–125, Jul. 2011.

[97] R. Bleta, P. Alphonse, L. Pin, M. Gressier, and M.-J. Menu, “An efficient route to aqueous phase synthesis of nanocrystalline γ-Al_2O_3 with high porosity: from stable boehmite colloids to large pore mesoporous alumina.,” *J. Colloid Interface Sci.*, vol. 367, no. 1, pp. 120–8, Feb. 2012.

[98] Y. Li, J. Su, J. Ma, F. Yu, and R. Li, “A high surface area nanocrystalline alumina with tailoring texture by mixed template,” *Mater. Lett.*, vol. 153, pp. 165–167, Aug. 2015.

[99] S. Royer, F. Bérubé, and S. Kaliaguine, “Effect of the synthesis conditions on the redox and catalytic properties in oxidation reactions of $LaCo_{1-x}Fe_xO_3$,” *Appl. Catal. A Gen.*, vol. 282, no. 1, pp. 273–284, 2005.

[100] K. S. W. Sing, “Reporting physisorption data for gas/solid systems with special reference to the determination of surface area and porosity,” *Pure Appl. Chem.*, vol. 54, no. 11, pp. 2201–2218, 1982.

[101] Q. Yuan, A. Yin, C. Luo, L. Sun, Y. Zhang, W. Duan, H. Liu, and C. Yan, “Facile Synthesis for Ordered Mesoporous γ-Aluminas with High Thermal Stability,” *J. Am. Chem. Soc.*, vol. 130, no. 11, pp. 3465–3472, 2008.

[102] B. Huang, C. H. Bartholomew, S. J. Smith, and B. F. Woodfield, “Facile solvent-deficient synthesis of mesoporous γ-alumina with controlled pore structures,” *Microporous Mesoporous Mater.*, vol. 165, no. 0, pp. 70–78, 2013.

[103] H. Li, L. Zhang, H. Dai, and H. He, “Facile Synthesis and Unique Physicochemical Properties of Three-Dimensionally Ordered Macroporous Magnesium Oxide, Gamma-Alumina, and Ceria−Zirconia Solid Solutions with Crystalline Mesoporous Walls,” *Inorg. Chem.*, vol. 48, no. 10, pp. 4421–4434, Apr. 2009.

[104] C. Boissiere, L. Nicole, C. Gervais, F. Babonneau, M. Antonietti, H. Amenitsch, C. Sanchez, and D. Grosso, “Nanocrystalline mesoporous γ-Alumina powders ‘UPMC1 material’ gathers thermal and chemical stability with high surface area,” *Chem. Mater.*, vol. 18, no. 1, pp. 5238–5243, 2006.

[105] P. Padmaja, P. K. Pillai, K. G. K. Warrier, and M. Padmanabhan, “Adsorption Isotherm and Pore Characteristics of Nano Alumina Derived from Sol-Gel Boehmite,” *J. Porous Mater.*, vol. 11, no. 3, pp. 147–155, Jul. 2004.

[106] G. L. Teoh, K. Y. Liew, and W. A. K. Mahmood, “Synthesis and characterization of sol--gel alumina nanofibers,” *J. Sol-Gel Sci. Technol.*, vol. 44, no. 3, pp. 177–186, 2007.

[107] S. Liu, L. Zhang, L. An, W. Fei, and H. Heinrich, “Phase Transformation of Mechanically Milled Nano-Sized gamma-Alumina,” *J. Am. Ceram. Soc.*, vol. 88, no. 9, pp. 2559–2563, Sep. 2005.

[108] S. Ghosh, P. Bose, S. Basak, and M. K. Naskar, “Solvothermal-assisted evaporation-induced self-assembly process for significant improvement in the textural properties of γ-Al_2O_3, and study dye adsorption efficiency,” *J. Asian Ceram. Soc.*, vol. 3, no. 2, pp. 198–205, Jun. 2015.

[109] A. Miño, C. Lancelot, P. Blanchard, C. Lamonier, L. Rouleau, M. Roy-Auberger, S. Royer, and E. Payen, “Strategy to produce highly loaded alumina supported CoMo-S catalyst for straight run gas oil hydrodesulfurization,” *Appl. Catal. A Gen.*, vol. 530, pp. 145–153, 2017.

[110] G. W. Lee, “Phase transition characteristics of flame-synthesized gamma-Al 2O3 nanoparticles with heat treatment,” *Int. J. Chem. Nucl. Metall. Mater. Eng.*, vol. 7, no. 9, pp. 358–361, 2013.

[111] K. M. Parida, A. C. Pradhan, J. Das, and N. Sahu, “Synthesis and characterization of nano-sized porous gamma-alumina by control precipitation method,” *Mater. Chem. Phys.*, vol. 113, no. 1, pp. 244–248, Jan. 2009.

[112] M. Takht Ravanchi, M. Rahimi Fard, S. Fadaeerayeni, and F. Yaripour, “Effect of Calcination Conditions on Crystalline Structure and Pore Size Distribution for a Mesoporous Alumina,” *Chem. Eng. Commun.*, vol. 202, no. 4, pp. 493–499, Oct. 2014.

[113] L. A. A. Chunduri, T. M. Rattan, M. Molli, and V. Kamisetti, “Single step preparation of nano size gamma alumina exhibiting enhanced fluoride adsorption,” *Mater. Express*, vol. 4, no. 3, pp. 235–241, 2014.

[114] F. Huang, Y. Zheng, Y. Xiao, Y. Zheng, G. Cai, and K. Wei, “A new synthetic procedure for ordered mesoporous γ-alumina using phthalic acid as an interfacial protector,” *Mater. Lett.*, vol. 65, no. 2, pp. 244–246, Jan. 2011.

[115] J. Xu, A. Wang, X. Wang, D. Su, and T. Zhang, “Synthesis, characterization, and catalytic application of highly ordered mesoporous alumina-carbon nanocomposites,” *Nano Res.*, vol. 4, no. 1, pp. 50–60, 2011.

[116] B. Yousefi, S. M. Mirhassani, A. AhmadiFard, and M. Hosseini, “Hierarchical segmentation of urban satellite imagery,” *Int. J. Appl. Earth Obs. Geoinf.*, vol. 30,

pp. 158–166, Aug. 2014.

[117] W. Cai, J. Yu, C. Anand, A. Vinu, and M. Jaroniec, “Facile synthesis of ordered mesoporous alumina and alumina-supported metal oxides with tailored adsorption and framework properties,” *Chem. Mater.*, vol. 23, no. 5, pp. 1147–1157, Mar. 2011.

[118] S. Hamoudi and S. Kaliaguine, “Periodic mesoporous organosilica from micellar oligomer template solution,” *Chem. Commun.*, no. 18, pp. 2118–2119, 2002.

[119] Z. Wu, Q. Li, D. Feng, P. A. Webley, and D. Zhao, “Ordered mesoporous crystalline gamma-Al_2O_3 with variable architecture and porosity from a single hard template.,” *J. Am. Chem. Soc.*, vol. 132, no. 34, pp. 12042–50, Sep. 2010.

[120] B. Huang, C. H. Bartholomew, and B. F. Woodfield, “Facile structure-controlled synthesis of mesoporous γ-alumina: Effects of alcohols in precursor formation and calcination,” *Microporous Mesoporous Mater.*, vol. 177, no. 0, pp. 37–46, 2013.

[121] D. Gielen, F. Boshell, and D. Saygin, “Climate and energy challenges for materials science,” *Nat Mater*, vol. 15, no. 2, pp. 117–120, Feb. 2016.

[122] M. Hajjari, M. Tabatabaei, M. Aghbashlo, and H. Ghanavati, “A review on the prospects of sustainable biodiesel production: A global scenario with an emphasis on waste-oil biodiesel utilization,” *Renew. Sustain. Energy Rev.*, vol. 72, no. October 2015, pp. 445–464, 2017.

[123] W. Kiatkittipong, S. Phimsen, K. Kiatkittipong, S. Wongsakulphasatch, N. Laosiripojana, and S. Assabumrungrat, “Diesel-like hydrocarbon production from hydroprocessing of relevant refining palm oil,” *Fuel Process. Technol.*, vol. 116, no. 0, pp. 16–26, 2013.

[124] D. Kochetkova, J. Blažek, P. Šimáček, M. Staš, and Z. Beňo, “Influence of rapeseed oil hydrotreating on hydrogenation activity of CoMo catalyst,” *Fuel Process. Technol.*, vol. 142, pp. 319–325, 2016.

[125] A. Kleinová, I. Vailing, J. Lábaj, J. Mikulec, and J. Cvengroš, “Vegetable oils and animal fats as alternative fuels for diesel engines with dual fuel operation,” *Fuel Process. Technol.*, vol. 92, no. 10, pp. 1980–1986, 2011.

[126] V. F. de Almeida, P. J. García-Moreno, A. Guadix, and E. M. Guadix, “Biodiesel

production from mixtures of waste fish oil, palm oil and waste frying oil: Optimization of fuel properties," *Fuel Process. Technol.*, vol. 133, pp. 152–160, 2015.

[127] S. R. Chia, K. W. Chew, P. L. Show, H. C. Ong, S.-M. Phang, T. C. Ling, D. Nagarajan, D.-J. Lee, and J.-S. Chang, "Sustainable approaches for algae utilization in bioenergy production," *Renew. Energy*, 2017.

[128] D. Kubička, J. Horáček, M. Setnička, R. Bulánek, A. Zukal, and I. Kubičková, "Effect of support-active phase interactions on the catalyst activity and selectivity in deoxygenation of triglycerides," *Appl. Catal. B Environ.*, vol. 145, pp. 101–107, Feb. 2014.

[129] B. S. Sazzad, M. A. Fazal, A. S. M. A. Haseeb, and H. H. Masjuki, "Retardation of oxidation and material degradation in biodiesel: a review," *RSC Adv.*, vol. 6, no. 65, pp. 60244–60263, 2016.

[130] P. Priecel, L. Čapek, D. Kubička, F. Homola, P. Ryšánek, and M. Pouzar, "The role of alumina support in the deoxygenation of rapeseed oil over NiMo–alumina catalysts," *Catal. Today*, vol. 176, no. 1, pp. 409–412, Nov. 2011.

[131] E. V Parkhomchuk, A. I. Lysikov, A. G. Okunev, P. D. Parunin, V. S. Semeikina, A. B. Ayupov, V. A. Trunova, and V. N. Parmon, "Meso/Macroporous CoMo Alumina Pellets for Hydrotreating of Heavy Oil," *Ind. Eng. Chem. Res.*, vol. 52, no. 48, pp. 17117–17125, Dec. 2013.

[132] G.-C. Wang and T.-M. Lu, "Crystal Lattices and Reciprocal Lattices," in *RHEED Transmission Mode and Pole Figures: Thin Film and Nanostructure Texture Analysis*, New York, NY: Springer New York, 2014, pp. 7–22.

[133] D. Pan, Q. Xu, Z. Dong, S. Chen, F. Yu, X. Yan, B. Fan, and R. Li, "Facile synthesis of highly ordered mesoporous cobalt-alumina catalysts and their application in liquid phase selective oxidation of styrene," *RSC Adv.*, vol. 5, no. 119, pp. 98377–98390, 2015.

[134] J. Ji, X. Duan, G. Qian, X. Zhou, G. Tong, and W. Yuan, "Towards an efficient CoMo/γ-Al_2O_3 catalyst using metal amine metallate as an active phase precursor:

Enhanced hydrogen production by ammonia decomposition," *Int. J. Hydrogen Energy*, vol. 39, no. 24, pp. 12490–12498, Aug. 2014.

[135] M. H. Aboonasr Shiraz, M. Rezaei, and F. Meshkani, "Microemulsion synthesis method for preparation of mesoporous nanocrystalline γ-Al_2O_3 powders as catalyst carrier for nickel catalyst in dry reforming reaction," *Int. J. Hydrogen Energy*, vol. 41, no. 15, pp. 6353–6361, Apr. 2016.

[136] A. Afshar Taromi and S. Kaliaguine, "Synthesis of ordered mesoporous γ-alumina – Effects of calcination conditions and polymeric template concentration," *Microporous Mesoporous Mater.*, vol. 248, pp. 179–191, Aug. 2017.

[137] C. Liu, J. Liu, G. Zhou, W. Tian, and L. Rong, "Transformation of Jatropha oil into green diesel over a new heteropolyacid Catalyst," *Environ. Prog. Sustain. Energy*, vol. 32, no. 4, pp. 1240–1246, 2013.

[138] P. Kim, Y. Kim, H. Kim, I. K. Song, and J. Yi, "Synthesis and characterization of mesoporous alumina with nickel incorporated for use in the partial oxidation of methane into synthesis gas," *Appl. Catal. A Gen.*, vol. 272, no. 1, pp. 157–166, 2004.

[139] R. Rinaldi, F. Y. Fujiwara, W. Hölderich, and U. Schuchardt, "Tuning the acidic properties of aluminas via sol-gel synthesis: New findings on the active site of alumina-catalyzed epoxidation with hydrogen peroxide," *J. Catal.*, vol. 244, no. 1, pp. 92–101, 2006.

[140] P. Barpanda, N. Recham, J.-N. Chotard, K. Djellab, W. Walker, M. Armand, and J.-M. Tarascon, "Structure and electrochemical properties of novel mixed Li($Fe_{1-x}M_x$)SO_4F (M = Co, Ni, Mn) phases fabricated by low temperature ionothermal synthesis," *J. Mater. Chem.*, vol. 20, no. 9, pp. 1659–1668, 2010.

[141] X. Wang and U. S. Ozkan, "Characterization of Active Sites over Reduced Ni−Mo/Al_2O_3 Catalysts for Hydrogenation of Linear Aldehydes," *J. Phys. Chem. B*, vol. 109, no. 5, pp. 1882–1890, Feb. 2005.

[142] J. Escobar, M. C. Barrera, J. A. Toledo, M. A. Cortés-Jácome, C. Angeles-Chávez, S. Núñez, V. Santes, E. Gómez, L. Díaz, E. Romero, and J. G. Pacheco, "Effect of ethyleneglycol addition on the properties of P-doped NiMo/Al_2O_3 HDS catalysts:

Part I. Materials preparation and characterization," *Appl. Catal. B Environ.*, vol. 88, no. 3–4, pp. 564–575, May 2009.

[143] A. D. Gandubert, C. Legens, D. Guillaume, S. Rebours, and E. Payen, "X-ray Photoelectron Spectroscopy Surface Quantification of Sulfided CoMoP Catalysts – Relation Between Activity and Promoted Sites – Part I: Influence of the Co/Mo Ratio," *Oil Gas Sci. Technol. - Rev. IFP*, vol. 62, no. 1, pp. 79–89, 2007.

[144] D. Laurenti, B. Phung-Ngoc, C. Roukoss, E. Devers, K. Marchand, L. Massin, L. Lemaitre, C. Legens, A.-A. Quoineaud, and M. Vrinat, "Intrinsic potential of alumina-supported CoMo catalysts in HDS: Comparison between γc, γT, and δ-alumina," *J. Catal.*, vol. 297, pp. 165–175, Jan. 2013.

[145] X. Wang, G. Li, and U. S. Ozkan, "Hydrogenation of hexanal over sulfided Ni-Mo/γ-Al_2O_3 catalysts," *J. Mol. Catal. A Chem.*, vol. 217, no. 1–2, pp. 219–229, Aug. 2004.

[146] N. Wang, J. Li, X. Liu, R. Hu, Y. Zhang, H. Su, and X. Gu, "Remarkable enhancement of the catalytic performance of molybdenum sulfide catalysts via an in situ decomposition method for higher alcohol synthesis from syngas," *RSC Adv.*, vol. 6, no. 113, pp. 112356–112362, 2016.

[147] A. V. Naumkin, A. Kraut-Vass, S. W. Gaarenstroom, and C. J. Powell, "NIST X-ray Photoelectron Spectroscopy Database 20, Version 4.1 (National Institute of Standards and Technology, Gaithersburg)." 2012.

[148] D. L. Nguyen, S. Gillot, D. O. Souza, P. Blanchard, C. Lamonier, E. Berrier, T. V Kotbagi, M. K. Dongare, S. B. Umbarkar, S. Cristol, E. Payen, and C. Lancelot, "One-Pot Sol–Gel Preparation for Efficient Cobalt–Molybdenum–Titania Hydrotreating Catalysts," *ChemCatChem*, vol. 4, no. 12, pp. 2112–2120, 2012.

[149] G. Zhou, Y. Hou, L. Liu, H. Liu, C. Liu, J. Liu, H. Qiao, W. Liu, Y. Fan, S. Shen, and L. Rong, "Preparation and characterization of NiW-nHA composite catalyst for hydrocracking," *Nanoscale*, vol. 4, no. 24, pp. 7698–7703, 2012.

[150] H. Wang, S. Yan, S. O. Salley, and K. Y. S. Ng, "Hydrocarbon fuels production from hydrocracking of soybean oil using transition metal carbides and nitrides

supported on ZSM-5," *Ind. Eng. Chem. Res.*, vol. 51, no. 30, pp. 10066–10073, Aug. 2012.

[151] R. K. Sharma, M. Anand, B. S. Rana, R. Kumar, S. A. Farooqui, M. G. Sibi, and A. K. Sinha, "Jatropha-oil conversion to liquid hydrocarbon fuels using mesoporous titanosilicate supported sulfide catalysts," *Catal. Today*, vol. 198, no. 1, pp. 314–320, 2012.

[152] K. Kandel, J. W. Anderegg, N. C. Nelson, U. Chaudhary, and I. I. Slowing, "Supported iron nanoparticles for the hydrodeoxygenation of microalgal oil to green diesel," *J. Catal.*, vol. 314, pp. 142–148, May 2014.

[153] K. Fan, X. Yang, J. Liu, and L. Rong, "Effect of reducing catalyst coke by La loading in hydrocracking of Jatropha oil," *RSC Adv.*, vol. 5, no. 42, pp. 33339–33346, 2015.

[154] B. D. Wahlen, R. M. Willis, and L. C. Seefeldt, "Biodiesel production by simultaneous extraction and conversion of total lipids from microalgae, cyanobacteria, and wild mixed-cultures," *Bioresour. Technol.*, vol. 102, no. 3, pp. 2724–2730, 2011.

[155] B. P. Pattanaik and R. D. Misra, "Effect of reaction pathway and operating parameters on the deoxygenation of vegetable oils to produce diesel range hydrocarbon fuels: A review," *Renew. Sustain. Energy Rev.*, vol. 73, pp. 545–557, 2017.

[156] A. Srifa, K. Faungnawakij, V. Itthibenchapong, N. Viriya-Empikul, T. Charinpanitkul, and S. Assabumrungrat, "Production of bio-hydrogenated diesel by catalytic hydrotreating of palm oil over $NiMoS_2/\gamma\text{-}Al_2O_3$ catalyst.," *Bioresour. Technol.*, vol. 158, pp. 81–90, Apr. 2014.

[157] T. Li, J. Cheng, R. Huang, W. Yang, J. Zhou, and K. Cen, "Hydrocracking of palm oil to jet biofuel over different zeolites," *Int. J. Hydrogen Energy*, vol. 41, no. 47, pp. 21883–21887, Dec. 2016.

[158] "http://www.infomine.com/chartsanddata. London Metal Exchange (LME) accessed July 2017."

[159] M. Snåre, I. Kubičková, P. Mäki-Arvela, D. Chichova, K. Eränen, and D. Y. Murzin, "Catalytic deoxygenation of unsaturated renewable feedstocks for production of diesel fuel hydrocarbons," *Fuel*, vol. 87, no. 6, pp. 933–945, May 2008.

[160] T. Li, J. Cheng, R. Huang, J. Zhou, and K. Cen, "Conversion of waste cooking oil to jet biofuel with nickel-based mesoporous zeolite Y catalyst," *Bioresour. Technol.*, vol. 197, pp. 289–294, Dec. 2015.

[161] C. Kordulis, K. Bourikas, M. Gousi, E. Kordouli, and A. Lycourghiotis, "Development of nickel based catalysts for the transformation of natural triglycerides and related compounds into green diesel: a critical review," *Appl. Catal. B Environ.*, vol. 181, pp. 156–196, 2016.

[162] L. Xu, H. Song, and L. Chou, "One-Pot Synthesis of Ordered Mesoporous NiO–CaO–Al_2O_3 Composite Oxides for Catalyzing CO_2 Reforming of CH_4," *ACS Catal.*, vol. 2, no. 7, pp. 1331–1342, Jul. 2012.

[163] K. Jabbour, N. El Hassan, A. Davidson, S. Casale, and P. Massiani, "Factors affecting the long-term stability of mesoporous nickel-based catalysts in combined steam and dry reforming of methane," *Catal. Sci. Technol.*, vol. 6, no. 12, pp. 4616–4631, 2016.

[164] S. M. Morris, P. F. Fulvio, and M. Jaroniec, "Ordered Mesoporous Alumina-Supported Metal Oxides," *J. Am. Chem. Soc.*, vol. 130, no. 45, pp. 15210–15216, Oct. 2008.

[165] G. Li, L. Hu, and J. M. Hill, "Comparison of reducibility and stability of alumina-supported Ni catalysts prepared by impregnation and co-precipitation," *Appl. Catal. A Gen.*, vol. 301, no. 1, pp. 16–24, 2006.

[166] J. Liu, H. Peng, W. Liu, X. Xu, X. Wang, C. Li, W. Zhou, P. Yuan, X. Chen, W. Zhang, and H. Zhan, "Tin Modification on Ni/Al $_2$ O $_3$: Designing Potent Coke-Resistant Catalysts for the Dry Reforming of Methane," *ChemCatChem*, vol. 6, no. 7, pp. 2095–2104, 2014.

[167] Z. Hao, Q. Zhu, Z. Jiang, B. Hou, and H. Li, "Characterization of aerogel Ni/Al_2O_3 catalysts and investigation on their stability for CH_4-CO_2 reforming in a fluidized

bed," *Fuel Process. Technol.*, vol. 90, no. 1, pp. 113–121, Jan. 2009.

[168] S. Kaliaguine, "Application of surface science techniques in the field of zeolitic materials," *Stud. Surf. Sci. Catal.*, vol. 102, pp. 191–230, 1996.

[169] J. Wang, Q. Zhao, H. Hou, Y. Wu, W. Yu, X. Ji, and L. Shao, "Nickel nanoparticles supported on nitrogen-doped honeycomb-like carbon frameworks for effective methanol oxidation," *RSC Adv.*, vol. 7, no. 23, pp. 14152–14158, 2017.

[170] Z. Boukha, C. Jiménez-González, B. de Rivas, J. R. González-Velasco, J. I. Gutiérrez-Ortiz, and R. López-Fonseca, "Synthesis, characterisation and performance evaluation of spinel-derived Ni/Al_2O_3 catalysts for various methane reforming reactions," *Appl. Catal. B Environ.*, vol. 158, pp. 190–201, 2014.